Lagrangian Simulation of Fiber Orientation Dynamics Using Random Walk Methods

Dissertation
zur Erlangung des akademischen Grades eines
Doktors der Naturwissenschaften
(Dr. rer. nat.)

Der Fakultät für Mathematik der
Technischen Universität Dortmund
vorgelegt von

Omid Ahmadi

im September 2023

Dissertation

Lagrangian Simulation of Fiber Orientation Dynamics Using Random Walk Methods

Fakultät für Mathematik
Technische Universität Dortmund

Erstgutachter: Prof. Dr. Dmitri Kuzmin
Zweitgutachter: Prof. Dr. Stefan Turek

Tag der mündlichen Prüfung: 10.01.2024

Acknowledgments

First and foremost, I would like to express my sincerest gratitude to Prof. Dr. Dmitri Kuzmin for providing me with the opportunity to work under his esteemed supervision during my PhD studies and for making my employment at TU Dortmund possible. I deeply appreciate his unwavering availability, innovative ideas and continuous guidance. His professionalism and meticulous attention to detail have always been a source of inspiration for me, making a positive impact on my academic and non-academic pursuits. Thank you for your time, constructive feedback, and consistent support.

I sincerely want to thank Prof. Dr. Stefan Turek for also facilitating my employment. As the Dean of the Mathematics Department, he significantly contributed to creating a welcoming and supportive environment, particularly at the Institute of Applied Mathematics (LS III), which enriched my overall experience, both academically and personally. I am also grateful to him and Prof. Dr. Jan Nagel for kindly agreeing to act as reviewer and examiner, respectively, of this thesis.

I am also deeply indebted to Prof. Dr. Alexei Novikov for his valuable assistance in the field of Stochastics, which significantly contributed to a part of this thesis. Additionally, I want to thank Dr. Otto Mierka for the remarkable support regarding the FEATFLOW software and Dr. Abderrahim Ouazzi for the constructive input on non-Newtonian flows.

Furthermore, I acknowledge the *Deutsche Forschungsgemeinschaft (DFG)* for their financial support, which has been instrumental in the successful completion of this work. In this regard, I thank Dr. Christoph Lohmann for his valuable contributions while we worked on the DFG project that primarily supported this thesis.

I would like to express my gratitude to my colleagues and friends at LS III for creating a friendly and fruitful atmosphere. Let me thank Dr. Babak Sayyid Hosseini, Muhammad Aaqib Afaq, Dr. Arooj Fatima, Robert Jendrny, Dr. Evren Bayraktar, and Dr. Naheed Begum for the delightful exchanges, both academic and personal, we have shared over these years. I also want to thank Katharina Wegener, who kindly proofread this thesis and provided valuable feedback.

Let me take this opportunity to thank Dr. Michael Scharfschwerdt for his support during my time in the industry.

This journey would not have been possible without the unconditional support of my parents, Hayedeh and Saeid, who always stood by me in every situation, backing my decisions, and instilling confidence in me. Many thanks to my brother, Navid, for his backing too. At this point, my warmest and heartfelt gratitude goes to Pegah for her unwavering support, love, and encouragement.

Abstract

This thesis focuses on developing a two-way coupled framework for the numerical simulation of fiber suspension flows. The influence of fibers on the flow is accounted for by evaluating a non-Newtonian stress term incorporated into the Navier-Stokes equations. The accuracy of the analysis depends on a second-order tensor field used to approximate the orientation distribution of fibers. In this context, the disperse phase can be treated in the Lagrangian or Eulerian manner. We conduct a comprehensive comparison of these frameworks for one-way coupled scenarios in both two- and three-dimensional homogeneous flows. With a special focus on the Lagrangian approach, the algorithm for solving the two-way coupled fiber suspension flow in a segregated manner is proposed by incorporating the fiber-induced stresses in the finite element formulation of the Navier-Stokes equations.

In non-dilute suspensions, fiber-fiber interactions may cause spontaneous changes in the orientation of fibers. Applying the theory of rotary Brownian motion, the effect can be studied using a rotary diffusion term with a Laplace-Beltrami operator. In this work, we develop random walk methodologies to emulate the action of the diffusion term without evolving or reconstructing the so-called orientation distribution function. After deriving simplified forms of Brownian motion generators for rotated reference frames, several practical approaches to generating random walks on the unit sphere are discussed. Among the proposed methods, this research effort presents the projection of Cartesian random walks, as well as polar random walks on the tangential plane. The standard random walks are then projected onto the unit sphere. Moreover, we propose an alternative based on a tabulated approximation of the cumulative distribution function obtained from the exact solution of the spherical heat equation.

In the last part of this work, the random walk approaches are compared through several numerical studies, including the study of the orientation distribution of fibers in a three-dimensional homogeneous flow. Then, the two-way coupled solver is validated in a simple geometry, followed by performing a few three-dimensional numerical simulations to study the rheological behavior of the fiber suspension flow through an axisymmetric contraction. The effect of fiber-fiber interactions is also incorporated using the random walk methodology.

Contents

Chapter 1

Introduction

The importance of the dispersed two-phase flows in many industrial processes has led to the development of many numerical models that cover different mixtures and scales. In fluid-solid mixtures, particularly particulate flows, a continuous fluid phase carries rigid or deformable solid particles. The numerical study of such suspensions can provide information about the behavior of the particles in a fluid and several flow characteristics.

Direct numerical simulation (DNS) of particulate flows requires capturing or tracking moving boundaries on a mesh that is fine enough to resolve the smallest scales. The moving mesh methods are mainly based on Arbitrary Lagrangian Eulerian (ALE) approaches [1, 2] used to solve fluid-structure interaction problems. The fictitious domain, the fictitious boundary, and the immersed boundary methods are well-known examples of fixed mesh approaches, in which it is assumed that the whole flow domain is filled with a fluid, and different approaches are used to treat the presence of particles in the flow [3, 4, 5].

The direct numerical simulation requires very fine grid resolutions. Therefore, it is mainly restricted to simulations with a small number of moving particles. Since the mesh size is generally based on the size of particles, simulations with tiny particles may not be computationally feasible with DNS. Hence, subgrid scale models coupled with the averaged Navier-Stokes equations are widely used to study the macroscopic behavior of particulate flows [6].

The fiber suspension flow, an example of particulate flow, is essential in many industrial applications, such as papermaking, recycling, or textile manufacturing. The presence of fibers can greatly affect the final products during the production process. Hence, studying the behavior of fibers and their rheological effect on the

flow is a topic of significant interest.

The fiber suspension flow refers to a flow containing fibers, i.e., consisting of immersed particles carried by a continuous fluid phase. Several factors can affect the behavior of the suspension, such as the shape and the concentration of the fibers and the flow characteristics.

Due to the very small size of fibers, two classes of models are widely used to treat the particles, namely Euler-Lagrange models and Euler-Euler models. While the fluid phase is studied as a continuum, the dispersed phase can be considered either in a Lagrangian or an Eulerian way. Throughout this work, the Lagrangian approach refers to Euler-Lagrange models, which involve considering fibers as individual particles, whereas the Eulerian approach treats dispersed phases as a continuum.

Numerical studies of a fiber suspension flow are also divided into two main categories. In a two-way coupled framework, the rheological influence of fibers on the carrier fluid is taken into account. In contrast, in a one-way coupled approach, the numerical results obtained by flow simulation provide necessary input fields for the subsequent fiber analysis without considering the presence of fibers in the flow.

Jeffery [7] proved that the rotational motion of a fiber immersed in a homogeneous flow depends on the local velocity gradients of the flow and derived an expression for the orientation change of the fiber as a function of a shape parameter, strain rate and spin tensors. He showed that an individual fiber rotates continuously around the vorticity axis on one of an infinite set of closed orbits [8].

In the Eulerian framework, the fiber orientation state can be described by a probability distribution function (PDF). The evolution of the so-called *orientation distribution function* is governed by the Fokker-Planck equation [9, 10], which is cumbersome to solve due to its high dimensionality.

In a two-way coupled framework, the influence of fibers on the flow is taken into account by evaluating a non-Newtonian stress term incorporated into the Navier-Stokes equations. Fiber-induced stresses are commonly computed by a constitutive equation using orientation tensors. These tensors represent even-order moments of the orientation distribution function, specifically the second- and fourth-order ones. The orientation tensors can be defined by forming dyadic products of the orientation vectors, followed by integrating the product of these tensors with the distribution function over the unit sphere. This approach to calculating orientation tensors requires that the distribution function be already known.

Since the Fokker-Planck equation is mathematically complex and costly, Advani and Tucker [11] proposed an evolution equation for the orientation tensor to avoid solving the equation for the distribution function. The overall accuracy of the so-

called Folgar-Tucker equation strongly depends on the modeling of the fourth-order tensor, which may produce nonphysical orientation states in numerical approximations [12, 13]. A variety of *closure* approximations can be found, for example, in [14, 15, 16, 17, 18, 19, 20].

The Folgar-Tucker model can become inaccurate for modeling in injection molding, where it provides a poor prediction of the rate of orientation development [21]. To address this issue, further models were developed, such as reduced-strain closure (RSC) [22] or retardant principal rate (RPR) [23].

In the Lagrangian framework, the orientation tensors are commonly approximated using stochastical approaches. In this framework, the rotary and translational motion of each fiber is tracked individually. Hence, overall, it requires more computational resources compared to the Eulerian approaches.

In the fiber suspension flow, fiber-fiber interactions may cause spontaneous changes in the orientation of fibers, in particular in concentrated suspensions. Using the theory of rotary Brownian motion, Hinch and Leal [24, 25] incorporated fiber-fiber interactions into the Fokker-Planck equation by proposing a rotary diffusion term. Later, more sophisticated anisotropic rotary diffusion (ARD) models were proposed by Koch [26] and Phan-Thien et al. [27], which were developed and incorporated into the above-mentioned Eulerian models; they include: ARD-RSC [28], or iARD-RPR [29]. The new orientation models have been used by commercial injection molding software, including Moldflow and Moldex3D [30].

Numerous Eulerian two-way coupled studies have been conducted in the Literature. Several fully coupled simulations showed the effect of the presence of fibers on the drag reduction in turbulent flows [31, 32, 33, 34]. A number of studies used finite-element-based methods to discretize the Folgar-Tucker equations [35, 12, 13]. As discussed by Lohmann [15], in the first two works [35, 12], the authors use continuous finite elements without proper stabilization, which may lead to numerical instabilities. Whereas Reddy and Mitchell [13] used a discontinuous Galerkin discretization technique to preserve the physical properties of an orientation tensor, the order of this property-preserving scheme is as low as $\frac{1}{2}$. To address the related issues, Lohmann used algebraic flux correction to constrain the continuous and piecewise linear Galerkin discretization to preserve the physical properties of orientation tensors without any post-processing. Using operator splitting techniques applied to the Folgar-Tucker model, he performed a simulation in a three-dimensional axisymmetric contraction problem, studied experimentally and numerically in [10, 35, 12].

Due to the computationally expensive nature of the Lagrangian approach, particularly in complex geometries, two-way coupled simulations have received relatively

less attention. In addition to this point, modeling fiber-fiber interactions has been relatively neglected in many Lagrangian-based works [36, 37, 38, 39, 40, 41, 42]. Applying the principles of the science of random processes, Chen and Yu [43], and Manhart [44], integrated the effect of fiber-fiber interactions into the Jeffery equation. This was followed in Manhart's group, which led to two-dimensional two-way coupled Lagrangian simulations to study the effect of fibers' presence in turbulent flows [45] using a finite volume technique to treat the Navier-Stokes equations.

In this work, we develop a two-way coupled framework for the fiber suspension flow, in which the presence of fibers studied in a Lagrangian manner is incorporated into a finite element formulation. Moreover, to include the fiber-fiber interactions, we design random walks to emulate the action of the rotary diffusion term without evolving or reconstructing the orientation distribution functions. The developed simulation tools and models are applied to a number of two- and three-dimensional problems. This includes a numerical simulation of the fiber suspension flow in the three-dimensional axisymmetric contraction using random walks to take the effect of fiber-fiber interactions into account.

1.1 Outline

Chapter 2 is concerned with mathematical and modeling aspects. After presenting the basic concepts, the underlying equations regarding fluid and solid phases are precisely described. Then, we discuss the rheology of the fiber suspension flow and introduce a number of constitutive equations by which the fiber-induced stresses can be computed.

In Chapter 3, we present numerical models with the aim of developing a two-way coupled simulation tool. After discussing discretization techniques in time and space, we explain an operator splitting method used to solve the Navier-Stokes equations. This is then followed by proposing two different approaches by which fiber-induced stresses can be incorporated into the solver.

Chapter 4 is based on [46], to which the author contributed. The basic assumptions and definitions of the Brownian motion as well as the formulation of a diffusion equation for Brownian particles, are presented in this chapter. After studying the relation between random walks and the Brownian motion, we present deterministic modeling of the Brownian motion to emulate the action of the Laplace-Beltrami operator without evolving or reconstructing the orientation distribution function. Several approaches to generating random walks on a sphere are proposed, which can

be readily applicable to the Lagrangian modeling presented above.

The numerical results are presented and discussed in Chapter 5. First, we study the orientation behavior of fibers in homogenous flows in one-way coupled simulations. Using the heat equation as a model problem, we compare random walk methods introduced in the previous chapter. The results of this section are published in [46]. The random walk formulations are then used to study the effect of fiber-fiber interactions in a three-dimensional homogeneous flow. After validating the two-way coupled solver in a simple geometry, we perform a numerical simulation of the fiber suspension flow in the three-dimensional axisymmetric contraction problem, considering the effect of fiber-fiber interactions.

The two-way coupled solver presented above is implemented into FEATFLOW, an open-source multi-purpose unstructured grid finite element code designed for solving the incompressible Navier-Stokes equations.

Chapter 2

Theory

A fiber suspension flow is a fluid medium that conveys immersed particles throughout its volume. Hence, the governing equations of both phases must be precisely described to give a comprehensive picture of the suspension.

In the first section, we introduce the underlying definitions and assumptions regarding the particle phase. The subsequent section covers the governing equations of fluid flows, followed by presenting the rheology of a fiber suspension flow.

2.1 Motion of rigid spheroidal particles

2.1.1 Basic definitions

In this work, a fiber refers to a rigid spheroidal particle, which is assumed to be neutrally buoyant, i.e., the average density of the fiber equals the density of the carrier fluid. As a consequence, the translation motion for the center of the fiber $\mathbf{x} \in \mathbb{R}^d$ is given by

$$\frac{d\mathbf{x}}{dt} = \mathbf{u}(\mathbf{x}), \quad \mathbf{x}(0) = \mathbf{x}^0, \tag{2.1}$$

where $\mathbf{u}(\mathbf{x})$ is the velocity of the flow at point $\mathbf{x}$.

A spheroid is an ellipsoid with two axes of equal length. In the Cartesian system, the surface of a spheroid is represented by

$$\frac{x^2+y^2}{a^2}+\frac{z^2}{c^2}=1, \tag{2.2}$$

where a and c are two distinct axis lengths. The spheroid is oblate if $a > c$ and prolate if $a < c$. In case $a = c$, the spheroid degenerates to a sphere. These three cases are shown in Fig. 2.1.

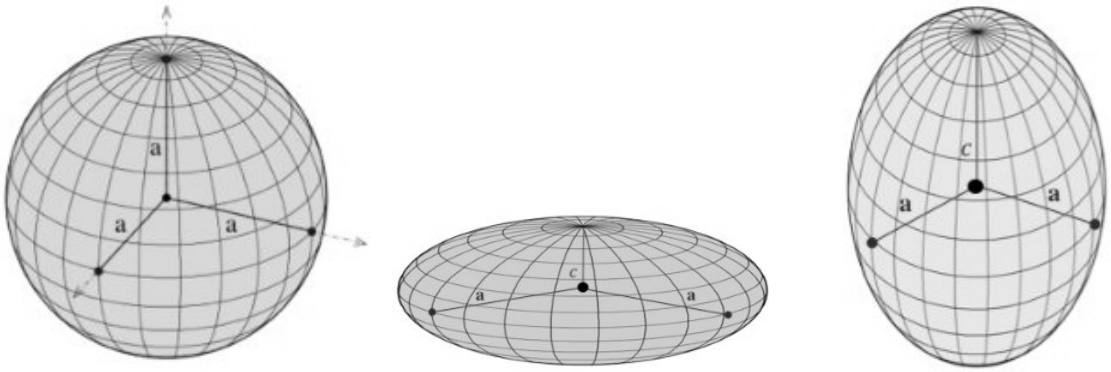

(a) (b) (c)

Figure 2.1: Schematics of (a) a sphere $c = a$, (b) an oblate spheroid $a > c$, and (c) a prolate spheroid $a < c$.

A fiber is assumed as a prolate spheroid with the aspect ratio $r = \frac{c}{a}$, which occupies the volume of

$$V_f = \frac{4}{3}\pi c a^2. \tag{2.3}$$

Fiber suspensions can be characterized based on the volume fraction ϕ and r into three different concentration regimes: dilute, semi-dilute, and concentrated. The suspension is considered dilute in case $\phi r^2 < 1$. If $\phi r < 1 < \phi r^2$, then it falls into the semi-dilute regime, and if $\phi r > 1$, the regime is defined as concentrated [47].

In three-dimensional space, the orientation of a fiber is defined by a unit vector $\mathbf{p} \in \mathbb{S}^2$, aligned to the major axis of the prolate (Fig. 2.2). This vector can be defined in terms of two angles θ and ϕ in spherical coordinates as

$$\mathbf{p} = \begin{pmatrix} p_1 \\ p_2 \\ p_3 \end{pmatrix} = \begin{pmatrix} \sin\theta\cos\varphi \\ \sin\theta\sin\varphi \\ \cos\theta \end{pmatrix}, \qquad \varphi \in [0, 2\pi), \quad \theta \in [0, \pi]. \tag{2.4}$$

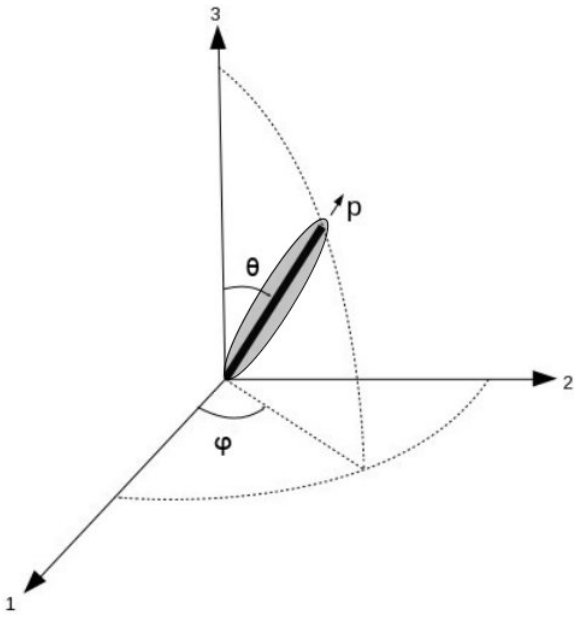

Figure 2.2: Orientation of a single fiber described by a unit vector $\mathbf{p}$ or the angles (φ, θ).

2.1.2 The Jeffery equation

The rotational motion of a fiber immersed in a homogeneous viscous flow depends on the local velocity gradients of the flow. Jeffery [7] proved the corresponding expression for the orientation change of the unit vector $\mathbf{p}$ in a dilute suspension as

$$\dot{\mathbf{p}} = \mathbf{W} \cdot \mathbf{p} + \lambda[\mathbf{D} \cdot \mathbf{p} - \mathbf{D} : (\mathbf{p} \otimes \mathbf{p}) \cdot \mathbf{p}], \tag{2.5}$$

where $\mathbf{D} = \frac{1}{2}[\nabla\mathbf{u} + (\nabla\mathbf{u})^T]$ and $\mathbf{W} = \frac{1}{2}[\nabla\mathbf{u} - (\nabla\mathbf{u})^T]$ are the strain rate tensor and the spin tensor respectively. $\lambda = (r^2 - 1)/(r^2 + 1)$ is a shape parameter depending on the aspect ratio of fibers.

The first term in the right-hand side of the Jeffery equation (2.5) makes fibers rotate with the vorticity of the flow while preserving the length of $\mathbf{p}$. The second term causes the orientation vector $\mathbf{p}$ to rotate in the direction of the maximum elongation rate. This term also preserves the length of $\mathbf{p}$ because the length change caused by the straining term $\mathbf{D} \cdot \mathbf{p}$ is projected back with term $\mathbf{D} : (\mathbf{p} \otimes \mathbf{p}) \cdot \mathbf{p}$. Hence, the Jeffery equation preserves the initial length of the orientation vector, i.e., $\|\mathbf{p}\| = 1$, where $\|\cdot\|$ denotes the Euclidean vector norm.

If $\lambda = 0$, the ellipsoid degenerates to a sphere that rotates only with the vorticity of the flow. If $\lambda = 1$, the fiber behaves as a slender rod. In such a case, the vorticity mentioned above and straining terms are balanced when the fiber reaches its steady state, i.e., aligned towards the flow direction. If $\lambda < 1$, the first term becomes dominant, which makes the fiber keep rotating after being aligned with the flow direction.

2.1.3 Orientation distribution function

In the Eulerian framework, the fiber orientation state can be described by a probability distribution function (PDF). In this context, PDF $\psi(\mathbf{p}; \mathbf{x}, t)$ is defined as the probability of finding a fiber parallel to the orientation vector $\mathbf{p} \in \mathbb{S}^{d-1}$, $d = \{2, 3\}$ at position $\mathbf{x} \in \mathbb{R}^d$ and time $t \geq 0$. The function must satisfy the normalization condition (conservation of fibers)

$$\int_{\mathbb{S}^{d-1}} \psi(\mathbf{p}; \mathbf{x}, t) d\mathbf{p} = 1, \tag{2.6}$$

and

$$\psi(\mathbf{p}; ., .) = \psi(-\mathbf{p}; ., .), \tag{2.7}$$

which shows the indistinguishability of the fiber's ends.

The evolution of the so-defined orientation distribution function is given by the following Fokker-Planck equation [11, 16]

$$\frac{\partial \psi}{\partial t} + \mathbf{u} \cdot \nabla \psi = -\nabla_p \cdot (\dot{\mathbf{p}} \psi), \tag{2.8}$$

where $\nabla_p \cdot$ is the divergence operator defined on the unit sphere.

Montgomery-Smith et al. [16] derived the analytical solution of this equation using the initial condition $\psi|_{t=0} = \psi_0$ as

$$\psi(\mathbf{p}) = \frac{\psi_0(C \cdot \mathbf{p}/|C \cdot \mathbf{p}|)}{(B : (\mathbf{p} \otimes \mathbf{p}))^{d/2}}, \tag{2.9}$$

where $B = C^T C$ and C satisfies

$$\frac{dC}{dt} = -C \cdot (\mathbf{W} + \lambda \mathbf{D}), \quad C|_{t=0} = I, \tag{2.10}$$

where I is the identity tensor.

Although the probability distribution function provides a comprehensive and unequivocal description of the fiber's orientation, solving the Fokker-Planck equation can be cumbersome, as it depends on two variables describing the orientation and three variables for the position. Furthermore, for the reasons given in section 2.1.5, finding an analytical solution is not feasible under some circumstances. Consequently, introducing a simplified but comprehensive description might be advantageous.

2.1.4 Orientation tensors

Fiber-induced stresses are commonly computed by a constitutive equation using orientation tensors. These tensors represent even-order moments of the orientation distribution function. Since the orientation distribution function is even, the odd-order integrals are zero (see condition (2.7)). The second- and fourth-order orientation tensors are defined as

$$\mathbf{A}(\mathbf{x},t) = \int_{\mathbb{S}^{d-1}} (\mathbf{p}\otimes\mathbf{p})\psi(\mathbf{p};\mathbf{x},t)d\mathbf{p}, \tag{2.11}$$

and

$$\mathbb{A}(\mathbf{x},t) = \int_{\mathbb{S}^{d-1}} (\mathbf{p}\otimes\mathbf{p}\otimes\mathbf{p}\otimes\mathbf{p})\psi(\mathbf{p};\mathbf{x},t)d\mathbf{p}. \tag{2.12}$$

Higher order tensors are not of interest as well, as it was shown that these two tensors could provide sufficient accuracy in most cases [11].

Assuming that the probability distribution function is available, in a 2D case, the integral in equations (2.11) and (2.12) can be split into m integrals

$$\begin{aligned} A_{ij} = &\int_0^{\frac{2\pi}{m}} \mathbf{p}_i\mathbf{p}_j\psi(\varphi)d\varphi + \int_{\frac{2\pi}{m}}^{\frac{4\pi}{m}} \mathbf{p}_i\mathbf{p}_j\psi(\varphi)d\varphi \ + \cdots \\ &+ \int_{\frac{(m-1)2\pi}{m}}^{2\pi} \mathbf{p}_i\mathbf{p}_j\psi(\varphi)d\varphi \end{aligned} \tag{2.13}$$

and

$$\begin{aligned} \mathbb{A}_{ijql} = &\int_0^{\frac{2\pi}{m}} \mathbf{p}_i\mathbf{p}_j\mathbf{p}_q\mathbf{p}_l\psi(\varphi)d\varphi + \int_{\frac{2\pi}{m}}^{\frac{4\pi}{m}} \mathbf{p}_i\mathbf{p}_j\mathbf{p}_q\mathbf{p}_l\psi(\varphi)d\varphi + \cdots \\ &+ \int_{\frac{(m-1)2\pi}{m}}^{2\pi} \mathbf{p}_i\mathbf{p}_j\mathbf{p}_q\mathbf{p}_l\psi(\varphi)d\varphi, \end{aligned} \tag{2.14}$$

where

$$\mathbf{p} = \begin{pmatrix} \cos\varphi \\ \sin\varphi \end{pmatrix}, \qquad \varphi \in [0, 2\pi). \tag{2.15}$$

Equation (2.13) can be numerically approximated, e.g., by Midpoint Rule

$$\int_{\psi_{k-1}}^{\psi_k} \mathbf{p}_i \mathbf{p}_j \psi(\varphi) d\phi = \frac{2\pi}{m} (\mathbf{p}_i^{mid} \mathbf{p}_j^{mid} \psi(\varphi_{k-\frac{1}{2}})), \tag{2.16}$$

where $\mathbf{p}^{mid}$ is the orientation of the midpoint of each integral's interval.

However, if the distribution function is not available, evaluating the orientation tensors using equations (2.11) and (2.12) requires solving the Fokker-Planck equation (2.8) beforehand, which makes it impossible to reduce the computational cost by evolving the tensors instead of ψ. Hence, two classes of approaches are introduced for evaluating the orientation tensors without the necessity of solving the Fokker-Planck equation.

Orientation tensors in the Eulerian approach

In the Eulerian approach, solving the Jeffery equation is not required because the behavior of each individual fiber is not of interest. Hence, an evolution equation for the second-order orientation tensor can be derived by taking the material derivative of equation (2.11) and invoking equations (2.5) and (2.8). The so-called Folgar-Tucker equation reads

$$\frac{\partial \mathbf{A}}{\partial t} + \mathbf{u} \cdot \nabla \mathbf{A} = (\mathbf{A} \cdot \mathbf{W} - \mathbf{W} \cdot \mathbf{A}) + \lambda (\mathbf{A} \cdot \mathbf{D} + \mathbf{D} \cdot \mathbf{A} - 2\mathbb{A} : \mathbf{D}). \tag{2.17}$$

The dependency of this equation on the fourth-order orientation tensor $\mathbb{A}$ in the right-hand side makes obtaining a closed-form solution impossible. Therefore, a closure formula is required to approximate $\mathbb{A}$ as a function of $\mathbf{A}$. A detailed investigation on the closures can be found, e.g., in [14, 15, 16, 48].

Orientation tensors in the Lagrangian approach

In the Lagrangian approach, the rotary movement of each fiber is tracked individually by solving the Jeffery equation (2.5). The presence of the orientation vector $\mathbf{p}$ for each fiber can be beneficial, as the orientation tensors can be evaluated without

the necessity of computing the orientation distribution function. The probability of having the orientation $\tilde{\mathbf{p}}$ is evaluated using the formula

$$\psi(\tilde{\mathbf{p}}) = \frac{1}{N_f} \sum_{i=1}^{N_f} \delta(\tilde{\mathbf{p}} - \mathbf{p}_l), \tag{2.18}$$

where δ is the Dirac delta function, N_f is the number of sampling fibers and $\mathbf{p}_l$ is the orientation of an individual fiber. Equation (2.18) satisfies condition (2.7) as follows [45]:

$$\begin{aligned} \int_{\mathbb{S}^{d-1}} \psi(\tilde{\mathbf{p}}) d\tilde{\mathbf{p}} &= \int_{\mathbb{S}^{d-1}} \frac{1}{N_f} \sum_{i=1}^{N_f} \delta(\tilde{\mathbf{p}} - \mathbf{p}_l) d\tilde{\mathbf{p}} \\ &= \frac{1}{N_f} \sum_{i=1}^{N_f} \int_{\mathbb{S}^{d-1}} \delta(\tilde{\mathbf{p}} - \mathbf{p}_l) d\tilde{\mathbf{p}} \\ &= \frac{1}{N_f} \sum_{i=1}^{N_f} 1 = 1. \end{aligned} \tag{2.19}$$

Substituting equation (2.18) into equation (2.11) yields

$$\begin{aligned} \mathbf{A}(\mathbf{x}, t) &= \int_{\mathbb{S}^{d-1}} (\tilde{\mathbf{p}} \otimes \tilde{\mathbf{p}}) \ \frac{1}{N_f} \sum_{i=1}^{N_f} \delta(\tilde{\mathbf{p}} - \mathbf{p}_l) d\tilde{\mathbf{p}} \\ &= \frac{1}{N_f} \sum_{i=1}^{N_f} \int_{\mathbb{S}^{d-1}} (\tilde{\mathbf{p}} \otimes \tilde{\mathbf{p}}) \ \delta(\tilde{\mathbf{p}} - \mathbf{p}_l) d\tilde{\mathbf{p}} \\ &= \frac{1}{N_f} \sum_{i=1}^{N_f} \mathbf{p}_i \mathbf{p}_i. \end{aligned} \tag{2.20}$$

The fourth-order orientation tensor can be evaluated similarly:

$$\mathbb{A}(\mathbf{x}, t) = \frac{1}{N_f} \sum_{i=1}^{N_f} \mathbf{p}_i \mathbf{p}_i \mathbf{p}_i \mathbf{p}_i. \tag{2.21}$$

2.1.5 Fiber-Fiber interaction

In addition to rotation with angular velocity governed by flow velocity gradients, fiber-fiber interactions may cause spontaneous changes in the orientation of fibers, in particular for non-dilute suspensions. Applying the theory of rotary Brownian motion, Hinch and Leal [25] showed that the evolution of the orientation distribution function may be described by following modified Fokker-Planck equation

$$\frac{\partial \psi}{\partial t} + \mathbf{u} \cdot \nabla \psi = -\nabla_p \cdot (\dot{\mathbf{p}} \psi) + D_r \Delta_p \psi, \tag{2.22}$$

in which the last term corresponds to the effect of fiber-fiber interactions, D_r is the *rotary diffusivity*, and Δ_p is the Laplace-Beltrami operator. Consequently, the evolution equation for the second-order orientation tensor is modified as follows:

$$\begin{aligned} \frac{\partial \mathbf{A}}{\partial t} + \mathbf{u} \cdot \nabla \mathbf{A} = (\mathbf{A} \cdot \mathbf{W} - \mathbf{W} \cdot \mathbf{A}) + \lambda(\mathbf{A} \cdot \mathbf{D} + \mathbf{D} \cdot \mathbf{A} - 2\mathbb{A} : \mathbf{D}) - 2\mathbb{A} : \mathbf{D}) \\ + D_r(6\mathrm{I} - 3\mathbf{A}). \end{aligned} \tag{2.23}$$

Whereas the already mentioned formulation is practical in the Eulerian approach, it is not efficiently applicable to the Lagrangian approach, in which the orientation tensors are evaluated using equations (2.20) and (2.21). The Jeffery equation is a fairly good model to describe the orientation of individual fibers in dilute suspensions. However, it may produce poor predictions as the concentration of fibers increases. The collisions between fibers cause sudden reorientations as they move through the flow field and rotate with the angular velocity. To incorporate the fiber-fiber interactions into the Jeffery equation, observing the fiber behavior in concentrated suspensions, Folgar and Tucker [47] proposed a diffusion-like term

$$\mathbf{q} = D_r \frac{1}{\psi} \nabla_p \psi, \tag{2.24}$$

which is explicitly added to the right-hand side of the Jeffery equation (2.5). They defined $D_r = C_I \dot{\gamma}$, where C_I is an empirical fiber-fiber interaction coefficient (discussed later in this section), and $\dot{\gamma} = (\mathbf{D} : \mathbf{D})^{1/2}$ is the scalar magnitude of the spin tensor. The surface gradient ∇_p can be written in spherical coordinates as follows:

$$\nabla_p = \frac{\partial}{\partial \theta} e_\theta + \frac{1}{\sin(\theta)} \frac{\partial}{\partial \phi} e_\phi. \tag{2.25}$$

In other words, the diffusion term corresponding to rotary Brownian motion in Hinch and Leal's interpretation is included in equation (2.22) and the Jeffery equation is

considered as its original form (2.5), whereas in Folgar and Tucker's definition, the Jeffery equation is modified closely analogous to rotary Brownian motion of small particles. Due to term $\nabla_p \cdot (\dot{\mathbf{p}}\psi)$ in equation (2.8), both interpretations lead to the same equation for the orientation distribution function (2.22), and consequently to the same evolution equation (2.23). The latter representation looks tangible if tracing the orientation of each fiber is of interest. However, the former provides a better understanding of the physics behind the interactions, which can be advantageous for employing the random walk theory discussed in Chapter 4.

Generally, orientation distribution function ψ can be thought of as the concentration of fibers at different orientations. Since term $\nabla_p \cdot (\dot{\mathbf{p}}\psi)$ is proportional to the gradient of the orientation distribution function, the term can cause a net motion of fibers away from the regions where they are highly aligned in a single direction to the regions where they are randomly oriented. The motion can be described in terms of a drift and a diffusive term (2.22). The former term can represent the influence of external forces such as shear forces, and the latter term can be understood as the rotary Brownian motion.

Although we do not solve the Fokker-Planck equation in the Lagrangian framework, we compute the orientation tensors, including fiber-fiber interactions, by incorporating term $\mathbf{q}$ into the Jeffery equation. As is shown later in Section 2.2.2, this is important because fiber-induced stresses are calculated using the orientation tensors, which in turn affect the velocity of fibers.

However, since the orientation distribution function is not available in the Lagrangian approach, direct computing of term $\mathbf{q}$ can be challenging. Function ψ can be obtained by solving equation (2.8) or reconstructing the orientation distribution function (see [49, 11]).

As discussed in [50], the reconstructed orientation distribution function might not be smooth enough, particularly in complex flows, where the orientation of fibers is subject to sudden changes. Fourier series (in 2D) and spherical harmonics (in 3D) can be used to smooth the distribution function and conveniently evaluate the gradient of ψ.

The distribution function ψ is non-negative and satisfies condition (2.6). Its Fourier series can be written in terms of the orientation angle ϕ as follows:

$$\psi_f(\phi) = a_0 + \sum_{n=1}^{\infty}(a_n \cos(n\phi) + b_n \sin(n\phi)), \tag{2.26}$$

where the Fourier coefficients are defined by

$$a_0 = \frac{1}{2\pi}\int_0^{2\pi} \psi(\phi)d\phi = \frac{1}{2\pi} \text{ (by 2.7)}, \tag{2.27a}$$

$$a_n = \frac{1}{\pi}\int_0^{2\pi} \psi(\phi)\cos(n\phi)d\phi, \tag{2.27b}$$

$$b_n = \frac{1}{\pi}\int_0^{2\pi} \psi(\phi)\sin(n\phi)d\phi. \tag{2.27c}$$

The Fourier coefficients can be calculated in the same way as integrals in equations (2.13) and (2.14). In view of representation (2.26), the derivative in the diffusion term (2.24) can be easily evaluated as

$$\frac{\partial \psi_f}{\partial \phi} = \sum_{n=1}^{\infty}(-a_n n\sin(n\phi) + b_n n\cos(n\phi)). \tag{2.28}$$

Note that the discretized diffusion term is transformed to the Cartesian coordinate system ($e_\phi = -\sin\phi e_x + \cos\phi e_y$) before being added to the Jeffery equation (2.5).

Another advantage of using the Fourier series representation is that the second- and fourth-order orientation tensors can be calculated from a small number of first Fourier coefficients. We have

$$\mathbf{A} = \frac{\pi}{2}\begin{pmatrix} 2a_0 + a_2 & b_2 \\ b_2 & 2a_0 - a_2 \end{pmatrix}, \tag{2.29}$$

$$\mathbb{A} = \frac{\pi}{8}\begin{pmatrix} 6a_0 + 4a_2 + a_4 & 2b_2 + b_4 & 2b_2 + b_4 & 2a_0 - a_4 \\ 2b_2 + b_4 & 2a_0 - a_4 & 2a_0 - a_4 & 2b_2 - b_4 \\ 2b_2 + b_4 & 2a_0 - a_4 & 2a_0 - a_4 & 2b_2 - b_4 \\ 2a_0 - a_4 & 2b_2 - b_4 & 2b_2 - b_4 & 6a_0 - 4a_2 + a_4 \end{pmatrix}, \tag{2.30}$$

as shown in detail by Lohmann [51]. A detailed description of spherical harmonics for the 3D case can be found, e.g., in [52]. However, the computational cost of the direct approach is significantly higher than that of approaches that evaluate the orientation tensors and term $\mathbf{q}$ without reconstructing the underlying orientation distribution function, such as random walk methods discussed in more detail in Chapter 4.

Concentration-dependent fiber interaction coefficient

The Folgar-Tucker constant C_I is an essential suspension property and must be determined experimentally [47]. Bay [53] measured this coefficient numerically by solving the Fokker-Planck equation with various C_I and then by evaluating the second-order orientation tensor to fit the experimental data. Bay found C_I in the range of around 10^{-2} and 10^{-4} and provided the following empirical equation

$$C_I = 0.0184exp(-0.7148r\phi). \tag{2.31}$$

However, it was shown by Bay that this equation is only reliable when $r\phi = O(1)$, which implies its validity only for concentrated regimes. Furthermore, the experimental data employed to obtain equation (2.31) were all for reinforced composites. Later, Phan-Thien et. al [27] improved the equation and introduced the following empirical equation

$$C_I = 0.03(1 - exp(-0.2248r\phi)), \tag{2.32}$$

which can evaluate the interaction coefficient with sufficient accuracy in dilute and semi-dilute regimes.

2.2 Governing equations of fluid flow

2.2.1 The Navier-Stokes equations

The Navier-Stokes equations for describing the motion of fluids for an incompressible flow read

$$\rho\frac{\partial \mathbf{u}}{\partial t} + \rho(\mathbf{u}\cdot\nabla)\mathbf{u} = -\nabla p + \nabla\cdot\tau + \mathbf{f}, \tag{2.33a}$$

$$\nabla\cdot\mathbf{u} = 0, \tag{2.33b}$$

where $\mathbf{u}$ is the flow velocity vector, p is the pressure, τ is the stress (deviator) tensor, composed of the shear stresses, and $\mathbf{f}$ represents external forces. The momentum equation (2.33a) is complemented with the second equation, called the continuity equation, which guarantees the conservation of mass. Solving these equations, along with the initial and boundary conditions, simulates an incompressible flow, in which it is assumed that the density of fluid ρ is constant.

Stress in flow can be classified into *normal* and *tangential* stresses. If we assume that fluids are composed of tiny particles, the pressure p is considered a normal stress that acts towards the surface and is perpendicular to it. The shear stresses, resulting from the friction between fluid layers moving at different velocities, act on the surface depending on the orientation of the surface relative to the flow direction.

The stress term can be modeled according to the physical properties of a fluid. In this regard, fluids are categorized into Newtonian and non-Newtonian fluids. In the Newtonian ones, the stress is assumed to be proportional to the deformation (strain) rate

$$\tau_N = 2\mu\mathbf{D} \tag{2.34}$$

where μ is the proportionality constant, called viscosity, which describes the fluid's resistance to flow. Since μ is constant throughout the fluid, the divergence of the stress term can be simplified to $\mu\Delta\mathbf{u}$.

In non-Newtonian fluids, the viscosity can change under force within the fluid, and the shear stress may not be directly proportional to the deformation rate as equation (2.34). Under some circumstances, the viscosity can also depend on the kinematic history of the fluid.

In the fiber suspension flow, the influence of fibers on the flow is taken into account by an additional non-Newtonian stress term. Hence, the stress term in equation (2.33) can be written as

$$\tau = \tau_N + \tau_{NN}, \tag{2.35}$$

which is discussed in the following section.

2.2.2 The rheology of fiber suspensions

The derivation of the constitutive equation relies on a scheme that involves solving the stress field around a single fiber with arbitrary translation and rotation. It is assumed that the fiber is not under any force or moment. Then, the influence of the fiber on the stress is obtained by examining the traction on the surface, followed by averaging the contribution of all fibers on the continuum scale [54].

Several constitutive models have been proposed for evaluating the contribution of the rheology of suspension into the non-Newtonian stress tensor.

Brenner [55] proposed a constitutive relation and showed that the rheological properties of the suspension depend on five material constants, the fluid's viscosity, and the orientation state of the particles. The rheological theory of Brenner

was developed for axisymmetric particles such as spherical dumbbells, double cones, spheroids, and circular cylinders. The general expression for the non-Newtonian stress tensor reads

$$\begin{aligned}\tau_{NN} &= 2\mu_0\mathbf{D} + \mu_1 I(\mathbf{D}:\mathbf{A}) + \mu_2\mathbb{A}:\mathbf{D} + 2\mu_3(\mathbf{A}\cdot\mathbf{D}+\mathbf{D}\cdot\mathbf{A}) \\ &\quad + 2\mu_4 D_r(3\mathbf{A}-I),\end{aligned} \tag{2.36}$$

where $\mu_0, ..., \mu_4$ are material constants reformulated by Moosaie [45] as

$$\mu_0 = 5\mu\phi Q_0, \tag{2.37a}$$
$$\mu_1 = 5\mu\phi Q_1, \tag{2.37b}$$
$$\mu_2 = 5\mu\phi Q_2, \tag{2.37c}$$
$$\mu_3 = 5\mu\phi Q_3, \tag{2.37d}$$
$$\mu_4 = 5\mu\phi Q_4, \tag{2.37e}$$

where

$$Q_0 = \frac{1}{5a'_{\parallel}}, \tag{2.38a}$$
$$Q_1 = \frac{2}{15a'_{\parallel}}\Big(1 - \frac{a''_{\parallel}}{a''_{\perp}}\Big), \tag{2.38b}$$
$$Q_2 = -4Q_3 - 3Q_1, \tag{2.38c}$$
$$Q_3 = \frac{1}{5a'_{\parallel}}\Big(-1 + \frac{2ra'_{\parallel}}{(r^2+1)a'_{\perp}}\Big), \tag{2.38d}$$
$$Q_4 = \frac{2(r^2-1)}{5(r^2a_{\parallel} + a_{\perp})}. \tag{2.38e}$$

Defining

$$ß = \frac{cosh^{-1}r}{r(r^2-1)^{1/2}}, \tag{2.39}$$

for prolate spheroids, one can evaluate the remaining unknowns as

$$a_{\parallel} = \frac{2}{r^2-1}(r^2ß - 1), \tag{2.40a}$$

$$a'_{\parallel} = \frac{r^2}{4(r^2-1)^2}(3ß + 2r^2 - 5), \tag{2.40b}$$

$$a''_{\parallel} = \frac{r^2}{4(r^2-1)^2}\Big[-(4r^2-1)ß + 2r^2 + 1\Big], \tag{2.40c}$$

$$a_{\perp} = \frac{r^2}{r^2-1}(-ß + 1), \tag{2.40d}$$

$$a'_{\perp} = \frac{r}{(r^2-1)^2}(-3r^2ß + 2 + r^2), \tag{2.40e}$$

$$a''_{\perp} = \frac{r^2}{(r^2-1)^2}\Big[(2r^2+1)ß - 3\Big]. \tag{2.40f}$$

As previously pointed out, the stress term in a non-Newtonian fluid is not directly proportional to the deformation rate. Nevertheless, equation (2.36) implies that this can be true under some circumstances. In such a case, an effective viscosity is evaluated to be added to the viscosity of the fluid. Therefore, the suspension is considered a Newtonian fluid with higher viscosity. As an example, for spherical particles, it is evident that $\mu_1 = \mu_2 = \mu_3 = \mu_4 = 0$ and $\mu_0 = \frac{5}{2}\mu\phi$. An effective viscosity then can be evaluated as

$$\mu_{eff} = \mu\Big(1 + \frac{5}{2}\phi\Big), \tag{2.41}$$

and consequently

$$\tau = 2\mu_{eff}D = 2\mu\Big(1 + \frac{5}{2}\phi\Big)D, \tag{2.42}$$

which resembles the Einstein's relation for including the effect of spherical particles in a Newtonian fluid.

Another significant outcome of Equation (2.36) is that an isotropic orientation state, i.e., fully random oriented fibers, can lead to a Newtonian flow with a higher viscosity than the carrier fluid's viscosity. Assuming an isotropic state, the second-order orientation tensor can be written as

$$\mathbf{A} = \begin{pmatrix} 1/3 & 0 & 0 \\ 0 & 1/3 & 0 \\ 0 & 0 & 1/3 \end{pmatrix}. \tag{2.43}$$

Moreover, an exact evaluation of the fourth-order orientation tensor can be obtained in an isotropic state, e.g., using a linear closure. Analogously to the previous case for spherical particles, it results in a direct relation between the stress tensor and the deformation rate [45]

$$\tau_{NN} = \Big(2\mu_0 + \frac{2}{15}\mu_2 + \frac{4}{3}\mu_3 + \frac{2}{5}\mu_4\Big)D, \tag{2.44}$$

which leads to a Newtonian stress term for an isotropic fiber suspension flow

$$\tau = 2\mu_{eff}D = 2\Big(\mu + \mu_0 + \frac{1}{15}\mu_2 + \frac{2}{3}\mu_3 + \frac{1}{5}\mu_4\Big)D. \tag{2.45}$$

It is worth mentioning that the effective viscosity of an isotropic fiber suspension flow with the aspect ratio $r = 100$ is 237.5 times higher than a suspension of spherical particles with the same volume fraction [45].

The finding above that an isotropic orientation state of a fiber suspension leads to a Newtonian flow with a higher viscosity can be of great importance, as it can be used to verify the flow solver. Any flow pattern for which an analytical solution exists, can be used in this regard, which is employed and discussed in Chapter 5.

Assuming the constitutive equation for the Non-Newtonian stress in a general form

$$\tau_{NN} = \mu\mathbf{D} + \mu\phi\Big[A(\mathbb{A} : \mathbf{D}) + B(\mathbf{D}\cdot\mathbf{A} + \mathbf{A}\cdot\mathbf{D}) + C\mathbf{D} + 2F\mathbf{A}D_r\Big], \tag{2.46}$$

several other theories have been proposed, which differ in the way the constants are obtained [54].

Dinh and Armstrong [56] proposed a model for cylindrical fibers, in which the constant A is evaluated by

$$A = \frac{(L_f/D)^2}{3\ln(2h_f/D)}, \tag{2.47}$$

where L_f and D are the length and diameter of fibers, respectively, and h_f represents the characteristic distance between an individual fiber and its nearest counterpart. In this theory, due to h_f's definition, the effect of fibers on the stress tensor is not a function of volume fraction. Furthermore, the fiber's thicknesses are ignored; consequently, the coefficients B and C are equal to zero [54].

Using an exact three-dimensional solution, Hinch and Leal [24] and Lipscomb et al. [10] found the material constants as follows:

$$A = \frac{r^2}{2(\ln 2r - 1.5)}, \tag{2.48a}$$

$$B = \frac{6\ln 2r - 11}{r^2}, \tag{2.48b}$$

$$C = 2, \tag{2.48c}$$

$$F = \frac{3r^2}{\ln 2r - 0.5}. \tag{2.48d}$$

The latter theory provides an accurate result for $r > 10$ [57]. However, it fails to predict the solution for oblate spheroids with $0 < r < 1$ and prolate spheroids if $r < 10$, whereas Brenner's model can cover the whole range with sufficient accuracy [45].

For slender fibers, i.e., $r \gg 1$, it is shown that constants B and C vanish, and no accuracy is lost by ignoring them [58]. Therefore, the expression for Non-Newtonian stress reduces to

$$\tau_{NN} = \mu\mathbf{D} + \mu\phi\Big[A(\mathbb{A} : \mathbf{D}) + 2F\mathbf{A}D_r\Big], \tag{2.49}$$

or

$$\tau_{NN} = \mu\mathbf{D} + \mu N_p(\mathbb{A} : \mathbf{D}) + 2\mu\phi F\mathbf{A}D_r, \tag{2.50}$$

where N_p is the particle number. This dimensionless number was first introduced by Evans [59] as

$$N_p = \frac{A\phi}{1 + C\phi} \overset{r\gg 1}{\approx} A\phi, \tag{2.51}$$

which is interpreted as the resistance of the suspension against elongation in the direction of fibers in comparison to the other form of deformations [58].

Chapter 3

Numerical Simulation Tools

The previous chapter described the basic assumptions regarding the motion of rigid spheroidal particles, referred to as fibers. Then, the governing equations of an incompressible flow were reviewed. It was then followed by presenting several rheological theories, which could incorporate the influence of the stress caused by the fiber's presence into the flow equations.

This chapter presents the numerical aspects of solving the Navier-Stokes equations and the equations describing the dynamics of fibers. Firstly, the Navier-Stokes equations are numerically discretized in time using Euler and Crank-Nicolson methods and in space using the finite element method. It is followed by a discussion of the discrete projection scheme for solving the Navier-Stokes equations. After presenting the numerical aspects of a fiber transport solver, two different approaches are employed for an implicit and an explicit treatment of fiber-induced stresses. It leads to describing the two-way coupled algorithm for the fiber suspension flow.

3.1 Flow solver

3.1.1 Time discretization

The Navier-Stokes equations can be discretized in time using the first-order backward or implicit Euler method as

$$\rho\frac{\mathbf{u}^{n+1}-\mathbf{u}^{n}}{\Delta t}+\rho(\mathbf{u}^{n+1}\cdot\nabla\mathbf{u}^{n+1})=-\nabla p^{n+1}+\nabla\cdot\tau^{n+1}+\mathbf{f}^{n}, \tag{3.1a}$$

$$\nabla\cdot\mathbf{u}^{n+1}=0. \tag{3.1b}$$

Notice that throughout this work, $\mathbf{f}$ refers to a source (or any other) term, which is treated explicitly hereafter.

Moreover, a ϑ-scheme can be considered a flexible and robust choice, which allows mixing the above methods and switching between them if it is needed. It reads

$$\rho\frac{\mathbf{u}^{n+1}-\mathbf{u}^{n}}{\Delta t}+\vartheta\mathbf{B}(\mathbf{u}^{n+1})+(1-\vartheta)\mathbf{B}(\mathbf{u}^{n})=0,\quad 0\leq\vartheta\leq 1 \tag{3.2a}$$

$$\nabla\cdot\mathbf{u}^{n+1}=0, \tag{3.2b}$$

where

$$\mathbf{B}(\mathbf{u}^{n+1})=\rho(\mathbf{u}^{n+1}\cdot\nabla\mathbf{u}^{n+1})+\nabla p^{n+1}-\nabla\cdot\tau^{n+1}-\mathbf{f}^{n}, \tag{3.3a}$$

$$\mathbf{B}(\mathbf{u}^{n})=\rho(\mathbf{u}^{n}\cdot\nabla\mathbf{u}^{n})+\nabla p^{n}-\nabla\cdot\tau^{n}-\mathbf{f}^{n}. \tag{3.3b}$$

In cases $\vartheta=0$ and $\vartheta=1$, one obtains the forward Euler and the backward Euler methods, respectively. If $\vartheta=\frac{1}{2}$, the Crank-Nicolson method with second-order accuracy in time is achieved.

3.1.2 The Finite Element Method

The finite element method (FEM) is a well-known numerical approach to discretizing Navier-Stokes equations in space. It is widely used in order to deal with complex geometries and partial differential equations (PDEs) due to its flexibility and robustness.

The first step in the finite element method is breaking down the bounded domain $\Omega\subseteq\mathbb{R}^d$, $d\in\{1,2,3\}$ into smaller subdomains to obtain the finite element mesh $\mathcal{T}_h$, often called a *triangulation*. Note that it can refer to, e.g., quadrilateral, tetrahedra, or hexahedra elements and not necessarily triangle meshes. While the union of the elements $K\in\mathcal{T}_h$ forms the closure of the domain $\bar{\Omega}$, there must not be any overlap between them. For a rigorous overview of the definitions and conditions regarding a triangulation, see [15].

Let us recall the Navier-Stokes equations (2.33) from Chapter 2:

$$\rho\frac{\partial \mathbf{u}}{\partial t} + \rho(\mathbf{u}\cdot\nabla)\mathbf{u} = -\nabla p + \nabla\cdot\tau + \mathbf{f}, \tag{3.4a}$$

$$\nabla\cdot\mathbf{u} = 0, \tag{3.4b}$$

Since the strong form of equations (3.4) requires high regularity of the solution in the whole domain, the PDE is written in an integral form called the weak formulation, which allows us to obtain a more flexible and efficient numerical approximation. In the FEM, the weak form is obtained by multiplying the equation with an arbitrary function, the so-called test function, and then integrating over bounded domain Ω. Let us define a vector-valued test function $\boldsymbol{v} \in V$ for the momentum equation (3.4a) and a scalar-valued function $\omega \in W$ for the continuity equation (3.4b), where $V \coloneqq \left[H_0^1(\Omega)\right]^d$ and $W \coloneqq L_0^2(\Omega)$ denote the functional spaces to which velocity and pressure belong, respectively. Note that the numerical solution and the test functions may not necessarily live in the same space, but in this work, we use this setting employed in the standard *Galerkin method*.

Let Γ be the boundary of the domain divided into the Dirichlet boundary Γ_D and the Neumann boundary Γ_N, where $\Gamma_D \cap \Gamma_N = \emptyset$. The Dirichlet boundary condition fixes the velocity at the boundary as

$$\mathbf{u} = \mathbf{g}, \text{ on } \Gamma_D, \tag{3.5}$$

which can be used, e.g., at the inflow. For the outflow, one can define the homogeneous Neumann boundary condition "Do-Nothing" [60] as

$$(\tau - pI)\mathbf{n} = 0, \tag{3.6}$$

where $\mathbf{n}$ is the unit outward normal to Γ.

Multiplying the Navier-Stokes equations for the Newtonian flow by continuously differentiable test functions associated with the classical solution, performing integration by parts, and invoking the boundary condition (3.6), the weak formulation reads

$$\int_\Omega \rho \frac{\partial \mathbf{u}}{\partial t} \cdot \boldsymbol{v} d\Omega + \int_\Omega \rho(\mathbf{u} \cdot \nabla)\mathbf{u} \cdot \boldsymbol{v} d\Omega = \int_\Omega p(\nabla \cdot \boldsymbol{v}) d\Omega \tag{3.7a}$$

$$- \int_\Omega \tau : \nabla \boldsymbol{v} d\Omega + \int_\Omega \mathbf{f} \cdot \boldsymbol{v} d\Omega,$$

$$\int_\Omega (\nabla \cdot \mathbf{u}) \omega d\Omega = 0. \tag{3.7b}$$

The element spaces for velocity and pressure are chosen such that they meet the inf-sup condition, the so-called *Ladyzhenskaya–Babuška–Brezzi* (LBB) condition [61], which guarantees that the chosen velocity and pressure elements are compatible. Throughout this work, the LBB-stable Q_2/P_1 element pair (see Fig. 3.1) is used, which is known as a robust and accurate pair. For a comprehensive review, see [62, 63, 64].

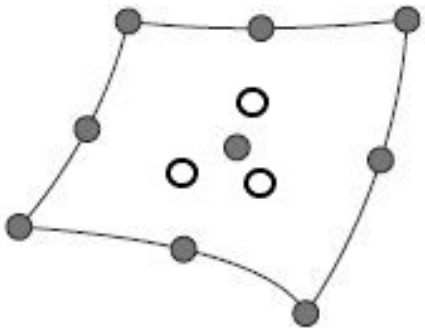

Figure 3.1: A Q_2/P_1 element pair, in which filled and empty circles correspond to velocity and pressure degrees of freedom, respectively.

Subsequently, we define finite dimensional subspaces of V and W in the case of the Q_2/P_1 pair as follows [65]:

$$V_h = \left\{ \boldsymbol{v}_h \in V, \boldsymbol{v}_{h|K} \in \left[Q_2(K) \right]^d \right\}, \tag{3.8a}$$

$$W_h = \left\{ w_h \in W, w_{h|K} \in P_1(K) \right\}. \tag{3.8b}$$

Next, let us define the discrete solution to (3.7) as

$$\mathbf{u}_h = \sum_{j=1}^{N_u} u_j \boldsymbol{v}_j, \qquad p_h = \sum_{j=1}^{N_p} p_j \omega_j, \tag{3.9}$$

where N_u and N_p are the total number of nodes and u_j and ω_j are the nodal values. Note that *nodes* refer to vertices of $K \in \mathcal{T}_h$ in this work. The so-called basis functions $\boldsymbol{\upsilon}_j$ and ω_j are the bases of the approximation spaces V_h and W_h, respectively.

Consequently, the discretized form of the weak formulation (3.7) can be written as

$$\int_\Omega \rho \frac{\partial \mathbf{u}_h}{\partial t} \cdot \boldsymbol{\upsilon}_h d\Omega + \int_\Omega \rho(\mathbf{u}_h \cdot \nabla)\mathbf{u}_h \cdot \boldsymbol{\upsilon}_h d\Omega = \int_\Omega p_h \nabla \cdot \boldsymbol{\upsilon}_h d\Omega - \int_\Omega \tau_h : \nabla \boldsymbol{\upsilon}_h d\Omega + \int_\Omega \mathbf{f} \cdot \boldsymbol{\upsilon}_h d\Omega, \tag{3.10a}$$

$$\int_\Omega (\nabla \cdot \mathbf{u}_h)\omega_h d\Omega = 0. \tag{3.10b}$$

Discretizing the weak formulation (3.10) in time leads to the following discrete form:

$$Mu + \Delta t\big(N(u)u + Lu\big) + \Delta t B p = f, \tag{3.11a}$$

$$B^T u = 0, \tag{3.11b}$$

where $M = (m_{ij})_{i,j=1}^{N_u}, m_{ij} = \int_\Omega \upsilon_j \upsilon_i d\Omega$ is the *consistent* mass matrix, and f is a load vector, which contains the terms treated explicitly. The matrices N and L are associated with the nonlinear convective term and the diffusive term, respectively (see (3.10)). Hence, the fully discrete form of the problem is expressed as the following nonlinear saddle point system

$$\begin{bmatrix} A & \Delta t B \\ B^T & 0 \end{bmatrix} \begin{bmatrix} u \\ p \end{bmatrix} = \begin{bmatrix} f \\ 0 \end{bmatrix}, \tag{3.12}$$

where u and p are the vectors of unknowns, the discrete gradient operator B is a $N_u \times N_p$ matrix with fixed coefficients, and A is an $N_u \times N_u$ matrix consisting of convective, diffusive, and mass operators, which are a function of velocity at the current time step.

Solving the saddle point system (3.12) is challenging, mainly due to the nonlinearity of the convective term and the coupling between the velocity and pressure. In the following section, we present the discrete projection scheme and a nonlinear solution technique to address these challenges.

3.1.3 Discrete projection scheme

The (linearized) saddle point system (3.12) can be solved using direct or iterative methods. The direct ones are costly and require large amounts of memory, while iterative ones might converge slowly when there is a large number of unknowns. Hence, it is preferable to use the discrete projection method, a type of operator splitting methods, which decomposes the coupled system into simpler and smaller steps.

The main idea of this approach is to split the momentum equation from the continuity equation, which leads to the Poisson equation for pressure. This approach can be summarized as follows:

1. Solve the discrete nonlinear momentum equation to obtain the intermediate velocity field $\tilde{u}$ as

$$A\tilde{u} = f - \Delta t B p^l. \tag{3.13}$$

   The velocity obtained in this step does not satisfy the continuity equation, i.e., it is not necessarily (discretely) divergence-free.

2. Solve the Poisson equation in the form of the Schur complement formulation introduced by Turek [66, 67] as

$$B^T M_L^{-1} B\tilde{q} = \frac{1}{\Delta t} B^T \tilde{u}, \tag{3.14}$$

   where the lumped mass matrix is defined as $M_L = m_{ij} = \delta_{ij} \int_\Omega \upsilon_i d\Omega$.

3. Correct and update the pressure field

$$p^{l+1} = p^l + \alpha\tilde{q}, \tag{3.15}$$

   where α is a damping parameter.

4. Project the intermediate velocity field

$$u^{l+1} = \tilde{u} - \Delta t M_L^{-1} B\tilde{q}, \tag{3.16}$$

   to obtain the discretely divergence-free vector field u^{n+1}.

For further reading on the discrete projection scheme, see [66, 67, 68, 15].

Nonlinear solution techniques

The fixed point iteration and the Newton iteration are well-known methods widely used to treat the nonlinearity of the convection term in the Navier-Stokes equations. In this work, the nonlinear equation (3.13) is linearized using the following iterative approach

$$u^k = u^{k-1} + \omega C^{-1} r^{k-1}, \tag{3.17}$$

where k is the index of the iteration loop, ω is a damping factor and the *defect* r is defined as $r = f - Au$. Matrix C is a preconditioner matrix, which would be constructed as $C = A$ or include only part of A. However, the matrix should be constructed cautiously, as an inappropriate choice can lead to a slow convergence rate, poor accuracy, and increased computational cost. The loop can be stopped, e.g., when previous iterates do not influence the solution significantly or when the residual norm is decreased sufficiently.

Geometric Multigrid solver

The choice of linear solvers for the linear equation in the nonlinear iterates and the Poisson equation can be of great importance, as they represent the costly part of the algorithm mentioned above. Multigrid solvers have become one of the most efficient and robust approaches, which can provide remarkably good convergence rates. In what follows, we present the geometric Multigrid solver, which can be appropriately implemented with block-structured grids.

The main principle of geometric Multigrid solvers is to discretize the problem into a sequence of fine to coarse grids. In coarse grids, a low-frequency error is seen as a high-frequency one, which can be filtered out quickly. The general idea of a basic two-grid *V-cycle* is presented as follows:

1. Apply a few presmoothing steps in order to get a first approximation to the solution of the linear system. With this aim, one can use typical iterative solvers as smoothers such as SSOR, SOR, or Jacobi to damp the residual in the current level.

2. Compute the residual and restrict it to the next coarser grid.

3. Solve the system in the course grid to obtain the correction.

4. Interpolate back (prolongate) the calculated correction to the finer grid.

5. Apply a few postsmoothing steps to calculate the final solution.

Note that the basic V-cycle can be extended to more grids to achieve faster convergence. It is worth mentioning that an appropriate choice for restriction, prolongation, and smoothers, as well as the number and the type of the Multigrid cycles, can significantly influence the efficiency of the solver. For a detailed discussion, see [67, 69, 70].

3.2 Fiber dynamics solver

In the previous section, the structure of a flow solver was described, by which the discretely divergence-free velocity field is calculated. In this section, we discuss the numerical aspects of the dynamics of fibers.

3.2.1 The translation motion

Let us recall equation (2.1)

$$\frac{d\mathbf{x}}{dt} = \mathbf{u}(\mathbf{x}), \quad \mathbf{x}(0) = \mathbf{x}^0,$$

by which the motion of an individual fiber can be tracked. This equation is discretized in time using the explicit Euler approach.

In order to evaluate the velocity of the flow at the fiber's position, the element at which the fiber is located is identified. Then, the following approximation on the (reference) element is performed as

$$u^k(\boldsymbol{\zeta}) = \sum_{i=1}^{N_L} u_i^k \hat{v}_i^k(\boldsymbol{\zeta}), \quad k = 1, ..., d, \tag{3.18}$$

where d is the space dimension, N_L is the number of nodes in an element, i.e., 27 for a $3D$ $Q2$ element, and $\boldsymbol{\zeta}$ denotes coordinates (in the reference configuration).

In the FEM framework, it is more convenient and more efficient to map the element domain to a reference element domain. As a consequence, the formulas for basis functions as well as their derivatives, become independent of the element's shape and thus will be the same for all elements. For further reading on the mapping and the reference element, see [67, 71, 68].

3.2.2 The rotational motion

Evaluating the strain rate tensor and the spin rate tensor in the Jeffery equation

$$\dot{\mathbf{p}} = \mathbf{W} \cdot \mathbf{p} + \lambda[\mathbf{D} \cdot \mathbf{p} - \mathbf{D} : (\mathbf{p} \otimes \mathbf{p}) \cdot \mathbf{p}],$$

cannot be performed using approximation (3.18) due to the discontinuity in the first derivative of the piecewise tri-quadratic basis functions across the boundaries of mesh cells. In order to have a continuous field, given a function $f \in L^2(\Omega)$, the L^2-projection of $P_h f \in V_h$ is defined by:

$$\int_\Omega (f - P_h f)\upsilon d\Omega = 0, \forall \upsilon \in V_h. \tag{3.19}$$

Inserting $P_h f = \sum_{j=1}^{N_u} c_j \upsilon_j$ into equation (3.19), the discrete system is written as

$$\int_\Omega (\sum_{j=1}^{N} c_j \upsilon_j)\upsilon_i d\Omega = \int_\Omega f \upsilon_i d\Omega, \tag{3.20}$$

or equivalently

$$\sum_{j=1}^{N} c_j \int_\Omega \upsilon_j \upsilon_i d\Omega = \int_\Omega f \upsilon_i d\Omega. \tag{3.21}$$

Hence, the coefficients c_j are determined by solving the following discrete system:

$$Mx = b. \tag{3.22}$$

In order to build the strain rate tensor, for the sake of clarity, let us split the velocity gradient tensor into its constituent partial derivatives and define

$$f_{kl} = \frac{\partial u_h^k}{\partial x_l} = \sum_{j=1}^{N_u} u_j^k \frac{\partial \upsilon_j^k}{\partial x_l}. \tag{3.23}$$

To approximate the integral in the right-hand side of equation (3.21) using a quadrature rule, the integral is decomposed into element contributions, and the value of f

is interpolated to the cubature points of the reference element. Notice that evaluating the integral over the reference element has to be done with caution due to the change of variables theorem, as there are two coordinate systems. After the assembling procedure, equation (3.22) is solved d^2 times to provide the continuous fields.

It is worth mentioning that the values of basis functions and their partial derivatives are interpolated to the cubature points of the reference element only once at the start of the simulation. Due to the chain rule, evaluating the value of the derivative of the basis functions in the reference element has to be performed by taking the Jacobian of the transformation into consideration.

After evaluating all partial derivatives at nodes, the strain and spin rate tensors can now be interpolated to the position of the fiber using

$$\Big(\frac{\partial u^k}{\partial x^l}\Big)_h(\boldsymbol{\zeta}) = \sum_{i=1}^{N_L} \Big(\frac{\partial u^k}{\partial x^l}\Big)_i \hat{v}_i(\boldsymbol{\zeta}). \tag{3.24}$$

Notice that the value of the local basis functions for all indices k, l are taken to be the same.

In case the Reynolds number of the flow is high and the flow solver is stable for large time steps, the explicit time descritization for tracking the translation and the rotational motion might not provide an accurate solution. In such a case, exploiting a different time discretization technique or using a separate time step from the one in the flow solver can be beneficial. On the other hand, if the flow solver requires a very small time step, the equations mentioned above can be solved only after every few iterations of the flow solver, which can save significant computational costs.

3.2.3 The orientation tensors

As described in Chapter 2, the orientation tensors are needed to compute the stress tensors and can be stochastically approximated as follows:

$$\mathbf{A}(\mathbf{x}, t) = \frac{1}{N_f} \sum_{i=1}^{N_f} \mathbf{p}_i \mathbf{p}_i, \tag{3.25}$$

and

$$\mathbb{A}(\mathbf{x}, t) = \frac{1}{N_f} \sum_{i=1}^{N_f} \mathbf{p}_i \mathbf{p}_i \mathbf{p}_i \mathbf{p}_i. \tag{3.26}$$

The orientation tensors can be evaluated at any position in the domain, e.g., at the nodal points. Approximately, the influence of a fiber's orientation on a certain point of the flow field is inversely proportional to its distance from the point. Consequently, the fibers located only within a certain distance of the point are selected for the approximation. The distance can be a function of the mesh size, e.g., with a radius length of one or two element edges. Notice that the accuracy of the approximation strongly depends on the number of samples, which will be studied in Chapter 5.

3.2.4 Fiber-induced stress tensor

As described in Chapter 2, an additional non-Newtonian stress term is required to be evaluated to include the influence of the fibers on the flow.

Let us rewrite the weak formulation (3.7) as follows:

$$\int_\Omega \rho \frac{\partial \mathbf{u}_h}{\partial t} \cdot \boldsymbol{v}_h d\Omega + \int_\Omega \rho(\mathbf{u}_h \cdot \nabla)\mathbf{u}_h \cdot \boldsymbol{v}_h d\Omega = \int_\Omega p_h(\nabla \cdot \boldsymbol{v}_h) d\Omega \tag{3.27a}$$
$$- \int_\Omega \tau_N^h : \nabla \boldsymbol{v}_h d\Omega - \int_\Omega \tau_{NN}^h : \nabla \boldsymbol{v}_h d\Omega + \int_\Omega \mathbf{f} \cdot \boldsymbol{v}_h d\Omega,$$
$$\int_\Omega (\nabla \cdot \mathbf{u}_h)\omega d\Omega = 0. \tag{3.27b}$$

We treat the additional term $\int_\Omega \tau_{NN}^h : \nabla \boldsymbol{v}_h d\Omega$ using two different approaches discussed in the following sections.

The explicit approach

The main idea of this approach is to add the fiber-induced stress tensor as a source term to the Navier-Stokes equations. Hence, we treat integral $\int_\Omega \tau_{NN}^h : \nabla \boldsymbol{v}_h d\Omega$ as an explicit term and incorporate it into the load vector of the subproblem (3.13).

More specifically, describing the nonlinear solution technique given in Section 3.1.3 in more detail as

$$u^k = u^{k-1} + \omega u_u, \quad k = 0, 1, 2, ... \quad , \tag{3.28a}$$
$$u_u = C^{-1}(f - Au)^{k-1}, \tag{3.28b}$$
$$u_u = C^{-1} r^{k-1}, \tag{3.28c}$$
$$C u_u = r^{k-1}, \tag{3.28d}$$

we add the calculated vectors to the so-defined defect r.

As described in Chapter 2, the constitutive equations for the fiber-induced stress tensor are a function of the orientation and the strain rate tensors. Therefore, we evaluate the orientation tensors using equations (3.25) and (3.26), and follow the procedure described in Section 3.2.2 to calculate the strain rate tensors. Consequently, we compute all components of the non-Newtonian stress tensor using a constitutive equation, e.g., the one proposed by Brenner [55] as follows:

$$\begin{aligned}\tau_{ij} &= 2\mu_0 d_{ij} + \mu_1 \delta_{ij}(a_{ij}d_{ji}) + \mu_2 \underline{\underline{a}}_{ijkl} d_{kl} + 2\mu_3(a_{ik}d_{kj} + d_{ik}a_{kj}) \\ &\quad + 2\mu_4 D_r(3a_{ij} - \delta_{ij}).\end{aligned} \tag{3.29}$$

Note that the products are written using the convention of summation over repeated indices. It is worth mentioning that the strain rate tensor and the orientation tensors are symmetric; hence the order of indices in the products can obey different conventions proposed in the literature.

Decomposing the integral $\int_\Omega \tau^h_{NN} : \nabla \boldsymbol{\upsilon}_h d\Omega$ into element contributions and applying a quadrature rule, the element load vector, from which the global load vector is assembled, can be evaluated as

$$f^n_i = \int_{\hat{\Omega}_e} \sum_{j=1}^{d} \tau^n_{ij} \frac{\partial \hat{\upsilon}^n}{\partial x_j} |\det J| d\hat{\Omega} = \sum_{c=1}^{N_c} \sum_{j=1}^{n_d} w^c \tau_{ij}(\boldsymbol{\zeta}^c) \frac{\partial \hat{\upsilon}^n}{\partial x_j}(\boldsymbol{\zeta}^c) |\det J|, \tag{3.30}$$

where $n = 1, 2, ..., N_L$, $i = 1, ..., d$, w^c denotes the weight of the quadrature rule, and N_c is the number of cubature points used for the numerical integration. The value of the stress tensors at the cubature points ($\boldsymbol{\zeta}^c$) is computed using interpolation formula (3.18).

For an introduction to the global assembly procedure, see [68, 72].

The implicit approach

As described in Chapter 2, by neglecting the rotary diffusivity $D_r = 0$ for slender fibers $r \gg 1$, the expression for the non-Newtonian stress tensor reduces to

$$\tau = 2\mu N_p \mathbb{A} : \mathbf{D}, \tag{3.31}$$

or equivalently

$$\tau_{ij} = 2\mu N_p \underline{\underline{a}}_{ijkl} d_{kl}. \tag{3.32}$$

Inserting (3.31) into the integral under study $\int_\Omega \tau^h_{NN} : \nabla \boldsymbol{v}_h d\Omega$, we have

$$\begin{aligned} \int_\Omega \tau_h : \nabla \boldsymbol{v}_h d\Omega &= 2\mu N_p \int_\Omega (\mathbb{A} : \mathbf{D}(\mathbf{u}_h)) : \mathbf{D}(\boldsymbol{v}_h) d\Omega \\ &= 2\mu N_p \int_\Omega (\underline{\underline{a}}_{ijkl} \frac{\partial u^k_h}{\partial x_l}) \frac{\partial v^i}{\partial x^j} d\Omega, \end{aligned} \tag{3.33}$$

where $D(\mathbf{u}_h)$ and $D(\boldsymbol{v}_h)$ are symmetric. Decomposing the integral into element contributions and extracting the coefficient vector, the element (local) stress matrix S^{mn}_{ik} for a reference element Ω_e is computed as follows:

$$S^{mn}_{ik} = 2\mu N_p \int_{\Omega_e} (\underline{\underline{a}}_{ijkl} \frac{\partial \hat{v}^m}{\partial x_l}) \frac{\partial \hat{v}^n}{\partial x_j} |detJ| d\Omega, \tag{3.34}$$

where $m, n = 1, 2, ..., N_L$ and $i, j, k, l = 1, ..., d$. The integral on the right-hand side can be numerically approximated analogously to that described in (3.30).

Subsequently, we incorporate the stress matrix into matrix A of subproblem (3.13).

Some notes on the explicit and implicit treatments

As already described, the explicit approach does not include the fiber-induced stress into matrix A. The simplification involved in this approach might make the system very unstable, whereas the implicit approach provides a stable solution even for large time steps. However, since the preconditioner matrix C is constructed based on A (see Section 3.1.3), solving the linear system $Cu_u = r$ is faster in the explicit case due to the sparsity of matrix C. The fiber-induced stress tensor added to the preconditioner in the implicit approach is not necessarily isotropic, which can make solving the linear system at each nonlinear iterate much slower. Furthermore, constructing the stress tensor, particularly at each nonlinear iterate, is costly. In other words, although the implicit approach can offer the advantage of using large time steps, the time spent at each time step might offset the benefit.

Moreover, there may be cases where using very small time steps is required due to other sources of instability. If both approaches provide a stable solution for a given time step, the explicit approach can be more efficient.

It is worth mentioning that the explicit approach offers the benefit of being readily applicable to any constitutive equation for the non-Newtonian stress tensor, no matter whether or not its contribution to the Jacobian of the Navier-Stokes system is easily computable. The implicit approach may be difficult to implement, particularly when $D_r \neq 0$ or if it is anisotropic, whereas, in the explicit approach, the fiber-induced stress is treated in a black-box fashion.

The two-way coupled fiber suspension flow

In the previous sections, we introduced the numerical algorithms of the flow and fiber solvers. Let us now summarize the algorithm for solving the two-way coupled fiber suspension flow in a segregated manner for one time step as follows:

1. Solve the Navier-Stokes system as described in Section 3.1.3 to obtain the discretely divergence-free velocity field.
2. Update the position and the orientation vector of fibers using the velocity from the previous step as described in Sections 3.2.1 and 3.2.2.
3. Following the procedures presented in Section 3.2.4, compute the fiber-induced stress tensor using an arbitrarily chosen constitutive equation (in the explicit approach), or evaluate the fourth-order orientation tensors (in the implicit approach), and incorporate the results into subproblem (3.13).
4. Go to the next time step.

Chapter 4

The Random Walk

Using the theory of rotational Brownian motion, Hinch and Leal [24] showed that the effect of the fiber-fiber interactions could be taken into account using an additional rotary diffusion term added to the Fokker-Planck equation, by which the orientation distribution function evolves. The theory is concerned with the random motion of small particles, so-called Brownian particles, suspended in a fluid. The fluid is made up of a huge number of tiny particles, which randomly interact with each other in all directions. These interactions make the Brownian particle jiggle in random directions, which leads to an observable diffusion effect. Using the assumption that the average density of fibers is equal to the density of the carrier fluid, the theory of rotational Brownian motion is emulated to model the fiber-fiber interactions.

In the Lagrangian framework, evaluating the rotary diffusion term using a direct approach requires either solving the Fokker-Planck equation or reconstructing the orientation distribution function. Since they are computationally expensive, in this chapter, we employ a stochastic approach and design random walks, to emulate the action of the rotary diffusion term. The main idea is to add stochastic perturbations to the orientations of Lagrangian fibers to achieve the same effect as using the diffusion term in the Fokker-Planck equation [73, 74].

The content of this chapter is based on [46] and is organized as follows. In the first section, after introducing the basic assumptions and definitions of Brownian motion, we present the formulation of a diffusion equation for Brownian particles, followed by studying the relation between random walks and Brownian motion. We focus then on Brownian motion on the sphere $\mathbb{S}^{d-1}$, $d \geq 2$. Restricting our attention to the rotary diffusive term added to the Fokker-Planck equation, deterministic modeling of the Brownian motion is presented in Section 4.2. Section 4.3 is devoted to the

practical approaches to implementing random walks.

4.1 The Brownian motion

Brownian motion is the random movement of tiny particles suspended in a fluid. Einstein [75] provided a theoretical analysis of Brownian motion and argued that the motion is due to the bombardment of the small particle with the water molecules. Whereas Einstein formulated a diffusion equation for Brownian particles, Wiener [76] constructed a rigorous stochastic model for the Brownian motion with the required properties.

It is worth mentioning that stochastic processes can be employed to model the processes that might not have inherent randomness. Ignoring the quantum mechanics, the forces which originate Brownian motion can be determined precisely. However, the system's complexity can lead to using a stochastic model.

A stochastic process is simply a collection of discrete or continuous random variables indexed by time. A standard Brownian motion (also known as a Wiener process) $B(t)$, $t \in [0, \infty)$ is a continuous stochastic process that has the following properties:

- $B(0) = 0$;
- It has stationary and independent increments;
- It has normal (so-called Gaussian) distribution;

For any fixed t and s, the expected (or mean) value and the variance of a standard Brownian process are defined as follows:

$$\mathbb{E}[(B(t+s) - B(t))] = \mathbb{E}[B(t)] = 0,$$

$$\mathrm{Var}[B(t)] = t,$$

$$\mathrm{Var}[B(t+s) - B(s)] = \mathbb{E}[(B(t+s) - B(t))^2] = s.$$

In this work, uppercase letters refer to random variables, and lowercase letters correspond to their deterministic counterparts. For example, Θ is a discrete random variable and θ is a deterministic one. Θ is a set of numbers corresponding to a random event, e.g., a coin toss. Similarly, $\theta(t)$, $t \in [0, \infty)$ is a deterministic continuous trajectory, whereas $\Theta(t)$, $t \in [0, \infty)$ is a stochastic process, which is a set of continuous trajectories.

4.1.1 Brownian motion and the Laplacian

It is well-known that $L = \frac{1}{2}\Delta$ is the infinitesimal generator of the d-dimensional Brownian motion [77]. The generator is a partial differential operator, which can be used, e.g., to derive partial differential equations relevant to stochastic processes. Restricting our attention to the Brownian motion, which satisfies the stochastic differential equation $dX(t) = dB(t)$, the infinitesimal generator L of the process is given by

$$Lf(x) = \lim_{t\to 0^+} \frac{\mathbb{E}^x[f(X_t)] - f(x)}{t}, \tag{4.1}$$

on the subspace defined as

$$D(L) = \left\{ f \in C_0^2 : \lim_{t\to 0^+} \frac{\mathbb{E}^x[f(X_t)] - f(x)}{t} \text{ exists} \right\}.$$

Note that in the stochastic calculus, the generator is defined for a wide class of stochastic processes (where $D(L)$ is defined on the subspace C_0). In this work, however, we limit the definition of the generator to the Brownian motion and do not elaborate on the other stochastic processes.

Rewriting formula (4.1) as

$$\lim_{t\to 0^+} \mathbb{E}^x[f(X_t)] - f(x) - tLf(x) = \lim_{t\to 0^+} t\left[\frac{\mathbb{E}^x[f(X_t)] - f(x)}{t} - Lf(x)\right] = 0,$$

we obtain the following approximation for small $t \geq 0$:

$$\mathbb{E}^x[f(X_t)] \approx f(x) + tLf(x).$$

Intuitively, $Lf(x)$ describes how fast $f(X_t)$ changes with respect to t and in the sense of $\mathbb{E}^x$.

Denoting $P_t f(x)$ as the expected value of $f(X_t)$ started at x at time 0, i.e., $P_t f(x) := \mathbb{E}^x[f(X_t)]$, we have

$$\frac{d}{dt} P_t f(x) = L P_t f(x). \tag{4.2}$$

Using the fact that the Brownian motion has independent increments, the above equation is derived as follows:

$$\frac{d}{dt} P_t f(x) = \lim_{h\to 0} \frac{P_{t+h} f(x) - P_t f(x)}{h} = \lim_{h\to 0} P_t \left(\frac{P_h f(x) - f(x)}{h}\right).$$

Rewriting (4.1) as

$$Lf(x) = \lim_{t \to 0^+} \frac{P_t f(x) - f(x)}{t}, \tag{4.3}$$

we obtain

$$\frac{d}{dt} P_t f(x) = P_t L f(x) = L P_t f(x).$$

For a one-dimensional Brownian motion $B(t)$, the expected value of $f(B(t))$ using Taylor's formula is approximated as

$$\mathbb{E}^x[f(B(t))] \approx \mathbb{E}^x \left[f(x) + f'(x)(B(t) - x) + \frac{1}{2} f''(x)(B(t) - x)^2 \right].$$

Since $f(x)$ is deterministic, we have

$$\mathbb{E}^x[f(B(t))] \approx f(x) + f'(x)\mathbb{E}^x \left[(B(t) - x) \right] + \frac{1}{2} f''(x)\mathbb{E}^x \left[(B(t) - x)^2 \right].$$

By definition, $\mathbb{E}^x$ is the expectation of the process started at point x; therefore,

$$\mathbb{E}^x[B(t) - x] = 0,$$

$$\mathbb{E}^x[(B(t) - x)^2] = t.$$

It follows that:

$$\mathbb{E}^x[f(B(t))] \approx f(x) + \frac{t}{2} f''(x). \tag{4.4}$$

Note the difference between the expectation of the Brownian motion and its standard version. The generator captures the behavior of the process started at different positions, which makes studying the general case more reasonable.

Using $u(x,t) := \mathbb{E}^x[f(B(t))]$, let us rewrite equation (4.2) as

$$\frac{d}{dt} u(x,t) = Lu(x,t). \tag{4.5}$$

Substituting approximation (4.4) into the left-hand side of (4.5)

$$\frac{d}{dt} u(x,t) = \frac{f''(x)}{2} = Lu(x,t),$$

we can see that $u(x,t)$ is the solution of the heat equation

$$\frac{\partial}{\partial t}u(x,t) = \frac{1}{2}\frac{\partial^2}{\partial x^2}u(x,t), \qquad (x,t) \in \mathbb{R} \times \mathbb{R}_+,$$
$$u(x,0) = f(x).$$

Substituting definition $L = \frac{1}{2}\Delta$ into (4.5) could also directly prove the conclusion.

Whereas the above formulations can develop intuitions regarding the generator and its relation to the heat equation, we refer to Example 7.9 of [77] for a rigorous derivation of $L = \frac{1}{2}\Delta$ and Lemma 8.1 of [77] for a rigorous proof that $u(x,t)$ is the *unique* solution of the heat equation.

One can also check that the normal distribution of a (rescaled) $d-$dimensional Brownian particle, which has an initial position of $X(0) = 0$ at $t = 0$

$$f(\mathbf{x},t) = \left(\frac{1}{2\sqrt{Dt\pi}}\right)^d e^{\frac{-\|\mathbf{x}\|^2}{4Dt}}, \tag{4.6}$$

is the solution to the heat equation

$$\frac{\partial f}{\partial t}(\mathbf{x},t) = D\Delta f(\mathbf{x},t), \qquad (\mathbf{x},t) \in \mathbb{R}^d \times \mathbb{R}_+, \tag{4.7}$$

$$f(\mathbf{x},0) = \delta(\mathbf{0}), \tag{4.8}$$

where δ is the delta distribution. The variance or mean square displacement of the distribution is evaluated as follows [73]:

$$\sigma_d^2(t) = \int_{\mathbb{R}^d} \|\mathbf{x}\|^2 f(\mathbf{x},t)\,\mathrm{d}\mathbf{x} = 2dDt. \tag{4.9}$$

For any $t > 0$, the position of a Brownian particle is a (d-dimensional) random variable with mean $\mathbf{0} \in \mathbb{R}^d$ and variance (also known as covariance matrix) $2Dt\mathbf{I}$, where $\mathbf{I}$ is the identity matrix. Note that the covariance matrix has zero off-diagonal entries under the assumption that the Brownian motion can be split into d independent one-dimensional standard Brownian motion. The term *standard deviation* is defined in terms of variance, which is the square root of the trace of the covariance matrix, i.e., $\sigma_d(t) = \sqrt{2dDt}$. The underlying stochastic process is given by

$$X(t) = \sigma B(t), \tag{4.10}$$

where $\sigma = \sqrt{2D}$, and $B(t) = (B_1(t), B_2(t), \ldots, B_d(t))$ contains d copies of independent one-dimensional standard Brownian motions.

4.1.2 Brownian motion and the random walk

Whereas the Brownian motion is a continuous stochastic process, a random walk is defined as a discrete process with independent increments. Brownian motion can be described as a macroscopic picture of a Brownian particle jiggling in a $d-$dimensional space. At a microscopic level, the particle performs discrete random displacements, let us call it random walks, caused by interacting with other solvent molecules. Using Donsker's invariance principle (also known as the functional central limit theorem), we can show that the random walks converge in distribution to the Brownian motion. The word *invariance* refers to the fact that all random walks with mean 0 and variance σ^2, regardless of their distributions, converge to the same Brownian motion [78].

Let X_i, $i \in \mathbb{N}$ be a sequence of i.i.d (independent, identically distributed) random variables normalized such that it has zero mean and variance σ^2. Note that this assumption can be justified for any sequence with a finite variance without loss of generality since it can always be normalized as follows [79]:

$$\frac{X_i - \mathbb{E}[X_i]}{\sqrt{\mathrm{Var}(X_i)}}.$$

Assuming that each random variable X_i corresponds to a one-dimensional displacement of a moving particle at discrete time step Δt

$$X_i = \begin{cases} \sigma\sqrt{\Delta t}, & \text{with probability } 0.5, \\ -\sigma\sqrt{\Delta t}, & \text{with probability } 0.5, \end{cases} \tag{4.11}$$

the corresponding random walk generated by the sequence is given by

$$S_n = \sum_{i=1}^{n} X_i, \quad n \in \mathbb{N}.$$

It is worth mentioning that $\sigma\sqrt{n\Delta t} = \sigma\sqrt{t}$ describes how far the particle deviates from its original position in time t. It is an informal description of the standard deviation evaluated for the Brownian motion in the previous section. Since the random variables are independent, the variance of the random walk is calculated using the sum of the variance of each random variable as follows:

$$\mathrm{Var}(\sum_{i=1}^{n} X_i) = \sum_{i=1}^{n} \mathrm{Var}(X_i) = \sigma^2 t.$$

To obtain the process in continuous time, let us perform a linear interpolation between the integer points

$$Y(t) = S_{\lfloor t/\Delta t \rfloor} + (t - \lfloor t/\Delta t \rfloor \Delta t) X_{\lfloor t/\Delta t \rfloor + 1},$$

where $\lfloor . \rfloor$ is the floor function and $Y \in \mathcal{C}[0, \infty)$. Defining a fixed time-step $\Delta t = 1/k$, Donsker's theorem demonstrates that the rescaled function

$$Y_k(t) = \sqrt{\Delta t} Y(t),$$

converges to one-dimensional Brownian motion $B(t)$ with variance $\sigma^2 t$ as $k \to \infty$.

4.1.3 Brownian motion on a circle

A variance-σ^2 Brownian motion on a circle can be defined as

$$X(t) = (X_1(t), X_2(t)) = (\cos(\sigma B(t)), \sin(\sigma B(t))), \tag{4.12}$$

where $B(t)$ is a one-dimensional standard Brownian motion.

Let $f \in \mathcal{C}^2(\mathbb{R})$, the Taylor formula applied to $f(B(t))$ is written as

$$\begin{aligned} df(B(t)) = f'(B(t))dB(t) + \frac{1}{2} f''(B(t))(dB(t))^2 + \\ \frac{1}{3!} f^3(B(t))(dB(t))^3 + \frac{1}{4!} f^4(B(t))(dB(t))^4 + \cdots . \end{aligned} \tag{4.13}$$

It should be noted that stochastic calculus forms its own branch of mathematics. Whereas small terms of order larger than two in deterministic calculus can be neglected, the small increment of Brownian motion of order two $(dB(t))^2$ is no longer negligible. Using the heuristic rule $(dB(t))^2 \approx dt$ and neglecting terms $(dt)^2$ and $dtdB(t) \approx \pm(dt)^{\frac{3}{2}}$, the Taylor formula for the Brownian motion can be given by

$$df(B(t)) = f'(B(t))dB(t) + \frac{1}{2} f''(B(t))dt. \tag{4.14}$$

Note that for small increment of $dB(t) \approx dt^a$, a choice of $a \in (0, \frac{1}{2})$ leads to a vanishing process as dt tends to zero, whereas for any $a > \frac{1}{2}$ the process would explode [80].

Applying Taylor's formula (4.14) to (4.12) with $f_1(B(t)) = \cos(\sigma B(t))$ and $f_2(B(t)) = \sin(\sigma B(t))$ we obtain

$$dX_1(t) = -\sigma \sin(\sigma B(t))dB(t) - \frac{\sigma^2 \cos(\sigma B(t))}{2} dt,$$

$$dX_2(t) = \sigma \cos(\sigma B(t))dB(t) - \frac{\sigma^2 \sin(\sigma B(t))}{2}dt.$$

Equivalently

$$dX_1(t) = -\sigma X_2(t)dB(t) - \frac{\sigma^2 X_1(t)}{2}dt,$$

$$dX_2(t) = \sigma X_1(t)dB(t) - \frac{\sigma^2 X_2(t)}{2}dt.$$

The corresponding stochastic differential equation in matrix form is given by

$$dX(t) = \sigma K X(t)dB(t) - \frac{\sigma^2}{2}X(t)dt, \tag{4.15}$$

where

$$K = \begin{pmatrix} 0 & -1 \\ 1 & 0 \end{pmatrix}.$$

The standard Brownian motion, by which the process is defined on the circle, lacks any deterministic term (the so-called drift term). However, equation (4.15) contains a drift term, which represents a deterministic motion towards the origin. In other words, the drift term is a correction that pushes the tangential random motion back onto the circle.

A practical formula for the generator operator L of a stochastic process X, which satisfies the stochastic differential equation of the form

$$dX_t = b(X_t)dt + \sigma(X_t)dB_t, \tag{4.16}$$

is given by [81]

$$Lf(x) = \sum_i b_i(x)\frac{\partial f}{\partial x_i} + \frac{1}{2}\sum_{i,j}(\sigma\sigma^T)_{i,j}(x)\frac{\partial^2 f}{\partial x_i \partial x_j}. \tag{4.17}$$

Hence, the generator of process X obtained by (4.15) in the Cartesian coordinates is given by

$$Lf = \frac{\sigma^2}{2}\left(-x_1\frac{\partial f}{\partial x_1} - x_2\frac{\partial f}{\partial x_2} + x_2^2\frac{\partial^2 f}{\partial x_1^2} - 2x_1x_2\frac{\partial^2 f}{\partial x_1 \partial x_2} + x_1^2\frac{\partial^2 f}{\partial x_2^2}\right).$$

Equivalently

$$Lf = \frac{\sigma^2}{2}\left(-x_1\frac{\partial f}{\partial x_1} - x_2\frac{\partial f}{\partial x_2} + \Delta f - x_1^2\frac{\partial^2 f}{\partial x_1^2} - 2x_1x_2\frac{\partial^2 f}{\partial x_1 \partial x_2} - x_2^2\frac{\partial^2 f}{\partial x_2^2}\right).$$

Looking at the generator at the two-dimensional North Pole $(x_1, x_2) = (0, 1)$ of the unit circle, Lf reduces to

$$Lf = \frac{\sigma^2}{2}\left(-\frac{\partial f}{\partial x_2} + \frac{\partial^2 f}{\partial x_1^2}\right). \tag{4.18}$$

It is aligned with the abovementioned observation regarding equation (4.15). Term $\frac{\partial^2 f}{\partial x_1^2}$ is the horizontal diffusion of a Brownian particle, and term $-\frac{\partial f}{\partial x_2}$ is the generator of vertical displacements, which projects back the particle on the unit circle. Changing of variables, the generator in polar coordinates reads

$$Lf = \frac{\sigma^2}{2}\frac{\partial^2 f}{\partial \theta^2}. \tag{4.19}$$

4.1.4 Brownian motion on a sphere

The Brownian motion on the sphere $\mathbb{S}^{d-1}$, $d \geq 2$ can be physically thought of as the random motion of a Brownian particle in a fluid, in which the particle is constrained to move only within a thin film of the surface of the sphere formed by the fluid.

There are many different methods to construct the Brownian motion on the sphere. For example, it can be constructed by employing a particular time change [81] or using the Stratonovich form of the stochastic differential equation [82, 83]. The processes can be defined to be a diffusion on the unit sphere whose generator is given by $\frac{1}{2}\Delta_p$ (Δ_p is the Laplace-Beltrami operator), which is expressed in the Cartesian coordinates as

$$Lf = \frac{\sigma^2}{2}\left(-(d-1)\sum_{i=1}^{d} x_i\frac{\partial f}{\partial x_i} + \Delta f - \sum_{i,j=1}^{d} x_i x_j \frac{\partial^2 f}{\partial x_i \partial x_j}\right). \tag{4.20}$$

It is worth mentioning that one of the definitions by which Brownian motion on a Riemannian manifold (M, g) is constructed is that its generator is $\frac{1}{2}\Delta_g$ [81]. Similarly, Brownian motion on the sphere can be defined as a stochastic process

whose probability distribution function is the heat kernel associated with the Laplace-Beltrami operator [84]. We do not elaborate on the construction methods in this work.

At the $d-$dimensional North Pole $(x_1, x_2, \dots) = (0, 0, \dots, 1)$ the Cartesian form of the generator Lf reduces to

$$Lf = \frac{\sigma^2}{2} \sum_{i=1}^{d-1} \left(-\frac{\partial f}{\partial x_d} + \frac{\partial^2 f}{\partial x_i^2} \right) = \frac{\sigma^2}{2} \left(-(d-1) \frac{\partial f}{\partial x_d} + \Delta_{d-1} f \right), \tag{4.21}$$

where Δ_{d-1} is the Laplacian operator defined on the manifold of the first $d-1$ space dimensions.

Restricting our attention to the unit sphere $\mathbb{S}^2$ and making a change of variables, we obtain the generator in spherical coordinates $0 \leq \theta \leq \pi$, $0 \leq \varphi < 2\pi$ as

$$Lf = \frac{\sigma^2}{2} \left(\frac{1}{\sin\theta} \frac{\partial}{\partial \theta} \left(\sin\theta \frac{\partial f}{\partial \theta} \right) + \frac{1}{\sin^2\theta} \frac{\partial^2 f}{\partial \varphi^2} \right). \tag{4.22}$$

4.2 Deterministic modeling of Brownian diffusion

Let us recall the Fokker-Planck equation

$$\frac{\partial \psi}{\partial t} + \mathbf{u} \cdot \nabla \psi + \nabla_p \cdot (\dot{\mathbf{p}} \psi) - D_r \Delta_p \psi = 0,$$

by which the evolution of the orientation distribution function is described. In the absence of spatial gradients, the Fokker-Planck equation reduces to the spherical heat equation

$$\frac{\partial \psi}{\partial t} = D_r \Delta_p \psi \qquad \text{on } \mathbb{S}^2. \tag{4.23}$$

Restricting the Laplace operator in spherical coordinates

$$\Delta = \frac{1}{r^2} \frac{\partial}{\partial r} \left(r^2 \frac{\partial}{\partial r} \right) + \frac{1}{r^2 \sin\theta} \frac{\partial}{\partial \theta} \left(\sin\theta \frac{\partial}{\partial \theta} \right) + \frac{1}{r^2 \sin^2\theta} \frac{\partial^2}{\partial \phi^2}, \tag{4.24}$$

to the unit sphere, the simplified formula for the Laplace-Beltrami operator is given by

$$\Delta_p = \frac{1}{\sin\theta} \frac{\partial}{\partial \theta} \left(\sin\theta \frac{\partial}{\partial \theta} \right) + \frac{1}{\sin^2\theta} \frac{\partial^2}{\partial \phi^2}. \tag{4.25}$$

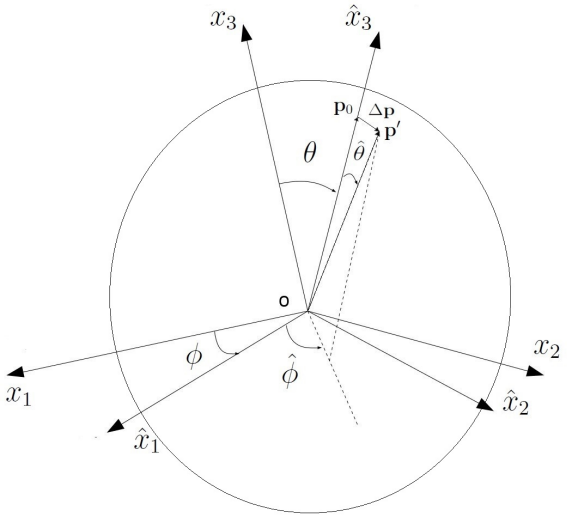

Figure 4.1: New coordinate system $\{\hat{x}_1, \hat{x}_2, \hat{x}_3\}$ in which $\mathbf{p}_0 = (0, 0, 1)^T$, cf. [43].

Due to the complication of solving equation (4.23), let us define another coordinate system $\{\hat{x}_1, \hat{x}_2, \hat{x}_3\}$ (see Fig. 4.1) using a change of variables

$$(x_1, x_2, x_3) \mapsto (\hat{x}_1, \hat{x}_2, \hat{x}_3), \quad (\theta, \varphi) \mapsto (\hat{\theta}, \hat{\varphi}),$$

such that the unit vector $\hat{e}_3 = (0, 0, 1)^T$ is co-directed to fiber orientation vector $\mathbf{p}_0$ and $\hat{x}_1$ is in the direction of the cross product of $\hat{x}_3$ and x_3. Note that $\mathbf{p}_0$ corresponds to the orientation of fibers rotated by the velocity gradients of the flow in the absence of the rotary diffusivity. Assuming all fibers have the same initial orientation vector $\mathbf{p}_0$ at $t = 0$, we have

$$\psi(\mathbf{p}, 0) = \delta(\mathbf{p}_0), \quad \mathbf{p}_0 \in \mathbb{S}^2. \tag{4.26}$$

In the new reference frame, since the rotation of a fiber around its symmetry axis $\hat{x}_3$ does not change its orientation, the probability distribution function and the initial condition become independent of the polar angle $\hat{\phi}$, i.e., $\psi = f(\hat{\theta}, t)$ for $t > 0$. It follows that:

$$\hat{\Delta}_p \psi = \frac{1}{\sin\hat{\theta}} \frac{\partial}{\partial\hat{\theta}} \left(\sin\hat{\theta} \frac{\partial\psi}{\partial\hat{\theta}} \right), \tag{4.27}$$

which leads to a simplification of the initial value problem

$$\frac{\partial\psi}{\partial t} = D_r \hat{\Delta}_p \psi, \qquad (\hat{\theta}, t) \in [0, \pi] \times \mathbb{R}_+, \tag{4.28}$$

$$\psi(\hat{\theta}, 0) = \frac{1}{2\pi \sin\hat{\theta}} \delta(\hat{\theta}_0), \tag{4.29}$$

of which the exact solution is given by [43, 85]

$$\psi(\hat{\theta}, t) = \frac{1}{2\pi} \sum_{0}^{\infty} (2n+1) \exp[-n(n+1) D_r t] \times P_n(cos(\hat{\theta})), \tag{4.30}$$

where P_n is the Legendre polynomial of degree n.

Equivalently, the initial value problem can be written in the Cartesian coordinates. By the chain rule, given $f := g \circ (x, y, z)$ and assuming the appropriate differentiability, we have

$$\begin{aligned} \frac{\partial f}{\partial \theta} &= \frac{\partial g}{\partial x}\frac{\partial x}{\partial \theta} + \frac{\partial g}{\partial y}\frac{\partial y}{\partial \theta} + \frac{\partial g}{\partial z}\frac{\partial z}{\partial \theta} \\ &= \cos\phi\cos\theta\frac{\partial g}{\partial x} + \sin\phi\cos\theta\frac{\partial g}{\partial y} - \sin\theta\frac{\partial g}{\partial z}, \end{aligned}$$

In the new reference frame, by the aforementioned rotational symmetry around $\hat{x}_3$, i.e., $\psi = f(\hat{x}_3, t)$, $\hat{x}_3 = \cos\hat{\theta}$, we obtain

$$\frac{\partial \psi(\hat{\theta}, t)}{\partial \hat{\theta}} = -\sin\hat{\theta}\frac{\partial \psi(\hat{x_3}, t)}{\partial \hat{x}_3}.$$

It follows that:

$$\hat{\Delta}_p \psi = \frac{\partial}{\partial \hat{x}_3}\left(\sin^2\hat{\theta}\frac{\partial \psi}{\partial \hat{x}_3}\right) = \frac{\partial}{\partial \hat{x}_3}\left((1 - \hat{x_3^2})\frac{\partial \psi}{\partial \hat{x}_3}\right), \tag{4.31}$$

and, therefore, the initial value problem can be rewritten as

$$\frac{\partial \psi}{\partial t} = D\frac{\partial}{\partial \hat{x}_3}\left((1 - \hat{x}_3^2)\frac{\partial \psi}{\partial \hat{x}_3}\right), \qquad (\hat{x}_3, t) \in [-1, 1] \times \mathbb{R}_+, \tag{4.32}$$

$$\psi(\hat{x}_3, 0) = \delta(1), \tag{4.33}$$

of which the exact solution is given by

$$\psi(\hat{x}_3, t) = \sum_{n=0}^{\infty} \frac{2n+1}{2} \exp\left(-n(n+1) D_r t\right) P_n(\hat{x}_3). \tag{4.34}$$

An accurate evaluation of ψ using equation (4.30) or (4.34) can lead to an expensive task of summation over a large number of terms, particularly in the case of small time steps. As an alternative, following Chen and Yu [43], if $D_r t \ll 1$ and $\hat{\theta} \ll 1$, one can use approximation $\sin\hat{\theta} \approx \hat{\theta}$, which leads to the simplified problem

$$\frac{\partial \psi}{\partial t} = D_r \frac{1}{\hat{\theta}} \frac{\partial \psi}{\partial \hat{\theta}} \left(\hat{\theta} \frac{\partial \psi}{\partial \hat{\theta}} \right), \tag{4.35}$$

of which the solution is given by

$$\psi(\hat{\theta}, t) = \frac{1}{4\pi D_r t} \exp\left(-\frac{\hat{\theta}^2}{4 D_r t} \right). \tag{4.36}$$

Whereas this approximation provides accurate results efficiently, it is only limited to cases with small time steps. For larger time steps, we will employ equations (4.30) and (4.34) by proposing an approach based on generating a *lookup* table, which reduces the computational cost by replacing a *runtime* computation with an array indexing operation.

4.3 Implementation of random walks

In order to model the rotary diffusion term stochastically, let us formulate the problem as the updates of the form

$$\mathbf{p}_m^{n+1} = \mathbf{p}_m^n + \Delta \mathbf{p}_m^n, \qquad m = 1, \ldots, N_f, \quad n = 0, 1, \ldots, \tag{4.37}$$

where $\Delta \mathbf{p}_m$ is a random perturbation such that $\mathbf{p}_m + \Delta \mathbf{p}_m \in \mathbb{S}^2$ for $\mathbf{p}_m \in \mathbb{S}^2$. Let us recall that $\mathbf{p}_m^n$ corresponds to the orientation of fibers rotated using the Jeffery equation, by which the length of the orientation vectors are preserved, i.e., $\|\mathbf{p}_m^n\| = 1$.

In this section, we propose different approaches to evaluate random perturbation vectors $\Delta \mathbf{p}_m$ on the unit sphere $\mathbb{S}^2$. As equations (4.18) and (4.21) admit, the Brownian motion on the sphere $\mathbb{S}^{d-1}$ can be constructed using the standard random walk on the $(d-1)$-dimensional tangential manifold, followed by a projection to get back to $\mathbb{S}^{d-1}$. Therefore, we discuss first how to construct perturbations $\Delta \mathbf{p}_m$ based on the standard random walk in $\mathbb{R}^d$. It is then followed by formulating two projection-based approaches. Finally, exploiting the second fiber-aligned coordinate system defined in Section 4.2, we generate the random walk directly on $\mathbb{S}^2$.

4.3.1 Standard random walk in $\mathbb{R}^d$

We defined $S_n = \sum_{i=1}^{n} X_i$, $n \in \mathbb{N}$, as a random walk generated by i.i.d random variables X_i on the interval $[-\frac{1}{2}, \frac{1}{2}]$. We evaluate the variance of S_n as

$$\text{Var}\left(\sum_{i=1}^{n} X_i\right) = \mathbb{E}\left(\left[\sum_{i=1}^{n} X_i\right]^2\right) - \left[\mathbb{E}\left(\sum_{i=1}^{n} X_i\right)\right]^2.$$

Since the random walk has zero mean, $\left[\mathbb{E}\left(\sum_{i=1}^{n} X_i\right)\right]^2 = 0$. We have

$$\begin{aligned}\mathbb{E}\left(\left[\sum_{i=1}^{n} X_i\right]^2\right) = \mathbb{E}\left(\sum_{i=1}^{n}\sum_{j=1}^{n} X_i X_j\right) &= \sum_{i=1}^{n}\sum_{j=1}^{n} \mathbb{E}(X_i X_j) \\ &= \sum_{i=1}^{n} \mathbb{E}[X_i^2] + \sum_{i=1}^{n}\sum_{\substack{j=1 \\ j\neq i}}^{n} \mathbb{E}[X_i X_j],\end{aligned} \tag{4.38}$$

where $\mathbb{E}[X_i X_j] = \mathbb{E}[X_i]\mathbb{E}[X_j]$ for any independent random variables. It leads to a further simplification of the above equation since $\mathbb{E}[X_i] = \mathbb{E}[X_j] = 0$.

Suppose X is a continuous random variable on $[a, b]$. Using the *law of the unconscious statistician* [86], the expected value of $g(X)$ is given by

$$\mathbb{E}[g(X)] = \int_a^b g(x) f_X(x) dx, \tag{4.39}$$

where $f_X(x)$ is the probability distribution function of X. Since X_i is uniformly distributed on $[-\frac{1}{2}, \frac{1}{2}]$, i.e., $f(x) = \frac{1}{b-a} = 1$, we calculate

$$\mathbb{E}[X^2] = \int_{-\frac{1}{2}}^{\frac{1}{2}} x^2 dx = \frac{1}{12}. \tag{4.40}$$

Therefore, for a random walk at time t with the discrete time step Δt, we have

$$\mathbb{E}\left[\left(\sum_{i=1}^{n} X_i\right)^2\right] = \mathbb{E}\left[\sum_{i=1}^{n} X_i^2\right] = \frac{n}{12} = \frac{t}{12\Delta t}.$$

Random walks generated in $\mathbb{R}^d$ can be split into d independent random walks in $\mathbb{R}$. Hence, multiplying each X_i with the same scaling factor $\xi \in \mathbb{R}_+$, the variance of the d-dimensional random walk is given by

$$\sigma^2_{d_{RW}}(t) = \frac{d\xi^2 t}{12\Delta t}. \tag{4.41}$$

This variance can be fitted to its deterministic counterpart $\sigma^2_d(t) = 2dDt$ defined by (4.9) using an appropriate scaling factor, i.e.,

$$\xi = \sqrt{24 D_r \Delta t}.$$

Hence, an increment of a Cartesian random walk, e.g., in the case $d = 3$, can be evaluated by

$$\Delta\tilde{\mathbf{p}} = \begin{pmatrix} \Delta p_1 \\ \Delta p_2 \\ \Delta p_3 \end{pmatrix} = \begin{pmatrix} \xi X_1 \\ \xi X_2 \\ \xi X_3 \end{pmatrix}, \tag{4.42}$$

where X_i, $i = 1, 2, 3$ are i.i.d random variables uniformly distributed on $[-\frac{1}{2}, \frac{1}{2}]$. Note that $\mathbf{p} + \Delta\tilde{\mathbf{p}} \notin \mathbb{S}^2$.

4.3.2 Random walk on $\mathbb{S}^1$

As shown in Section 4.1.3, the Brownian motion on a circle can be defined as $X(t) = (X_1(t), X_2(t)) = (\cos(\sigma B(t)), \sin(\sigma B(t)))$, which leads to the generator $Lf = \frac{\sigma^2}{2}\frac{\partial^2 f}{\partial \theta^2}$ in the polar coordinates. Therefore, transforming the orientation vector to the polar coordinates

$$\mathbf{p} = \begin{pmatrix} p_1 \\ p_2 \end{pmatrix} = \begin{pmatrix} \cos\varphi \\ \sin\varphi \end{pmatrix} \in \mathbb{S}^1,$$

one can add random perturbations of the form

$$\Delta\varphi = \xi\Phi,$$

to the polar angle φ of the unperturbed orientation vector $\mathbf{p}$. Similar to the random walk in $\mathbb{R}^d$ discussed in Section 4.3.1, Φ is the random variable uniformly distributed

on $[-\frac{1}{2}, \frac{1}{2}]$, and consequently, $\xi = \sqrt{24 D_r \Delta t}$. Hence, the perturbation vector $\Delta\mathbf{p}$ is evaluated as

$$\Delta\mathbf{p} = \begin{pmatrix} \Delta p_1 \\ \Delta p_2 \end{pmatrix} = \begin{pmatrix} \cos(\varphi + \Delta\varphi) - \cos\varphi \\ \sin(\varphi + \Delta\varphi) - \sin\varphi \end{pmatrix},$$

which preserves the initial length of the orientation vector $\mathbf{p}$ after the perturbation, i.e., $\mathbf{p} + \Delta\mathbf{p} \in \mathbb{S}^1$.

As discussed in Section 4.1.3, the reduced Cartesian form of the generator

$$Lf = \frac{\sigma^2}{2}\left(-\frac{\partial f}{\partial x_2} + \frac{\partial^2 f}{\partial x_1^2}\right),$$

leads to an alternative projection-based approach, by which first the random walk is calculated in the tangential vector and then it is projected onto $\mathbb{S}^1$. The tangential vector is orthogonal to the orientation vector $\mathbf{p}$ and is collinear to $\mathbf{p}^\perp = (-p_2, p_1)^T$. Therefore, the random perturbation in the tangential direction is given by

$$\Delta\mathbf{p}' = \begin{pmatrix} -p_2 \xi X \\ p_1 \xi X \end{pmatrix},$$

where X is uniformly distributed on $[-\frac{1}{2}, \frac{1}{2}]$ and $\xi = \sqrt{24 D_r \Delta t}$. The perturbed orientation vector $\mathbf{p} + \Delta\mathbf{p} \in \mathbb{S}^1$ is then obtained by performing the projection onto $\mathbb{S}^1$ as

$$\mathbf{p} + \Delta\mathbf{p} = \frac{\mathbf{p} + \Delta\mathbf{p}'}{\|\mathbf{p} + \Delta\mathbf{p}'\|},$$

which yields the perturbation vector

$$\Delta\mathbf{p} = \begin{pmatrix} \Delta p_1 \\ \Delta p_2 \end{pmatrix} = \frac{1}{\sqrt{1 + \xi^2 X^2}} \begin{pmatrix} p_1 - p_2 \xi X \\ p_2 + p_1 \xi X \end{pmatrix} - \begin{pmatrix} p_1 \\ p_2 \end{pmatrix}. \tag{4.43}$$

4.3.3 Random walk on $\mathbb{S}^2$

By analogy with the projection-based random walk on $\mathbb{S}^1$, we calculate a two-dimensional Cartesian random walk on the tangential plane perpendicular to the orientation vector $\mathbf{p}$ and then project it down onto the unit sphere $\mathbb{S}^2$. With this

aim, let us define an orthonormal basis for the tangential plane at $\mathbf{p} = (p_1, p_2, p_3)^T$ as

$$\hat{e}_1 = \frac{1}{\sqrt{p_1^2 + p_3^2}} \begin{pmatrix} p_3 \\ 0 \\ -p_1 \end{pmatrix}, \quad \hat{e}_2 = \frac{1}{\sqrt{p_1^2 + p_3^2}} \begin{pmatrix} p_1 p_2 \\ -(p_1^2 + p_3^2) \\ p_2 p_3 \end{pmatrix}. \tag{4.44}$$

Drawing an analogy with a one-dimensional case, random walks in the tangent plane can be generated by defining n vectors, each of which can uniformly attain an angle on $[0, 2\pi]$. To guarantee that random walks are performed in the tangent plane defined by (4.44), we introduce a unit vector in polar coordinates as

$$\mathbf{r} = \left(\hat{e}_1 \cos(\pi\Phi) + \hat{e}_2 \sin(\pi\Phi)\right),$$

by which the direction of each increment is determined, and Φ is a uniformly distributed random variable on $[-\frac{1}{2}, \frac{1}{2}]$.

Consequently, we introduce a random walk increment of the form

$$\Delta\mathbf{p}^* = \mathbf{r}\xi X, \tag{4.45}$$

where X is a random variable uniformly distributed on $[-\frac{1}{2}, \frac{1}{2}]$. Let us recall from Section 4.1 that the variance (covariance matrix) of the d-dimensional Brownian motion is $2D_r t\mathbf{I}$, under the assumption that the one-dimensional copies of the Brownian motion are independent. In what follows, we show that increment (4.45) leads to the covariance matrix with zero off-diagonal entries. Then we fit the matrix to its deterministic counterpart to calculate the scaling factor.

For the sake of simplicity, we restrict our attention to the North Pole, at which a reduced form of an increment of the walk is written as

$$\mathbf{r}' = (1, 0, 0)^T \cos(\pi\Phi)X + (0, -1, 0)^T \sin(\pi\Phi)X,$$

for which the covariance matrix is given by

$$\sigma^2 = \begin{pmatrix} \sigma_{x_1}^2 & Cov(x_1, x_2) & Cov(x_1, x_3) \\ Cov(x_2, x_1) & \sigma_{x_2}^2 & Cov(x_2, x_3) \\ Cov(x_3, x_1) & Cov(x_3, x_2) & \sigma_{x_3}^2 \end{pmatrix}. \tag{4.46}$$

The covariance of two random variables X and Y can be computed as follows:

$$Cov(X, Y) = \mathbb{E}[XY] - \mathbb{E}[X]\mathbb{E}[Y]. \tag{4.47}$$

Using formula (4.47), we calculate off-diagonal entries of matrix (4.46), e.g., $\sigma^2_{1,2}$, as

$$\begin{aligned}\sigma^2_{1,2} &= Cov(\cos(\pi\Phi)X, -\sin(\pi\Phi)X) \\ &= \mathbb{E}[-\cos(\pi\Phi)\sin(\pi\Phi)X^2] - \mathbb{E}[\cos(\pi\Phi)X]\mathbb{E}[-\sin(\pi\Phi)X].\end{aligned}$$

Since θ and X are independent, we have

$$\mathbb{E}[\cos(\pi\Phi)\sin(\pi\Phi)X^2] = \mathbb{E}[\cos(\pi\Phi)\sin(\pi\Phi)]\mathbb{E}[X^2].$$

Using equation (4.39) and performing further simplifications, we obtain $\sigma^2_{1,2} = 0$. The other off-diagonal entries are calculated similarly, which yields the same result.

Using the fact that $\mathbb{E}[X^2] = \frac{1}{12}$ and

$$\begin{aligned}\mathbb{E}[\cos^2(\pi\Phi)] &= \int_{\frac{-\pi}{2}}^{\frac{\pi}{2}} \cos^2(\pi\Phi)\frac{1}{\pi}du \\ &= \frac{1}{\pi}\int_{\frac{-\pi}{2}}^{\frac{\pi}{2}} \frac{1+\cos(2\pi\Phi)}{2}du \\ &= \frac{1}{\pi}\int_{\frac{-\pi}{2}}^{\frac{\pi}{2}} \frac{1}{2}du = \frac{1}{2},\end{aligned}$$

we calculate

$$\begin{aligned}\sigma^2_{1,1} &= \mathrm{Var}(\cos(\pi\Phi)X)) = \mathbb{E}[\cos^2(\pi\Phi)X^2] - \mathbb{E}[\cos(\pi\Phi)X]^2 \\ &= \mathbb{E}[\cos^2(\pi\Phi)]\mathbb{E}[X^2] - \mathbb{E}[\cos(\pi\Phi)]^2\mathbb{E}[X]^2 \\ &= \frac{1}{2}\frac{1}{12} = \frac{1}{24}.\end{aligned}$$

It can be easily shown that $\sigma^2_{2,2} = \sigma^2_{1,1}$.

Let us recall that the random walks are independent, i.e., the variance of the sum of increments equals the sum of each increment's variance. Hence, fitting covariance matrix (4.46) for all increments to its deterministic counterpart, the scaling factor is calculated as

$$\xi = \sqrt{48 D_r \Delta t}.$$

It should be noted that evaluating the scaling factor at the North Pole does not lose generality since all increments have the same variance.

Projecting onto $\mathbb{S}^2$, the perturbed orientation vector is obtained as

$$\mathbf{p} + \Delta\mathbf{p} = \frac{\mathbf{p} + \left(\hat{e}_1 \cos(\pi\Phi) + \hat{e}_2 \sin(\pi\Phi)\right) \xi X}{\|\mathbf{p} + \left(\hat{e}_1 \cos(\pi\Phi) + \hat{e}_2 \sin(\pi\Phi)\right) \xi X\|},$$

which yields the perturbation vector

$$\Delta\mathbf{p} = \begin{pmatrix} \Delta p_1 \\ \Delta p_2 \\ \Delta p_3 \end{pmatrix} = \frac{1}{\sqrt{1+\xi^2 X^2}} \begin{pmatrix} p_1 + \frac{p_3 \cos(\pi\Phi) + p_1 p_2 \sin(\pi\Phi))}{\sqrt{p_1^2+p_3^2}} \xi X \\ p_2 - \sin(\pi\Phi)\sqrt{p_1^2+p_3^2}\,\xi X \\ p_3 - \frac{p_1 \cos(\pi\Phi) - p_2 p_3 \sin(\pi\Phi))}{\sqrt{p_1^2+p_3^2}} \xi X \end{pmatrix} - \begin{pmatrix} p_1 \\ p_2 \\ p_3 \end{pmatrix}. \quad (4.48)$$

As an alternative to the computation of random walk in the tangent plane, one can generate the random walk in $\mathbb{R}^3$ followed by a projection onto $\mathbb{S}^2$. The perturbation vector calculated by (4.42) added to the orientation vector is projected onto $\mathbb{S}^2$ as follows:

$$\mathbf{p} + \Delta\mathbf{p} = \frac{\mathbf{p} + \Delta\tilde{\mathbf{p}}}{\|\mathbf{p} + \Delta\tilde{\mathbf{p}}\|}.$$

The perturbation vector can then be read off

$$\Delta\mathbf{p} = \begin{pmatrix} \Delta p_1 \\ \Delta p_2 \\ \Delta p_3 \end{pmatrix} = \frac{1}{\sqrt{\sum_{i=1}^{3}(p_i + \xi X_i)^2}} \begin{pmatrix} p_1 + \xi X_1 \\ p_2 + \xi X_2 \\ p_3 + \xi X_3 \end{pmatrix} - \begin{pmatrix} p_1 \\ p_2 \\ p_3 \end{pmatrix}. \quad (4.49)$$

This approach was used in [44, 45] for direct Monte Carlo simulations of fiber suspensions in turbulent channel flow. Following the steps of the proof of Donsker's theorem, one can show that the random walks generated with this approach converge to the Brownian motion on the sphere.

4.3.4 CDF-fitted spherical random walk on $\mathbb{S}^2$

In the previous section, the random walk on $\mathbb{S}^2$ was approximated using projection-based approaches. In this section, we generate a random walk directly on $\mathbb{S}^2$ using two different methods. Following Chen and Yu [43], the random walk is derived from an approximate solution of the spherical heat equation described in Section 4.2. Then we propose an exact random walk generated based on the analytical solution of the heat equation and the use of lookup tables.

Let us start with the formulation of the perturbation vector in the new reference frame proposed in Section 4.2. The unit vector $\hat{e}_3 = (0, 0, 1)^T$ of the rotated Cartesian coordinate system coincides with the unperturbed orientation vector $\mathbf{p}_0$. Denoting the perturbed orientation vector as $\mathbf{p}'$, the perturbation vector in the new reference frame $\Delta\hat{\mathbf{p}}$ is evaluated as

$$\Delta\hat{\mathbf{p}} = \mathbf{p}' - \hat{e}_3$$

which can be expanded to

$$\Delta\hat{\mathbf{p}} = \begin{pmatrix} \Delta\hat{p}_1 \\ \Delta\hat{p}_2 \\ \Delta\hat{p}_3 \end{pmatrix} = \begin{pmatrix} \sin(\hat{\Theta})\cos(\hat{\Phi}) \\ \sin(\hat{\Theta})\sin(\hat{\Phi}) \\ \cos(\hat{\Theta}) \end{pmatrix} - \begin{pmatrix} 0 \\ 0 \\ 1 \end{pmatrix},$$

where $\hat{\Phi}$ and $\hat{\Theta}$ are random variables that represent the angular perturbations in the new reference frame. Recalling the fact that the rotation of the fiber around $\hat{x}_3$ does not change its orientation, random variable $\hat{\Phi}$ can be calculated as follows:

$$\hat{\Phi} = 2\pi U, \tag{4.50}$$

where U is a random variable uniformly distributed on $[0, 1]$. The computation of $\hat{\Theta}$ is discussed later in this section.

The perturbation vector in the original coordinate system is then calculated using the following transformation:

$$\Delta\mathbf{p} = \begin{pmatrix} \Delta p_1 \\ \Delta p_2 \\ \Delta p_3 \end{pmatrix} = \begin{pmatrix} \sin\phi & \cos\theta\cos\phi & \sin\theta\cos\phi \\ -\cos\phi & \cos\theta\sin\phi & \sin\theta\sin\phi \\ 0 & -\sin\theta & \cos\theta \end{pmatrix} \begin{pmatrix} \Delta\hat{p}_1 \\ \Delta\hat{p}_2 \\ \Delta\hat{p}_3 \end{pmatrix}. \tag{4.51}$$

Equivalently, the perturbation vector can be evaluated in the Cartesian coordinate without performing the transformation. Recalling the coordinate transformation $\hat{x}_3 = \cos\hat{\theta}$ from Section 4.2, suppose that the random variable $\hat{X}_3$ represents the vertical coordinate of the Brownian motion on a sphere in the rotated frame at $t = \Delta t$. Its corresponding vector on the rotated frame is given by

$$\Delta\mathbf{p}_v = (\hat{X}_3 - 1)\mathbf{p}.$$

Since the rotation of a fiber along $\hat{x}_3$ does not change its orientation, the horizontal coordinate of the Brownian motion is nonunique and can be chosen arbitrarily.

Hence, we define a vector corresponding to the horizontal coordinate using the tangential basis vectors $\hat{e}_1$ and $\hat{e}_2$ defined by (4.44) as

$$\Delta\mathbf{p}_h = \zeta(\hat{e}_1 \cos(2\pi\Phi) + \hat{e}_2 \sin(2\pi\Phi)),$$

where Φ is a random variable uniformly distributed on $[-\frac{1}{2}, \frac{1}{2}]$. In the rotated frame we have $\|\mathbf{p}'\| = \sqrt{\hat{X}_3^2 + \zeta^2}$ which yields

$$\zeta = \sqrt{1 - \hat{X}_3^2}.$$

Therefore, the perturbation vector can be calculated as follows:

$$\Delta\mathbf{p} = \Delta\mathbf{p}_v + \Delta\mathbf{p}_h. \tag{4.52}$$

In order to calculate random variables $\hat{X}_3$ and $\hat{\Theta}$, let us use the so-called inverse transform sampling method, which employs the inverse of the cumulative distribution function (CDF) to generate random samples associated with a probability distribution function.

The CDF of random variable X is defined as the probability that X is less than or equal to a given value x, i.e.,

$$F(x) = \mathbb{P}[X \leq x]. \tag{4.53}$$

The continuous non-decreasing CDF of a probability distribution function f is defined as

$$F(x) = \int_{\infty}^{x} f(s)ds, \tag{4.54}$$

for $\infty \leq x \leq \infty$. The function $F : \mathbb{R} \to [0, 1]$ has the following properties:

$$\lim_{x\to\infty} F(x) = 1, \qquad \lim_{x\to-\infty} F(x) = 0.$$

Substituting the exact solution of the probability distribution function (4.30) into the spherical form of equation (4.54)

$$F(\theta, t) = 2\pi \int_0^{\theta} \hat{\psi}(\hat{\theta}, t) \sin\hat{\theta} d\hat{\theta}, \tag{4.55}$$

yields [43]

$$F(\theta, \tau) = 1 - \frac{1}{2} \sum_{n=0}^{\infty} C_n(\tau) P_n(\cos\theta), \tag{4.56}$$

where

$$C_n(\tau) = \exp[-(n-1)n\tau] - \exp[-(n+1)(n+2)\tau],\ \tau = D_r t.$$

Since using the rotated frame makes the exact CDF independent of the current time, i.e., $t = \Delta t$, we denote the function F_τ as a function of only one variable in space hereafter.

Let $F^{-1}(y)$, $y \in [0,1]$ denotes the inverse of the cumulative distribution function F. Assuming U as a random variable uniformly distributed on $[0,1]$, it can be shown that $X = F^{-1}(U)$ is distributed as F [87]. Note that it is feasible to define a generalized inverse function, even if the CDF is not invertible in a mathematical sense [88].

Then we can obtain a closed-form expression for $\hat{\Theta}$ as

$$\hat{\Theta} = F_\tau^{-1}(U). \tag{4.57}$$

Since inverting equation (4.56) requires extensive root-searching iterations, one can use approximation $\sin\hat{\theta} \approx \hat{\theta}$ with the assumption $\tau \ll 1$ discussed in Section 4.2. Substituting equation (4.36) into (4.55) yields

$$\tilde{F}_\tau(\theta) = 1 - \exp\left(-\frac{\theta^2}{4\tau}\right), \tag{4.58}$$

which can be easily inverted as follows:

$$\hat{\Theta} = \tilde{F}_\tau^{-1}(U) = \sqrt{-4\tau\ln(1-U)}. \tag{4.59}$$

Equivalently in the Cartesian coordinate, substituting (4.34) into

$$F(x_3) = \int_{-1}^{x} \hat{\psi}(\hat{x}_3, t)d\hat{x}_3, \tag{4.60}$$

yields

$$F_\tau(x) = \frac{x}{2} + \frac{1}{2}\sum_{n=1}^{\infty} \exp\left(-n(n+1)\tau\right)\left(P_{n+1}(x) - P_{n-1}(x)\right). \tag{4.61}$$

Using approximation $\sin\hat{\theta} \approx \hat{\theta}$ we have

$$\tilde{F}_\tau(x) = \exp\left(-\frac{\arccos^2 x}{4\tau}\right), \tag{4.62}$$

and consequently

$$\hat{X}_3 = \cos(\sqrt{-4\tau \ln(U)}). \tag{4.63}$$

As discussed in Section 4.2, the above approximation is based on the assumption $\tau \ll 1$. Chen and Yu [43] show that the CDF defined by (4.58) produces a poor approximation to (4.55) as τ increases and $\tilde{F}$ matches F only for $\tau < 1$.

If the CDF is not invertible, or is expensive to be inverted, methods like rejection sampling or the Metropolis–Hastings algorithm might offer more efficient approaches to generating random variables from a given probability distribution. However, using the rotated frame makes the exact CDF independent of the current time, i.e., $t = \Delta t$. As a consequence, in what follows, we provide an approach based on generating a lookup table, which is required to be constructed only once at the beginning of the simulation. This precalculation reduces the computational cost by replacing a runtime computation with an array indexing operation.

To that end, we calculate F at discrete points

$$F_j = F(\theta_j, \tau),$$

where $\theta_j = \pi \frac{j}{M}$ for $j = 0, \cdots, M$. Since $F_\tau : [0, \pi] \to [0, 1]$ is continuous and non-decreasing, using the intermediate value theorem, for any $U \in [0, 1]$ there exists an index j such $U \in [F_{j-1}, F_j]$. Decomposing $[0, \pi]$ into M equal size subintervals, we define the linear interpolant of F_{j-1} and F_j as

$$F_\tau^j(\theta) = F_{j-1}\frac{\theta_j - \theta}{\Delta\theta} + F_j\frac{\theta - \theta_{j-1}}{\Delta\theta}, \qquad \theta \in [\theta_{j-1}, \theta_j],$$

where $\Delta\theta = \frac{\pi}{M}$. Using equation (4.57), the inverse of the above linear function $(F_\tau^j)^{-1} : [F_{j-1}, F_j] \to [\theta_{j-1}, \theta_j]$ is used to calculate

$$\hat{\Theta} = (F_\tau^j)^{-1}(U) = \theta_{j-1}\frac{F_j - U}{F_j - F_{j-1}} + \theta_j\frac{U - F_{j-1}}{F_j - F_{j-1}}.$$

The CDF calculated at discrete points stored in an array associated with U can be located and retrieved efficiently using a search algorithm such as the binary search. An expression for X_3 can be obtained using a simple analogy to the approach presented above.

In the next chapter, we provide a comprehensive comparison between the different random walk approaches in terms of accuracy and computational cost.

Chapter 5

Numerical Results

The numerical studies presented in this chapter are categorized into three parts. In the first series of studies, we focus on the orientation behavior of fibers in homogeneous flows without considering their rheological influence on the carrier fluid, the so-called one-way coupled or decoupled study. Random walk methods discussed in the previous chapter are studied next, using the heat equation as a model problem. The results of this section are published in [46]. The methods are then employed to incorporate the effect of fiber-fiber interactions on the orientation distribution of fibers in a 3D simple shear flow. Finally, we study the rheological behavior of fiber suspension flow through a 3D axisymmetric contraction.

5.1 One-way coupled simulation

5.1.1 Homogeneous flows - without fiber interactions

In this section, we perform a numerical study of the Lagrangian approach to fiber orientation modeling for simple flows without taking the interaction of fibers into account. The components of the second-order orientation tensor are compared to the analytical solution of the Fokker-Planck equation

$$\mathbf{A}_{ex} = \psi_0 \left(\frac{\mathbf{C}.\mathbf{p}}{\|\mathbf{C}.\mathbf{p}\|} \right) \int_{\mathbb{S}^{d-1}} \frac{\mathbf{p} \otimes \mathbf{p}}{(\mathbf{B} : (\mathbf{p} \otimes \mathbf{p}))^{d/2}} d\mathbf{p}, \tag{5.1}$$

and those produced by Eulerian models provided in [14].

2D homogeneous flows

First, we perform numerical studies of 2D simple flows with the following velocity gradients:

- Planar elongation flow,

$$\nabla u = \begin{pmatrix} 0.01 & 0 \\ 0 & -0.01 \end{pmatrix}.$$

- Shear flow,

$$\nabla u = \begin{pmatrix} 0 & 0.01 \\ 0 & 0 \end{pmatrix}.$$

- Shearing and stretching flow,

$$\nabla u = \begin{pmatrix} 0.01 & 0.01 \\ 0 & -0.01 \end{pmatrix}.$$

We solve the Jeffery equation with $\lambda = \frac{99}{101}$ using the explicit Euler method with time step $\Delta t = 0.1$ for $0 \leq t \leq T = 150$. We first consider the isotropic initial condition, i.e.,

$$\psi_0(\mathbf{p}) = \frac{1}{2(d-1)\pi}, \qquad d = 2, 3. \tag{5.2}$$

This initial condition simplifies the exact solution to [16, 14]

$$\mathbf{A}_{ex} = \frac{1}{2(d-1)\pi} \int_{\mathbb{S}^{d-1}} \frac{\mathbf{p} \otimes \mathbf{p}}{(\mathbf{B} : (\mathbf{p} \otimes \mathbf{p}))^{d/2}} d\mathbf{p}, \tag{5.3}$$

and corresponds to the random orientation distribution of fibers.

Figure 5.1 illustrates the influence of the number of fibers on the accuracy of the Lagrangian approach to simulating the orientation dynamics of the elongation flow. Using more than a few thousand fibers makes it possible to achieve small further improvements in accuracy. However, the potential benefit is hardly worth the additional cost. In the rest of this section, we will use 2,000 sample fibers.

In Fig. 5.2, the Lagrangian approach is compared to Eulerian models that evolve the second-order orientation tensor using different closures for its fourth-order counterpart. The Lagrangian simulation for the planar elongation flow with 2,000 sample fibers performs better than all Eulerian models except for the natural closure, which yields the exact solution in the absence of fiber interactions under the assumption of isotropic initial conditions. A comparison with Fig. 5.1 reveals that the Lagrangian simulation with as few as 100 sample fibers is still more accurate than inexact Eulerian closure models. A similar comparison of the results for the shear flow and shear and stretching flow leads to the same observation (see Fig. 5.3 and 5.4).

For the non-isotropic initial conditions, however, the natural closure does not necessarily provide the exact solution. For instance, Kuzmin [14] showed that the piecewise-linear mixed closure produces more accurate results for elongation flow if $\mathbf{A}(0) = \text{diag}\{0.6571, 0.3429\}$. Using this initial condition, we perform the same comparative study for the abovementioned 2D flows.

The random orientation initialization of discrete fibers using a uniformly distributed random number generator leads to the isotropic initial condition. However, it is needed here to initialize the discrete fibers such that it yields the given second-order orientation tensor. For this reason, we reconstruct the probability distribution function from the given initial orientation tensor using the formula presented in [49, 11]. Then, we compute the cumulative distribution function from the reconstructed distribution function. Employing the inverse transform method discussed in Chapter 4, we initialize the orientation of individual fibers using a look-up table built from the inverse of the cumulative distribution function.

The reconstructed initial distribution function is also used to compute the exact solution using equation (5.1).

The results presented in Figures 5.5-5.7 indicate that the Lagrangian simulation with 2,000 particles outperforms the Eulerian models. Moreover, the Lagrangian approach is much less sensitive to the initial condition than the Eulerian models. Although the natural closure is not exact for this particular initial condition, it shall be noted that the model is exact if the isotropic state occurs at some time in its evolution history [14, 16].

It is worth mentioning that no particular closure here is found to be appropriate for all initial conditions and flows. This can be of great importance in the simulation of real-world problems in which the initial orientation of fibers is not necessarily isotropic. Also, a comparison with Fig. 5.1 reveals that the Lagrangian simulation with as few as 100 sample particles is still more accurate than inexact Eulerian closure models.

Whereas the Lagrangian simulation is more accurate than the Eulerian models under investigation, the cost of the former is higher as it requires solving the Jeffery equation for each individual fiber.

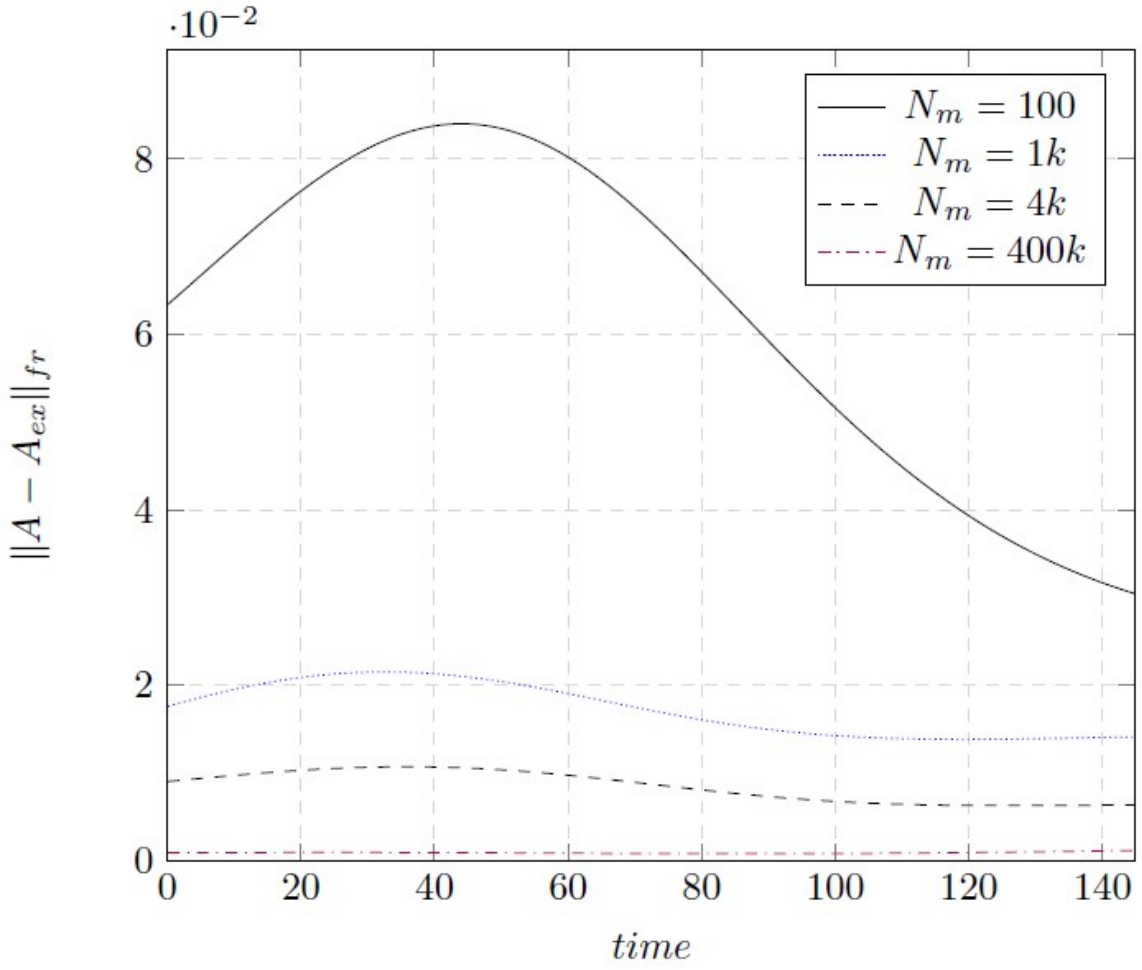

Figure 5.1: Influence of the number of Lagrangian fibers on the accuracy of the second order orientation tensor predictions for the 2D elongation flow.

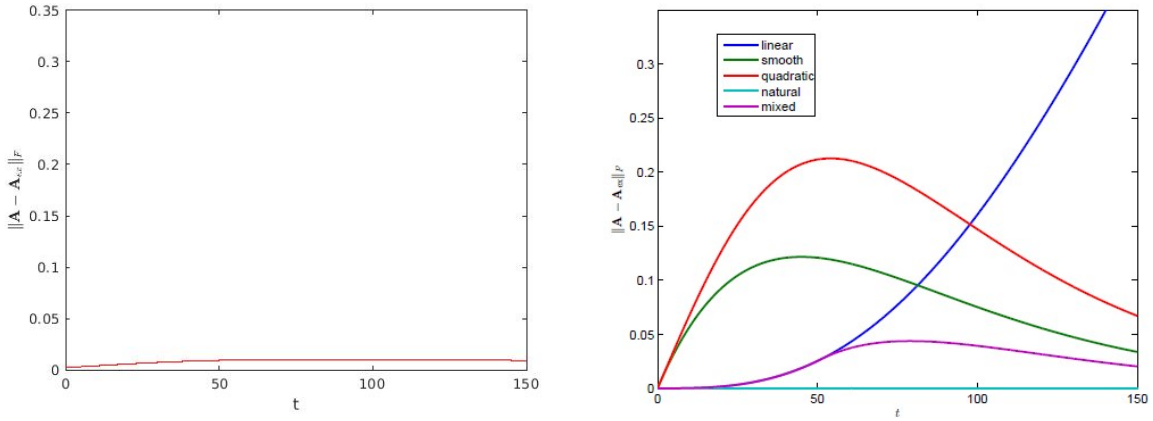

(a) (b)

Figure 5.2: Comparison between (a) Lagrangian simulation with 2,000 particles and (b) Eulerian approaches [14] for the 2D elongation flow with the isotropic initial condition, i.e., $\mathbf{A}(0) = \text{diag}\{0.5, 0.5\}$.

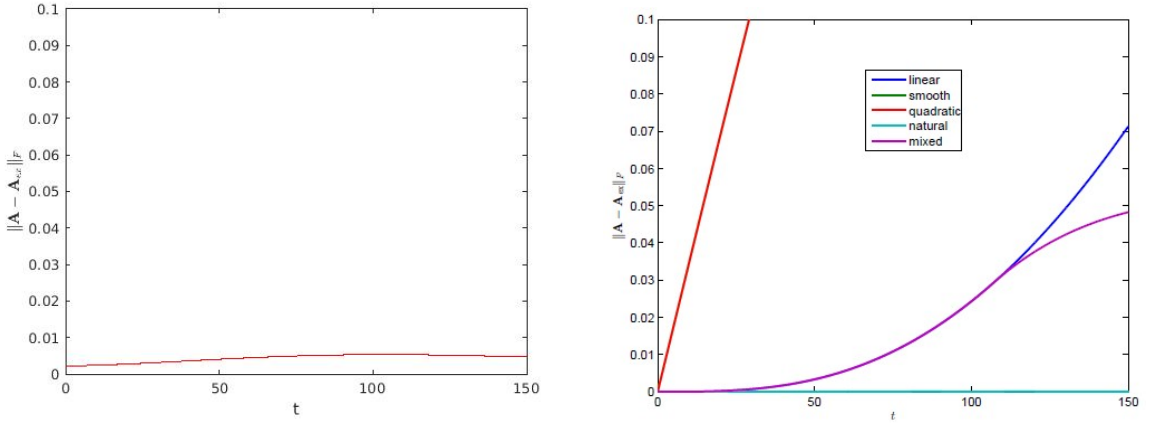

(a) (b)

Figure 5.3: Comparison between (a) Lagrangian simulation with 2,000 particles and (b) Eulerian approaches [14] for the 2D shear flow with the isotropic initial condition, i.e., $\mathbf{A}(0) = \text{diag}\{0.5, 0.5\}$.

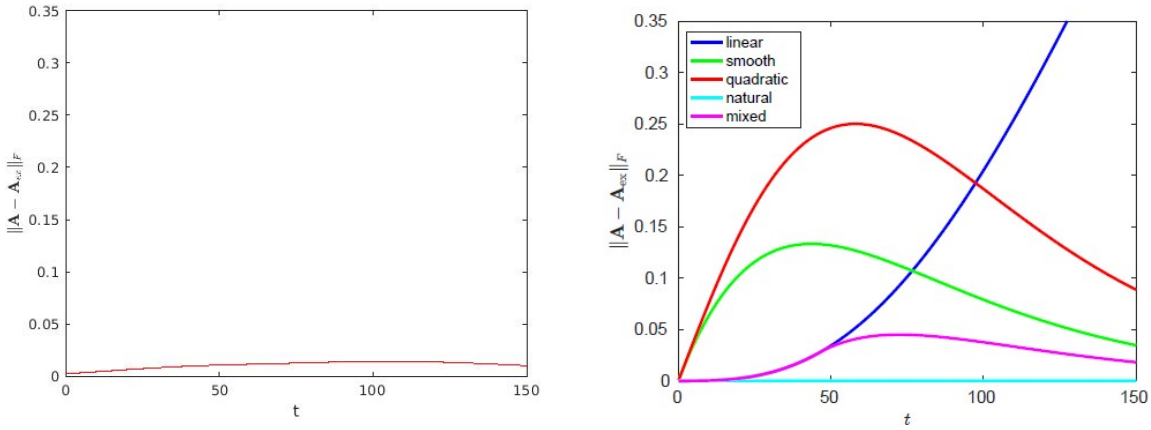

(a) (b)

Figure 5.4: Comparison between (a) Lagrangian simulation with 2,000 particles and (b) Eulerian approaches [14] for the 2D shear and stretching flow with the isotropic initial condition, i.e., $\mathbf{A}(0) = \text{diag}\{0.5, 0.5\}$.

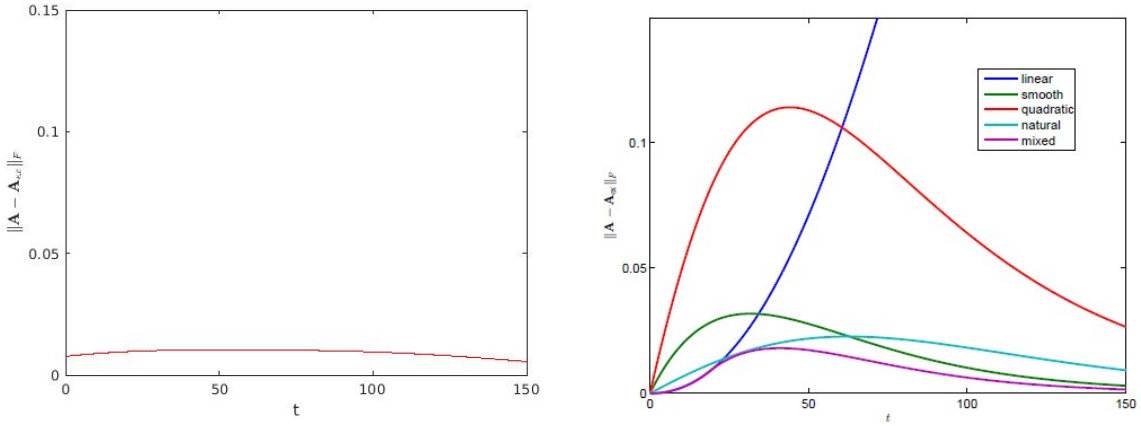

(a) (b)

Figure 5.5: Comparison between (a) Lagrangian simulation with 2,000 particles and (b) Eulerian approaches [14] for the 2D elongation flow, $\mathbf{A}(0) = \text{diag}\{0.6571, 0.3429\}$.

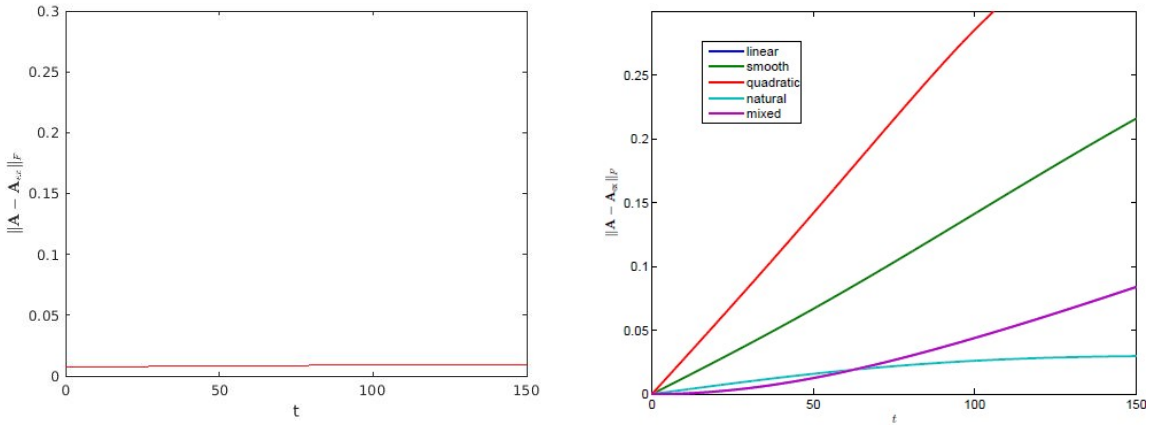

(a) (b)

Figure 5.6: Comparison between (a) Lagrangian simulation with 2,000 particles and (b) Eulerian approaches [14] for the 2D shear flow, $\mathbf{A}(0) = \text{diag}\{0.6571, 0.3429\}$.

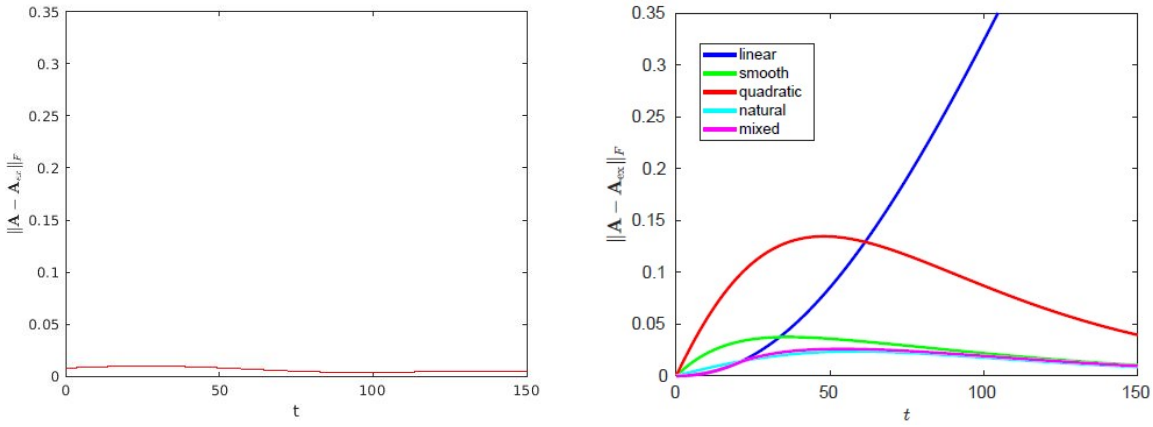

(a) (b)

Figure 5.7: Comparison between (a) Lagrangian simulation with 2,000 particles and (b) Eulerian approaches [14] for the 2D shear and stretching flow, $\mathbf{A}(0) = \text{diag}\{0.6571, 0.3429\}$.

3D homogeneous flows

For further comparison of the Lagrangian and Eulerian modeling frameworks, we study the following 3D simple flows:

- Uniaxial elongation flow,

$$\nabla u = \begin{pmatrix} 0.02 & 0.0 & 0.0 \\ 0.0 & -0.01 & 0.0 \\ 0.0 & 0.0 & -0.01 \end{pmatrix}.$$

- Biaxial elongation flow,

$$\nabla u = \begin{pmatrix} 0.01 & 0.0 & 0.0 \\ 0.0 & 0.01 & 0.0 \\ 0.0 & 0.0 & -0.02 \end{pmatrix}.$$

- Simple shear flow,

$$\nabla u = \begin{pmatrix} 0.0 & 0.05 & 0.0 \\ 0.0 & 0.0 & 0.0 \\ 0.0 & 0.0 & 0.0 \end{pmatrix}.$$

- Shearing and stretching flow,

$$\nabla u = \begin{pmatrix} -0.005 & 0.05 & 0.0 \\ 0.0 & -0.005 & 0.0 \\ 0.0 & 0.0 & 0.01 \end{pmatrix}.$$

With the isotropic initial condition, i.e., the random orientation distribution of fibers (see Fig. 5.8), the results presented in Fig. 5.9 to Fig. 5.12 exhibit that the Lagrangian version outperforms the majority of the Eulerian models also in applications to 3D simple flows. Some Eulerian models perform better in the 3D biaxial elongation flow, whereas the Lagrangian model produces a similar error curve insensitive to the flow type.

Further studies on a non-isotropic initial condition,
$\mathbf{A}(0) = \text{diag}\{0.25, 0.35, 0.4\}$, lead to the same observation, as shown in Figures 5.13-5.15.

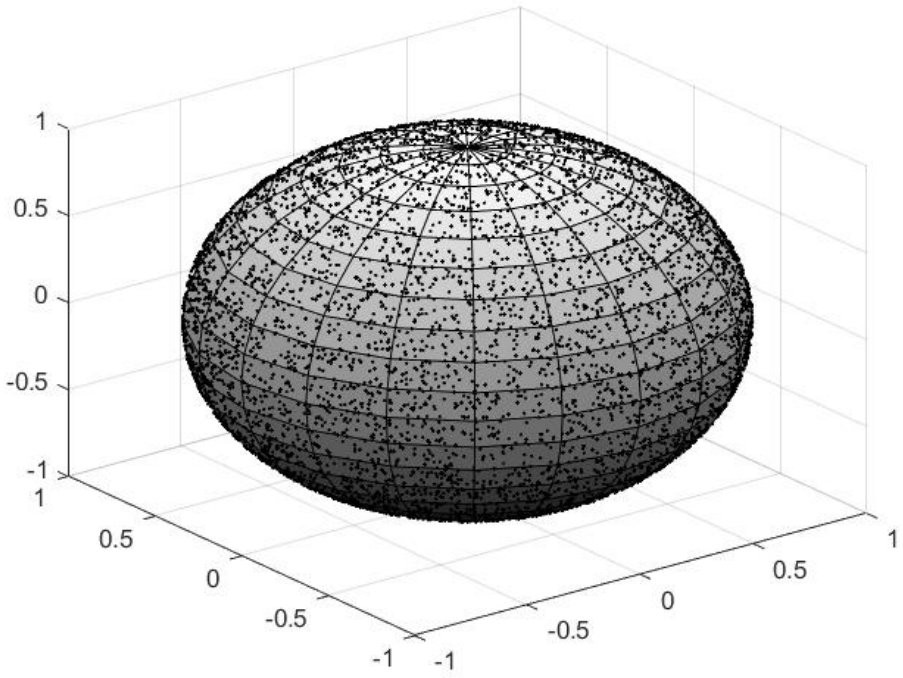

Figure 5.8: The uniform orientation distribution of sample fibers corresponding to the isotropic orientation state.

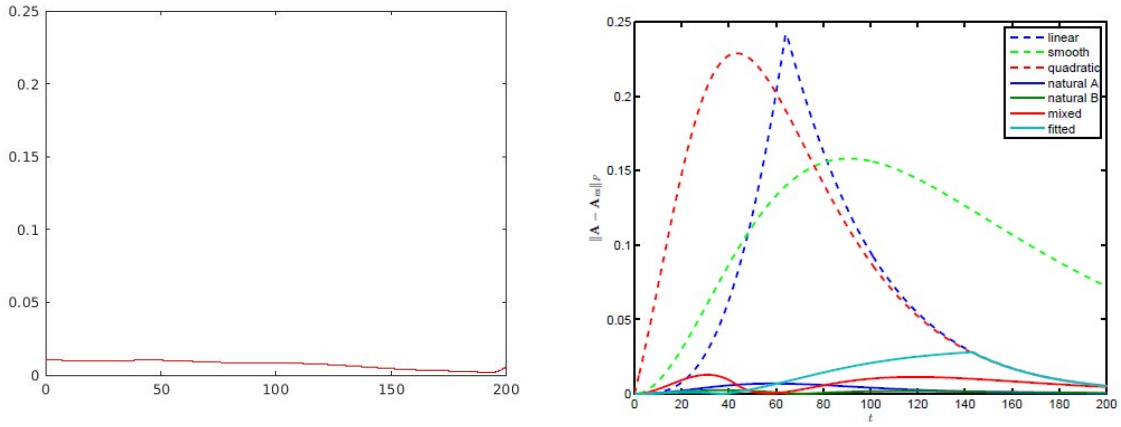

(a) (b)

Figure 5.9: Comparison between (a) Lagrangian simulation with 2,000 particles and (b) Eulerian approaches [14] for the 3D uniaxial elongation flow with the isotropic initial condition.

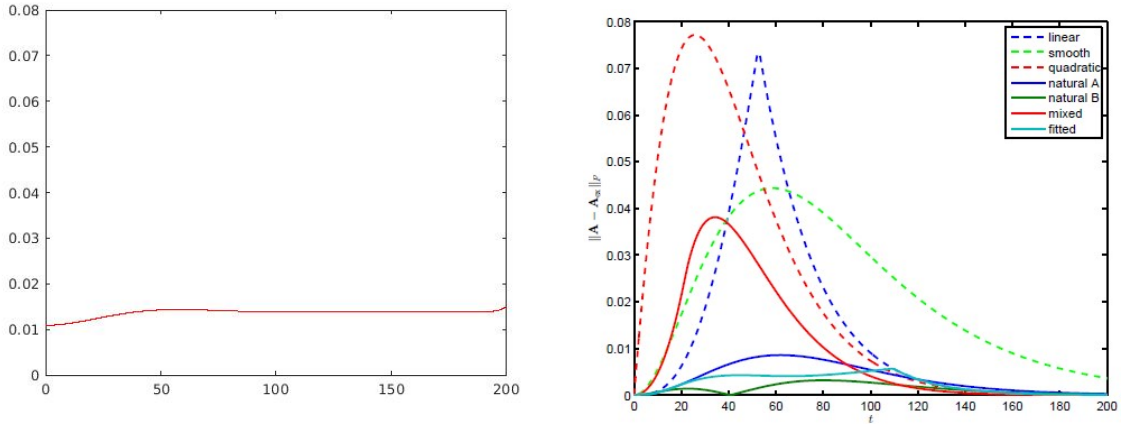

(a) (b)

Figure 5.10: Comparison between (a) Lagrangian simulation with 2,000 particles and (b) Eulerian approaches [14] for the 3D biaxial elongation flow with the isotropic initial condition.

Calculating the reference solution for 3D flows using arbitrary initial conditions can be cumbersome due to the formation of singularities. This explains the stagna-

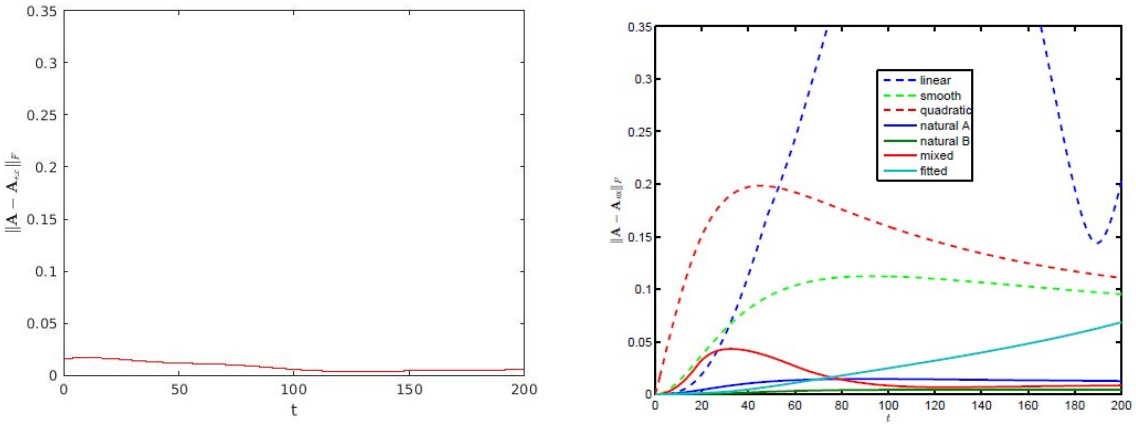

(a) (b)

Figure 5.11: Comparison between (a) Lagrangian simulation with 2,000 particles and (b) Eulerian approaches [14] for the 3D simple shear flow with the isotropic initial condition.

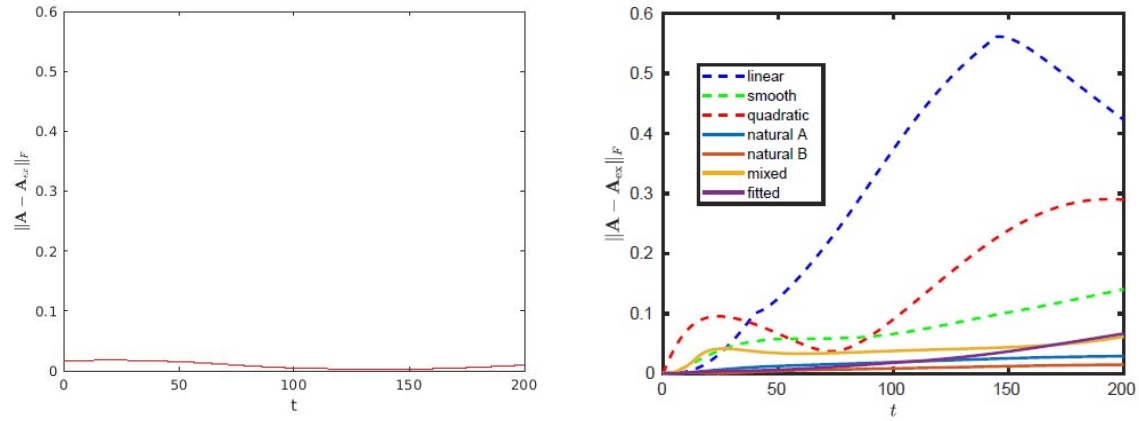

(a) (b)

Figure 5.12: Comparison between (a) Lagrangian simulation with 2,000 particles and (b) Eulerian approaches [14] for the 3D shearing and stretching flow with the isotropic initial condition.

tion in the error curve of Fig. 5.13, where the second-order orientation tensor of the

reference solution does not satisfy the unit trace condition. The formation of singularity was reported by Kuzmin [14] too, and consequently, no conclusions regarding the accuracy of the closures for the biaxial elongation flow could be drawn.

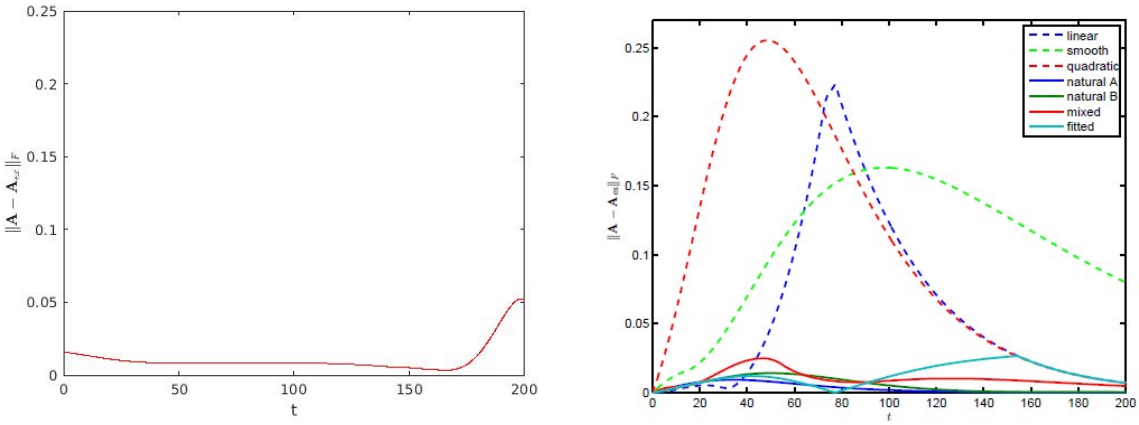

(a) (b)

Figure 5.13: Comparison between (a) Lagrangian simulation with 2,000 particles and (b) Eulerian approaches [14] for the 3D uniaxial elongation flow, $\mathbf{A}(0) = \text{diag}\{0.25, 0.35, 0.4\}$.

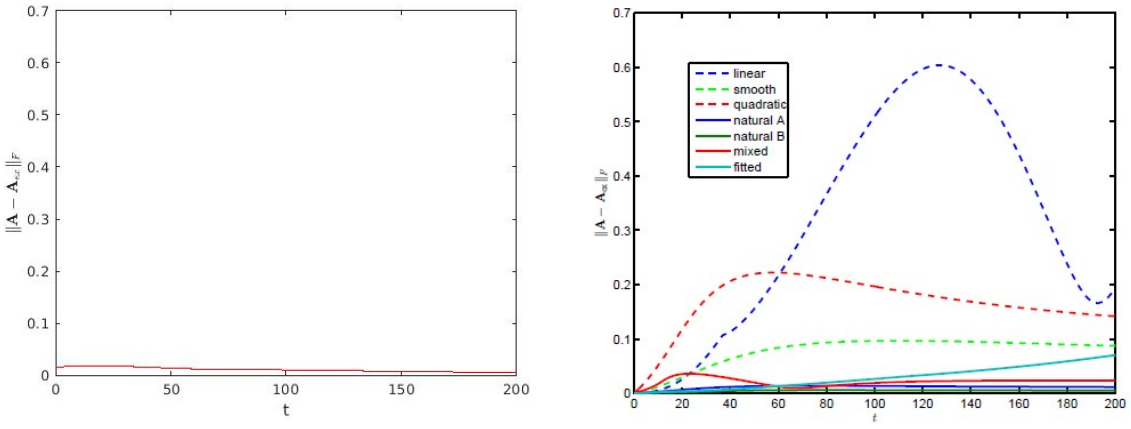

(a) (b)

Figure 5.14: Comparison between (a) Lagrangian simulation with 2,000 particles and (b) Eulerian approaches [14] for the 3D simple shear flow, $\mathbf{A}(0) = \text{diag}\{0.25, 0.35, 0.4\}$.

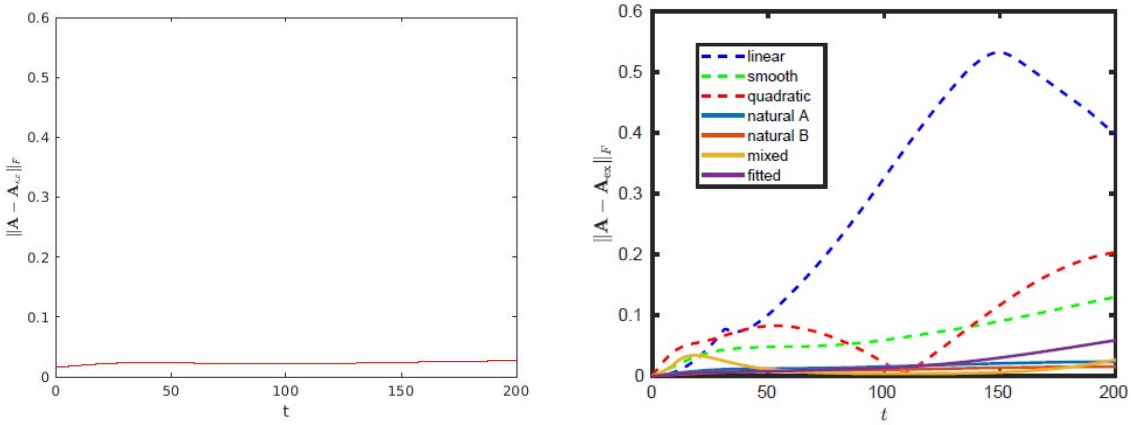

(a) (b)

Figure 5.15: Comparison between (a) Lagrangian simulation with 2,000 particles and (b) Eulerian approaches [14] for the 3D shearing and stretching flow, $\mathbf{A}(0) = \text{diag}\{0.25, 0.35, 0.4\}$.

5.1.2 Random walk

In this section, we compare and evaluate different random walk approaches discussed in Chapter 4. In the first part of this section, the numerical studies are performed for the three-dimensional spherical heat equation corresponding to formulation (4.23) (Chapter 4). The methods are then employed to study the effect of fiber-fiber interactions in a 3D homogeneous flow.

The following abbreviations are used for the methods under investigation:

- RW-CP: Cartesian random walk in $\mathbb{R}^3$ + projection onto $\mathbb{S}^2$ (Section 4.3.1, Chapter 4);
- RW-TP: Random walk on the tangential plane + projection onto $\mathbb{S}^2$ (Section 4.3.3, Chapter 4);
- RW-VH: Random walk in the vertical direction + random walk on the horizontal plane (Section 4.3.4, Chapter 4).

An additional letter X$\in$ {A,E} is used in abbreviations of the form RW-VH-X to distinguish between two different implementations:

- RW-VH-A: Approximate random walk method of Chen and Yu [43];
- RW-VH-E: Exact random walk using look-up tables for the CDF.

3D spherical heat equation

In the first set of numerical experiments, the initial condition is the δ distribution

$$\psi(\mathbf{p}(\theta,\varphi),0) = \delta(\mathbf{p}_0), \quad \mathbf{p}_0 \in \mathbb{S}^2,$$

which corresponds to

$$\mathbf{p}_0 = (0,0,1)^T.$$

The components of exact orientation tensors are given by

$$A_{ij}(t) = \int_0^{2\pi}\int_0^{\pi} p_i(\theta,\varphi)p_j(\theta,\varphi)\psi(\cos\theta,t)\sin\theta d\theta d\varphi, \tag{5.4}$$

$$A_{ijkl}(t) = \int_0^{2\pi}\int_0^{\pi} p_i(\theta,\varphi)p_j(\theta,\varphi)p_k(\theta,\varphi)p_l(\theta,\varphi)\psi(\cos\theta,t)\sin\theta\, d\theta d\varphi, \tag{5.5}$$

where $\psi(\hat{x}_3, t)$ is the azimuthal probability distribution defined by equation (4.34) (Chapter 4). The above integrals can be further simplified by making an appropriate change of variables. For example, A_{33} written in terms of $u = \cos\theta$ becomes

$$A_{33}(t) = 2\pi \int_{-1}^{1} u^2 g(u,t) du, \tag{5.6}$$

where

$$g(u,t) = \frac{1}{4\pi} \sum_{n=0}^{m} (2n+1) \exp[-n(n+1)Dt] P_n(u). \tag{5.7}$$

The number of terms in the truncated series approximations to $\psi(\theta, t)$ must be chosen sufficiently large to obtain the exact value of the given tensor component. Using Galerkin methods, orientation tensors of any order are uniquely defined by the first coefficients c_j of the truncated sum approximation

$$f_M(\mathbf{p}, t) = \sum_{j=1}^{M} c_j(t) \phi_j(\mathbf{p}), \tag{5.8}$$

by a linear combination of spherical harmonics ϕ_j. Hence, the exact values of A_{ij} and A_{ijkl} can be calculated using a small number m of terms in (5.7). More terms are generally required to calculate higher-order orientation tensors exactly.

Similar to the test case performed for a homogeneous flow, Fig. 5.16 illustrates the influence of the number of particles on the numerical results of one component of the second-order orientation tensor. The results obtained with other approaches exhibit similar dependence on the number of particles. In the remaining numerical experiments of this section, we perform random walks with 4,000 particles.

The approximations to A_{33} presented in Figures 5.17-5.18 indicate that all random walk methods under consideration produce similar results for small values of the scaled time step $\tau_t = D_r \Delta t$. Figure 5.19 demonstrates that our exact random walk (RW-VH-E) outperforms RW-CP and RW-TP as the time step increases and the accuracy of projection-based methods deteriorates.

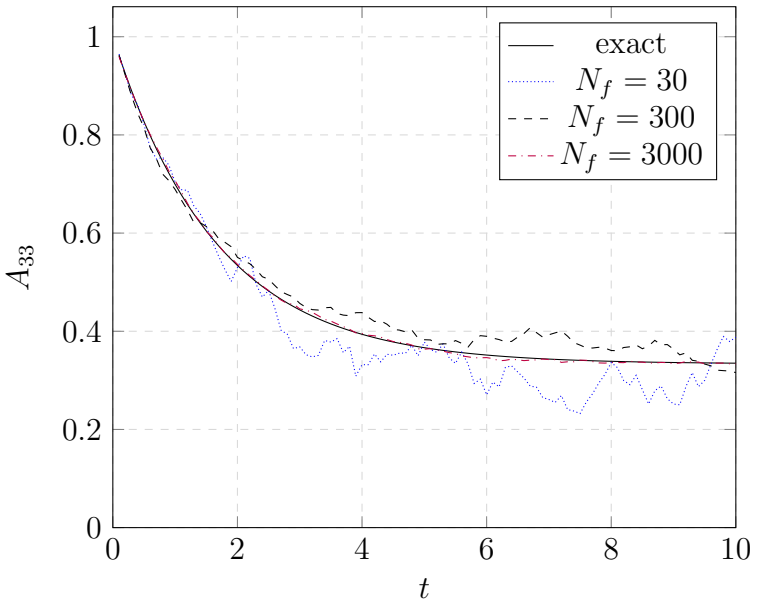

Figure 5.16: Dependence of the RW-CP results for A_{33} on the number of particles. Test problem: spherical heat equation with the initial condition given by the δ distribution.

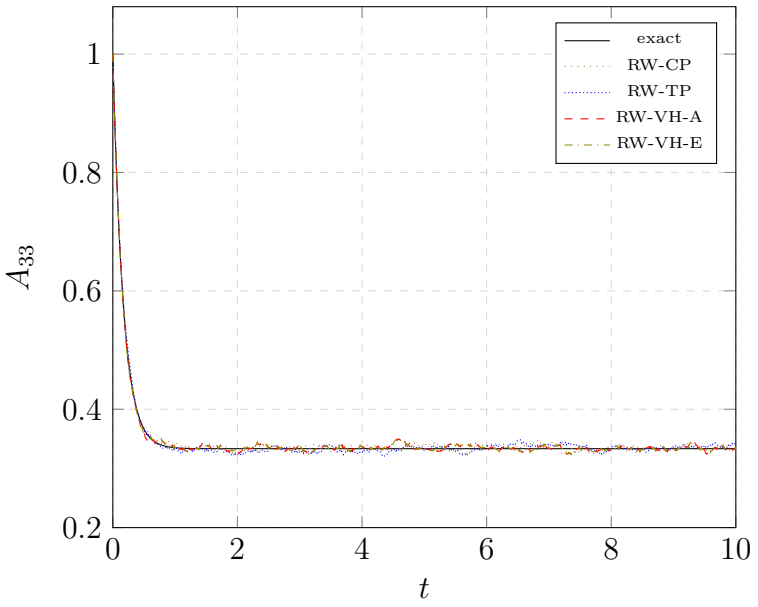

Figure 5.17: Evolution of A_{33} in random walks using $\tau_t = 0.01$ vs. the exact solution. Test problem: spherical heat equation with the initial condition given by the δ distribution.

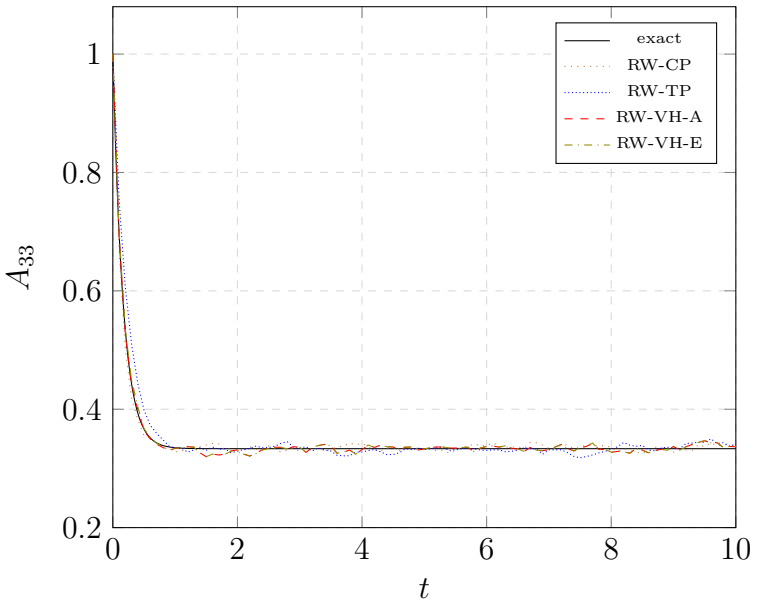

Figure 5.18: Evolution of A_{33} in random walks using $\tau_t = 0.1$ vs. the exact solution. Test problem: spherical heat equation with the initial condition given by the δ distribution.

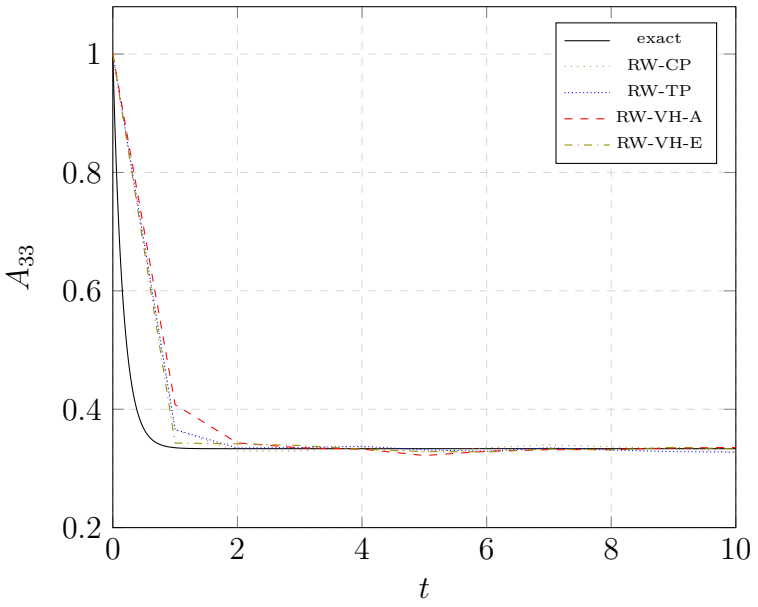

Figure 5.19: Evolution of A_{33} in random walks using $\tau_t = 1.0$ vs. the exact solution. Test problem: spherical heat equation with the initial condition given by the δ distribution.

For further comparison of different methods, we perform simulations for a randomly chosen initial state. In this set of experiments, the orientation angles of sample fibers at $t = 0$ are defined by

$$\Theta = \frac{\pi}{6}U, \qquad \Phi = 2\pi U,$$

where U is a random variable uniformly distributed on $[0, 1]$. This variable is generated using an identical seed for all methods. For each method, we present the results obtained with three different time steps. Since no exact solution is available for the case of random initial data, the results corresponding to $\tau_t = 0.01$ serve as reference solutions for each method. Indeed, this value of τ_t was found to produce sufficiently accurate approximations to the known exact solution of the first test problem (see Fig. 5.17).

The numerical approximations to the component A_{33} of the second-order orientation tensor are shown in Figures 5.20-5.23. Note that the RW-VH-E solution obtained with $\tau_t = 1$ is as accurate as the reference solution throughout the simulation run, whereas other methods produce significant errors after the first large time step. As in the first test, all methods yield accurate predictions for the constant value of A_{33} to which the reference solution converges as time goes. Clearly, individual components of low-order orientation tensors provide limited information about the probability distribution. As another quantity of interest, we consider the mean-squared angular displacement

$$\mathrm{MSD}(t) = \frac{1}{N_f}\sum_{m=1}^{N_f}(\theta_m(t) - \theta_m(0))^2,$$

where N_f is the number of samples. The evolution of MSD for the two versions of RW-VH is shown in Figures 5.24-5.25. The RW-VH-A method produces a significant overshoot after the first time step corresponding to $\tau_t = 1$. The random walk approach using the look-up table (RW-VH-E) is seen to produce excellent results for all three values of τ_t already at early stages. We conclude that it is better suited for simulating dynamic changes of orientation states with large time steps than any other method considered in this study.

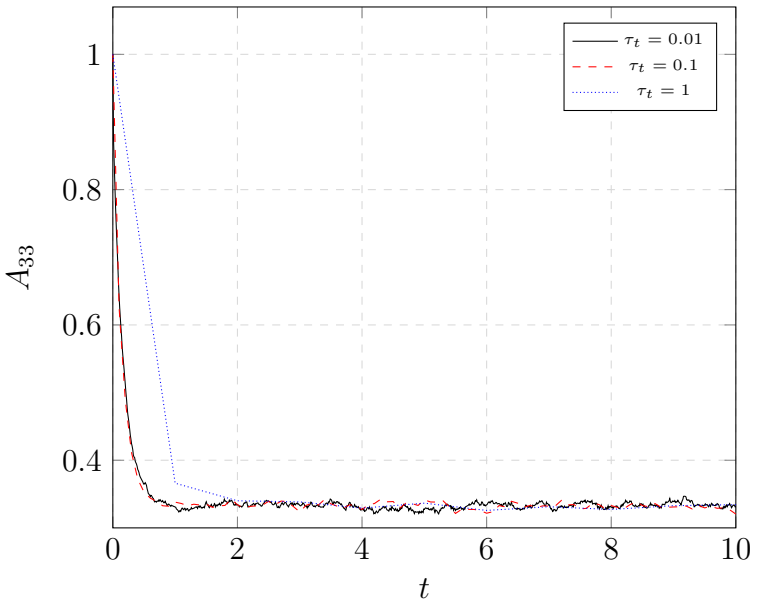

Figure 5.20: Evolution of A_{33} in random walks using RW-CP. Test problem: spherical heat equation with the random initial condition.

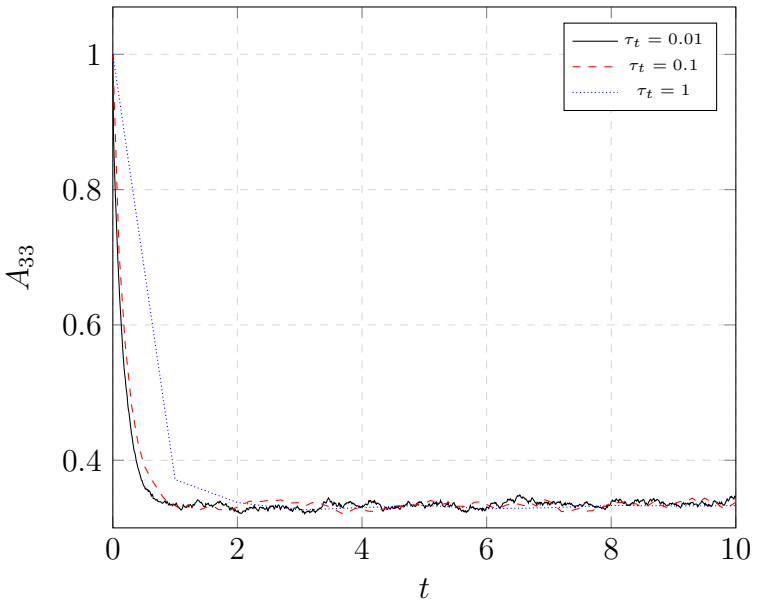

Figure 5.21: Evolution of A_{33} in random walks using RW-TP. Test problem: spherical heat equation with the random initial condition.

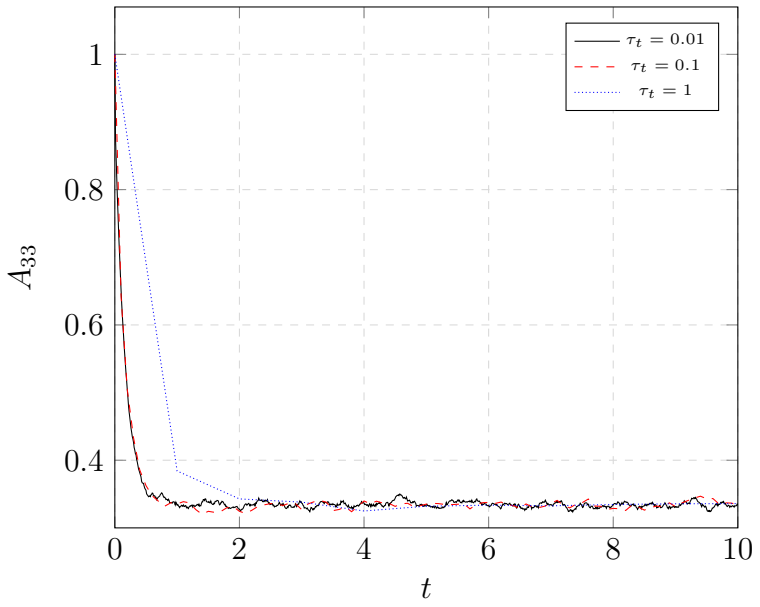

Figure 5.22: Evolution of A_{33} in random walks using RW-VH-A. Test problem: spherical heat equation with the random initial condition.

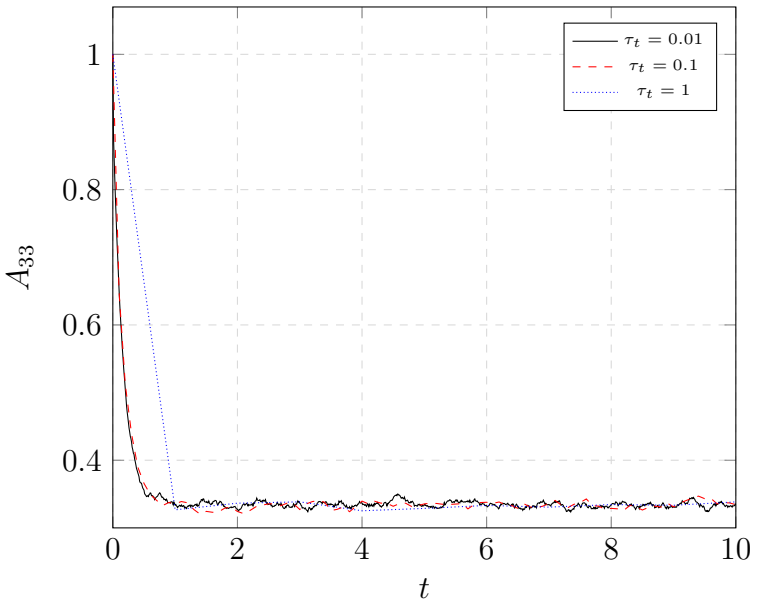

Figure 5.23: Evolution of A_{33} in random walks using RW-VH-E. Test problem: spherical heat equation with the random initial condition.

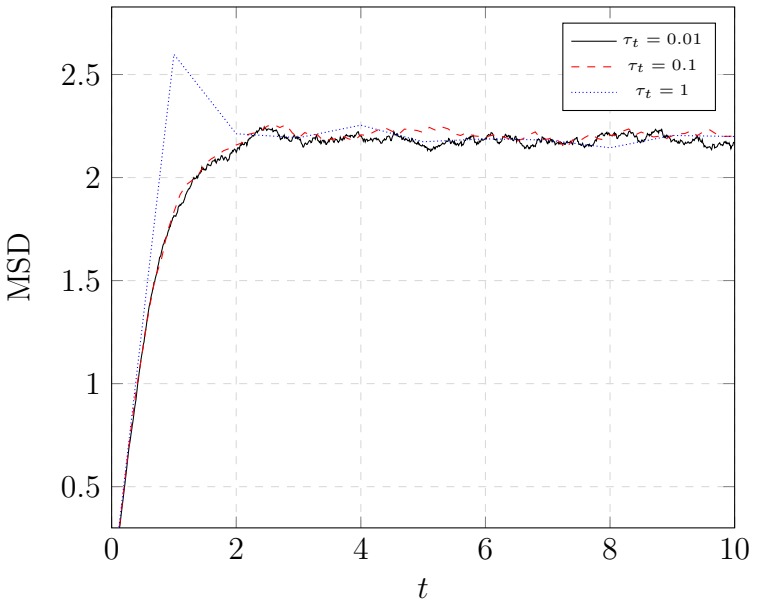

Figure 5.24: Evolution of MSD in random walks using RW-VH-A. Test problem: spherical heat equation with the random initial condition.

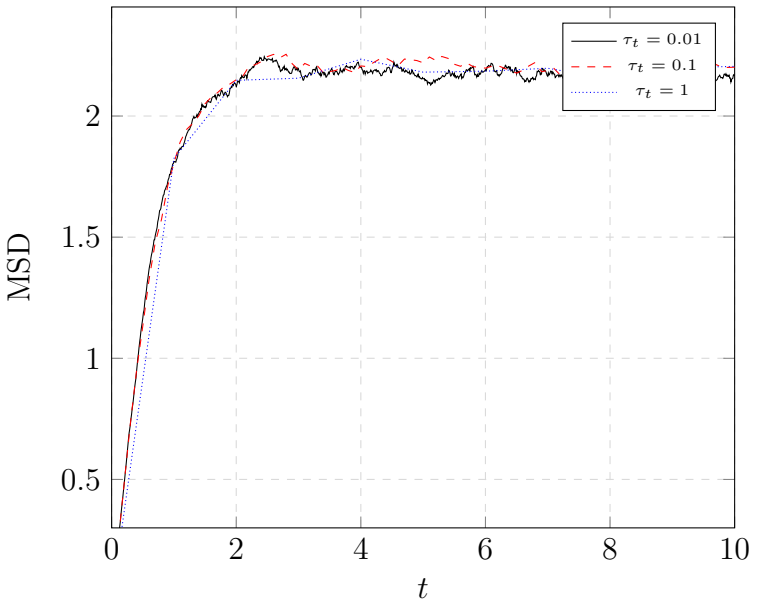

Figure 5.25: Evolution of MSD in random walks using RW-VH-E. Test problem: spherical heat equation with the random initial condition.

3D homogeneous flow - with fiber interactions

Using random walk methods discussed in the previous section, we perform a numerical study of a 3D simple shear flow in which fiber interactions are taken into account. Due to the lack of an exact solution for $D_r \neq 0$, we use the reference solution computed in the work of Cintra and Tucker [48] by solving the Fokker-Planck equation for the probability distribution function using a finite difference code. The velocity gradient of the 3D simple shear flow is defined as

$$\nabla u = \begin{pmatrix} 0.0 & g & 0.0 \\ 0.0 & 0.0 & 0.0 \\ 0.0 & 0.0 & 0.0 \end{pmatrix},$$

where $g = 0.1$. The Jeffery equation with $\lambda = 1$ is solved using the explicit Euler method with time step $\Delta t = 0.1$ for $0 \leq t^* \leq 20$, where $t^* = tg$ is a dimensionless time parameter. The formulation presented in Section 4.3 (Chapter 4) is employed to model the rotary diffusion term using the random walk methods and includes the influence of fiber-fiber interactions in the Lagrangian framework.

In Fig. 5.26, the Lagrangian approach equipped with the aforementioned random walk methods is compared with different Eulerian approaches [48] for $C_I = 0.01$. The DFC curve is the reference solution. The other curves represent different closure models, including natural (NAT), Hinch and Leal's second composite (HL2), orthotropic fitted (ORF), and hybrid closures (HYB). While the natural closure provides the exact description of orientation dynamics in the absence of fiber interactions, the orthotropic closure yields the best predictions among the Eulerian approaches under investigation when rotary diffusion comes into play. The results of the Lagrangian simulation exhibit a very good agreement with the reference solution and are more accurate than numerical solutions obtained using the Eulerian models. As shown in the previous section, the random walk methods behave similarly for small values of the scaled time step $\tau_t = D_r \Delta t$.

By construction, the parameters of fitted closures depend on the value of the interaction coefficient C_I. Therefore, a change in the value of C_I may require the use of a different closure [48]. For example, the orthotropic fitted closure denoted by ORL in Fig. 5.27 was derived using polynomial fitting to numerical solutions of the Fokker-Planck equation with $C_I = 0.001$. The Lagrangian approach does not require closure approximations for the fourth-order tensor and the simulation results agree well with the reference solution in the whole range of the interaction coefficients.

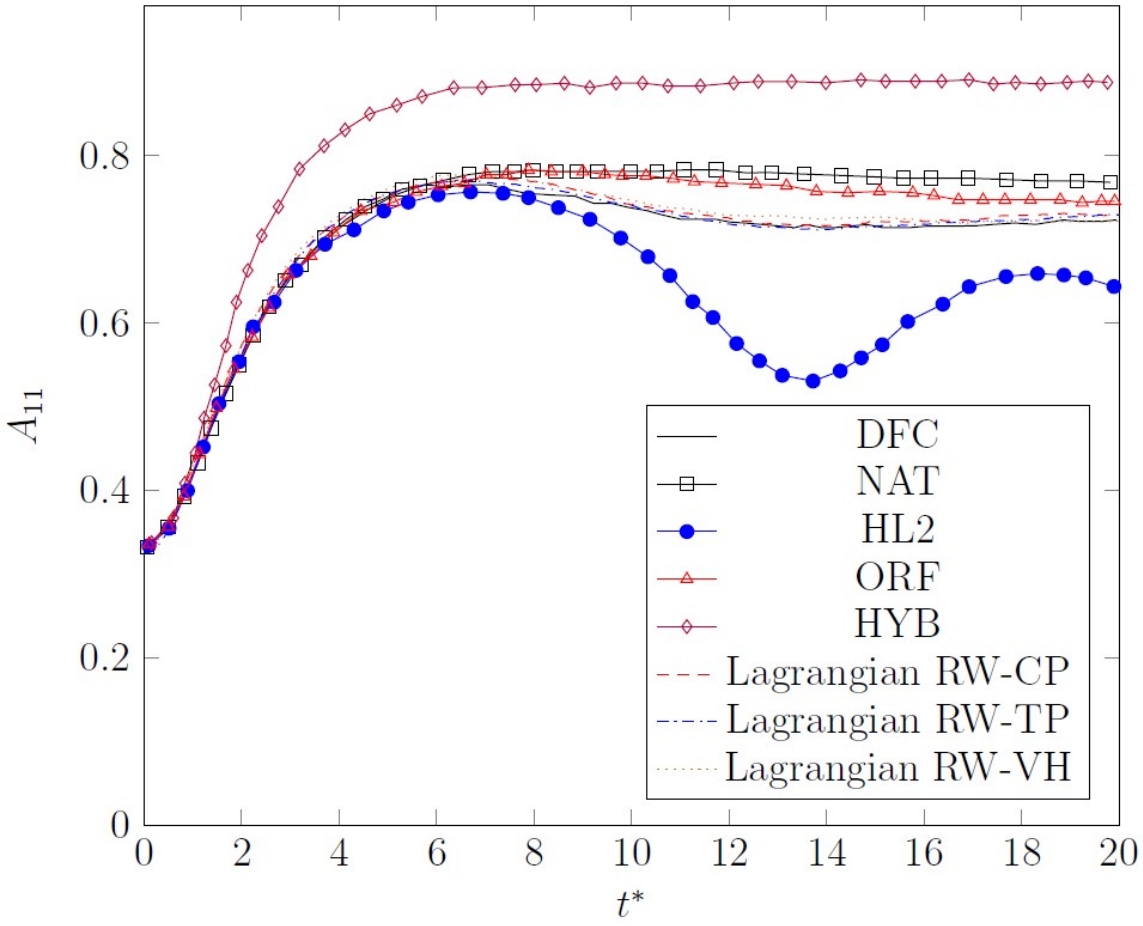

Figure 5.26: Comparison between the Eulerian approaches [48] and the Lagrangian simulations using different random walk methods with 4,000 fibers, the isotropic initial condition, $C_I = 0.01$.

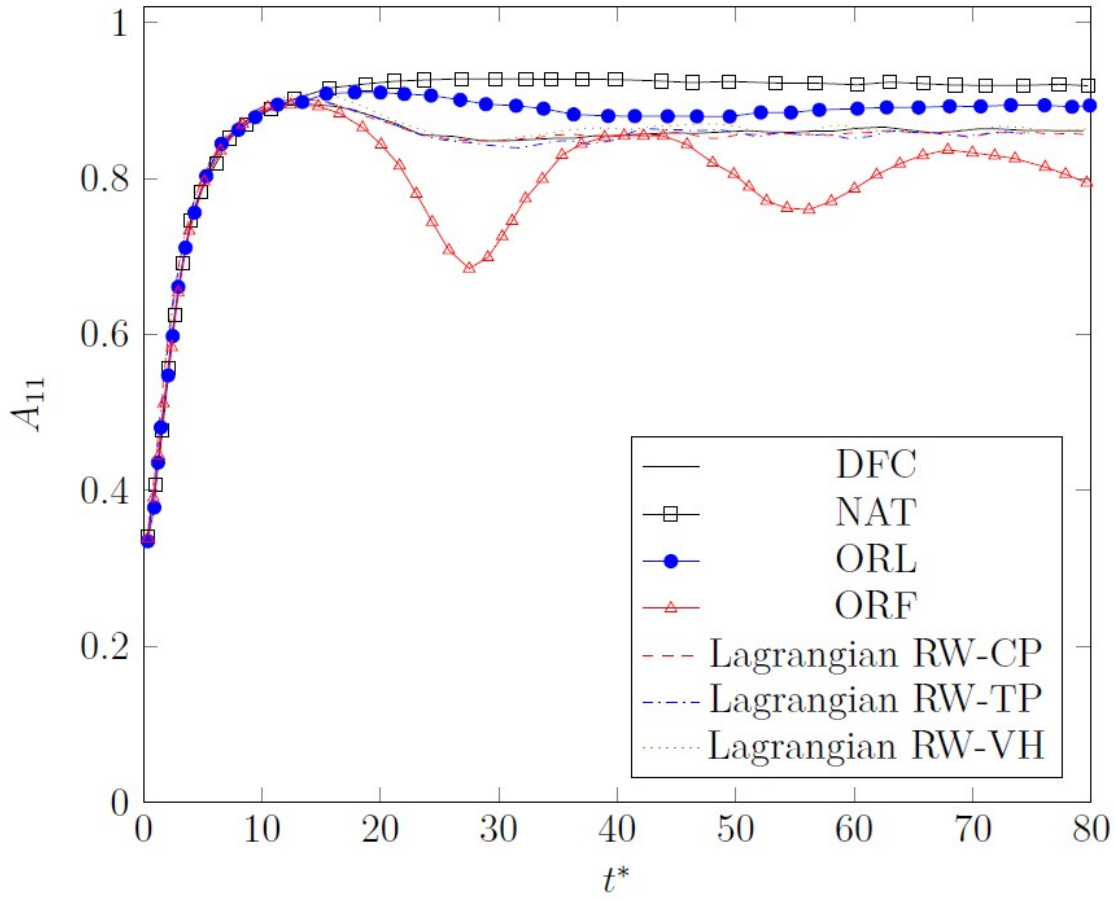

Figure 5.27: Comparison between the Eulerian approaches [48] and the Lagrangian simulations using different random walk methods with 4,000 fibers, the isotropic initial condition, $C_I = 0.001$.

5.2 Two-way coupled simulation

In the previous sections, we performed numerical studies of the Lagrangian and Eulerian approaches to fiber orientation modeling in one-way coupled simulations. In this section, we perform numerical studies of the two-way coupled system in which the influence of fiber-induced stresses on the carrier fluid is taken into consideration.

5.2.1 Channel flow

Recalling the discussion in Section 2.2.2 (Chapter 2), it was shown that an isotropic orientation state of a fiber suspension leads to a Newtonian flow with a higher viscosity. The effective viscosity can then be analytically evaluated because we have an exact evaluation of the fourth-order orientation tensor using the linear closure under the assumption of the isotropic states [14]. We use this finding to validate our two-way coupled solver in a simple geometry and flow pattern.

For this purpose, we choose a laminar flow in a simple channel with parallel sides. A Quasi-2D approach is used, i.e., the thickness of the computational domain is set to a small value. This method requires zero flow in the third direction and the symmetry boundary condition on both the front and back faces. For a laminar incompressible flow with constant properties, the velocity distribution in the channel with a height of $2h$ can be analytically evaluated as [89]

$$\mathbf{u}(y) = -\frac{1}{2}\frac{h^2}{\mu}\frac{dP}{dx}\left[1 - \left(\frac{y}{h}\right)^2\right]\mathbf{e}_x, \tag{5.9}$$

where $\mathbf{e}_x = (1, 0, 0)^\intercal$, and $\frac{dP}{dx}$ is assumed to be constant as the source of momentum of the flow. The maximum velocity occurred at the center-line reads

$$\mathbf{u}_m(y = h) = -\frac{1}{2}\frac{h^2}{\mu}\frac{dP}{dx}\mathbf{e}_x. \tag{5.10}$$

We first study the numerical results of the flow without fibers. The velocity distribution of the simulation with $\mu = 0.01$ and $\frac{dP}{dx} = -0.004$ is shown in Fig. 5.28. The detailed plot of $\mathbf{u}(y)$ at $x = 2.5$ illustrates that the results computed with our one-way coupled solver have a perfect agreement with the analytical solution.

Following the discussion from Section 2.2.2 (Chapter 2), we calculate $\frac{\mu_{eff}}{\mu} = 4.584$ by setting $r = 150$ and $\phi = 0.01$ using equation

$$\tau = 2\mu_{eff}D = 2\Big(\mu + \mu_0 + \frac{1}{15}\mu_2 + \frac{2}{3}\mu_3\Big)D, \tag{5.11}$$

and the formulas (2.37) (Chapter 2). It follows that the reference maximum velocity magnitude of the suspension flow with the above parameter has a value of 0.04363, which is still in the laminar flow regime.

In the first test case, we perform a two-way coupled simulation using the explicit approach discussed in Section 3.2.4 (Chapter 3). In order to approximate the orientation tensors, the fibers located only within an average distance of radius length of two element edges are selected. The fibers are initialized in the domain such that it guarantees the existence of an average of 6000 particles around each computational node in the areas under study. The fiber-induced stress tensor is computed using the formulas proposed by Brenner (2.36) (Chapter 2).

Due to the employed statistical approach, the calculated velocity is expected to be oscillatory even after a large number of simulation steps. Therefore, the simulation is performed until the amplitude of the oscillation as well as the relative change of the computed velocity average, reaches below 0.01%. As shown in Fig. 5.29, our two-way coupled solver has a very good agreement with the reference solution by calculating the maximum velocity magnitude of 0.04364.

The next two-way coupled simulation is performed based on the implicit approach presented in Section 3.2.4 (Chapter 3) using the simplified formula (3.31) (Chapter 3). Figure 5.30 demonstrates that the implicit approach produces 0.6% relative error by calculating the maximum velocity magnitude of 0.04391. This deviation is expected, as the reference solution is calculated using Brenner's constitutive equation.

Hence, we perform a further simulation using the explicit approach with the simplified formula exploited in the implicit approach. The computed velocity magnitude of 0.04392 indicates that the neglected terms in the simplified formula are the source of the measured error. The influence of the fiber's aspect ratio on the coefficients of Brenner's stress formula can be seen in Fig. 5.31. Coefficients of the other stress formulas have a similar relation to the aspect ratio.

In order to see the influence of the volume fraction and aspect ratio on the accuracy of the stress formulas, we perform a similar test case by setting $r = 276$ and $\phi = 0.045\%$, the parameters by which the numerical simulation of fiber suspension flow in a 3D axisymmetric contraction geometry is studied in the next section. Whereas our first experiment with the simplified formula produces around 0.6% relative error, the abovementioned higher aspect ratio and lower volume fraction lead to around 0.07% relative error.

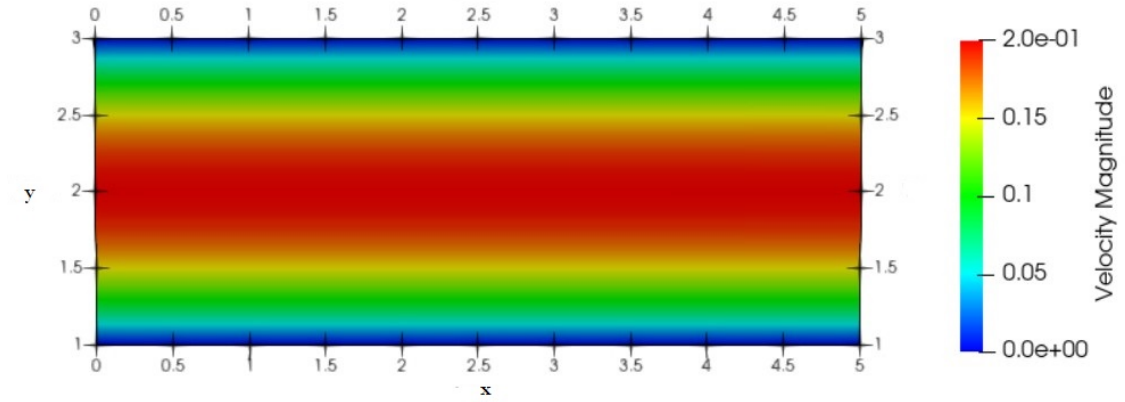

(a)

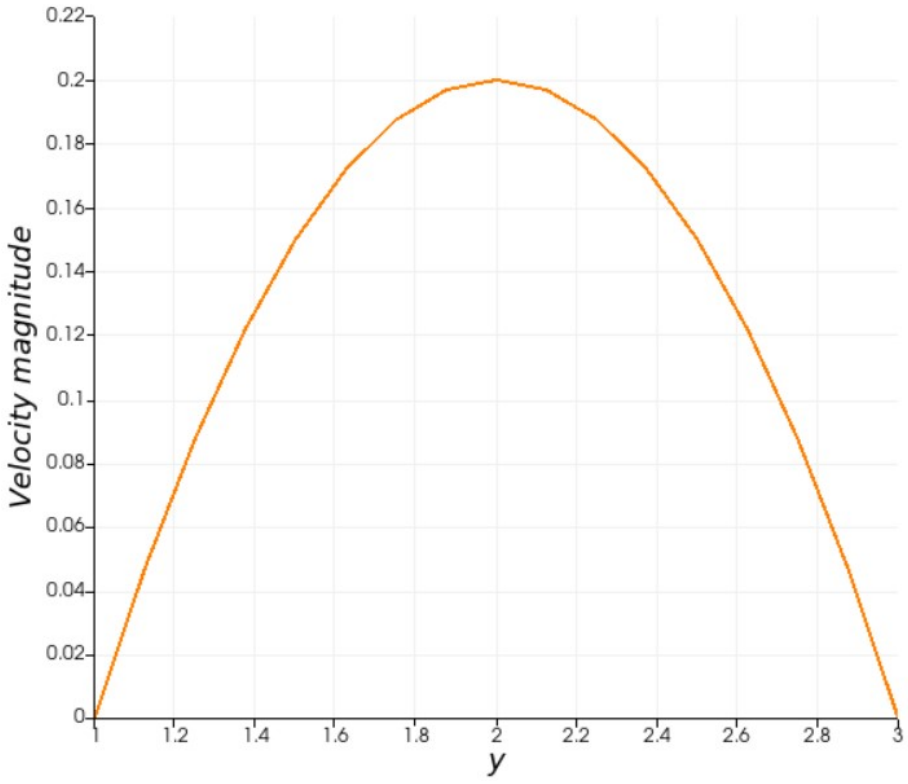

(b)

Figure 5.28: (a) The distribution of the velocity magnitude computed with the decoupled solver. (b) The magnitude of the velocity field at x=2.5.

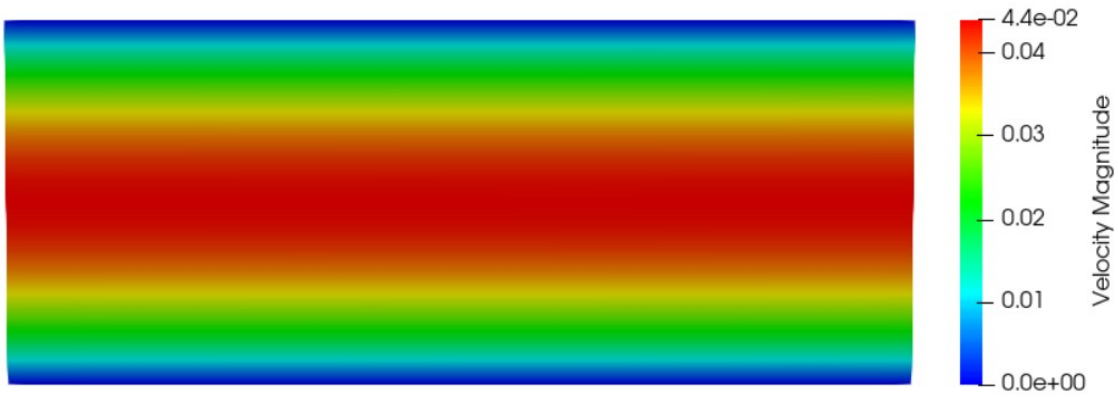

(a)

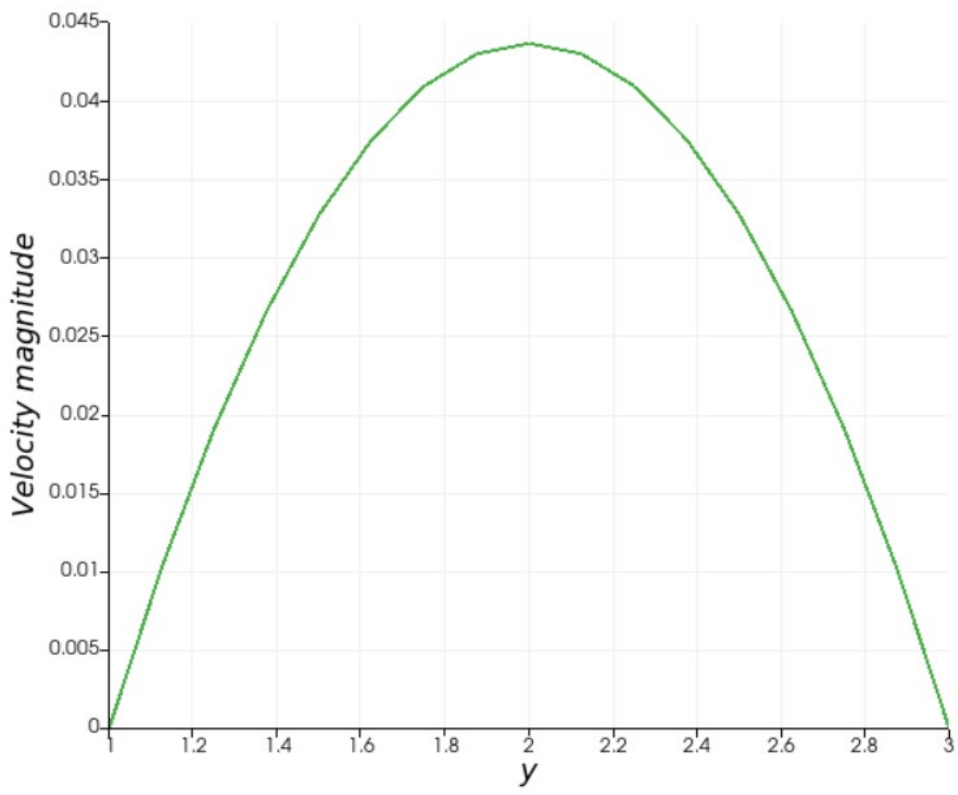

(b)

Figure 5.29: (a) The distribution of the velocity magnitude computed with the two-way coupled simulation using the explicit approach with Brenner's constitutive equation.(b) The magnitude of the velocity field at x=2.5.

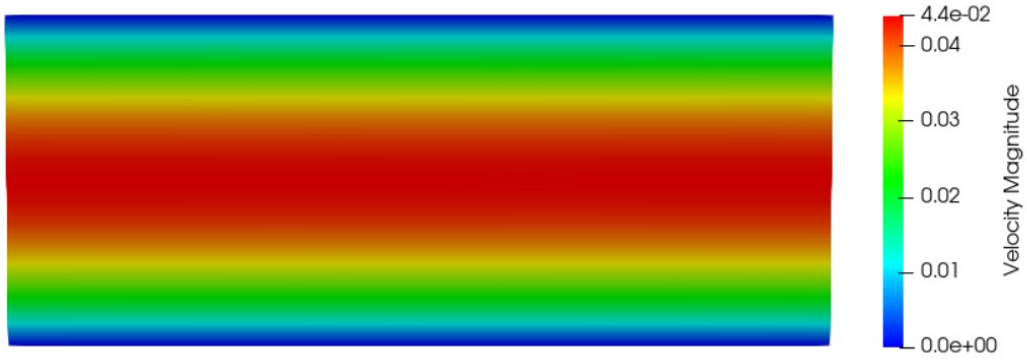

(a)

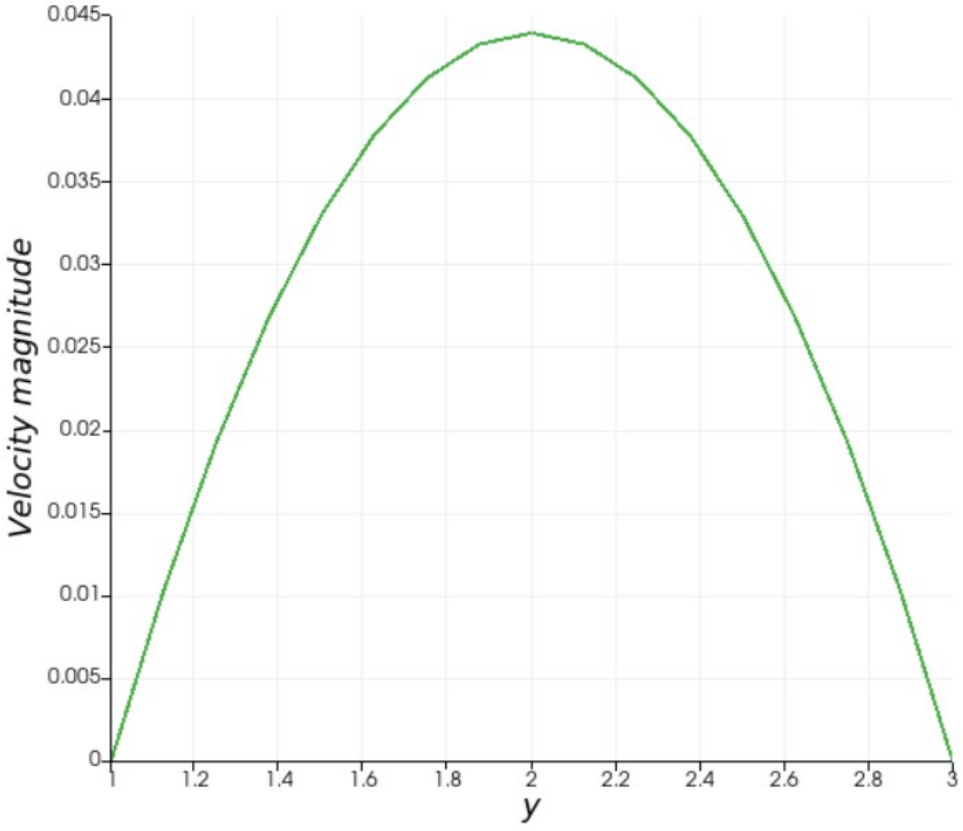

(b)

Figure 5.30: (a) The distribution of the velocity magnitude computed with the two-way coupled simulation using the implicit approach with the simplified stress formula. (b) The magnitude of the velocity field at x=2.5.

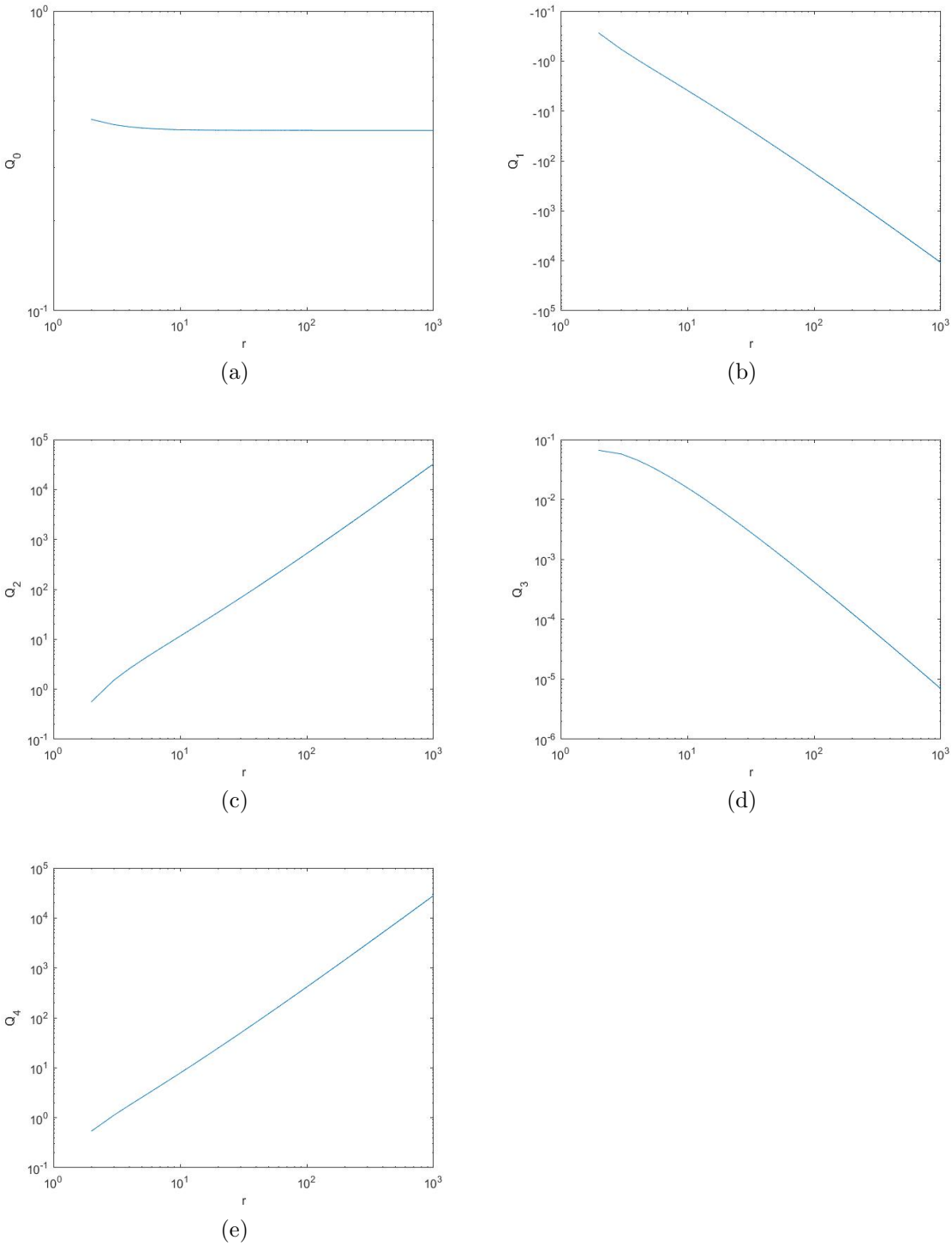

Figure 5.31: The influence of the fiber's aspect ratio on the coefficients of Brenner's constitutive equation.

5.2.2 3D axisymmetric contraction

In this section, we turn to the numerical simulation of fiber suspension flow in a 3D axisymmetric 4.5 : 1 contraction geometry, for which experimental data and numerical results using the Eulerian approach are presented in [10, 12, 15]. As shown in Fig. 5.32, a long pipe with diameter $R_1 = 0.0225$ and length $L_1 = 0.09$ joins a smaller pipe with diameter $R_2 = 0.005$ and length $L_2 = 0.02$.

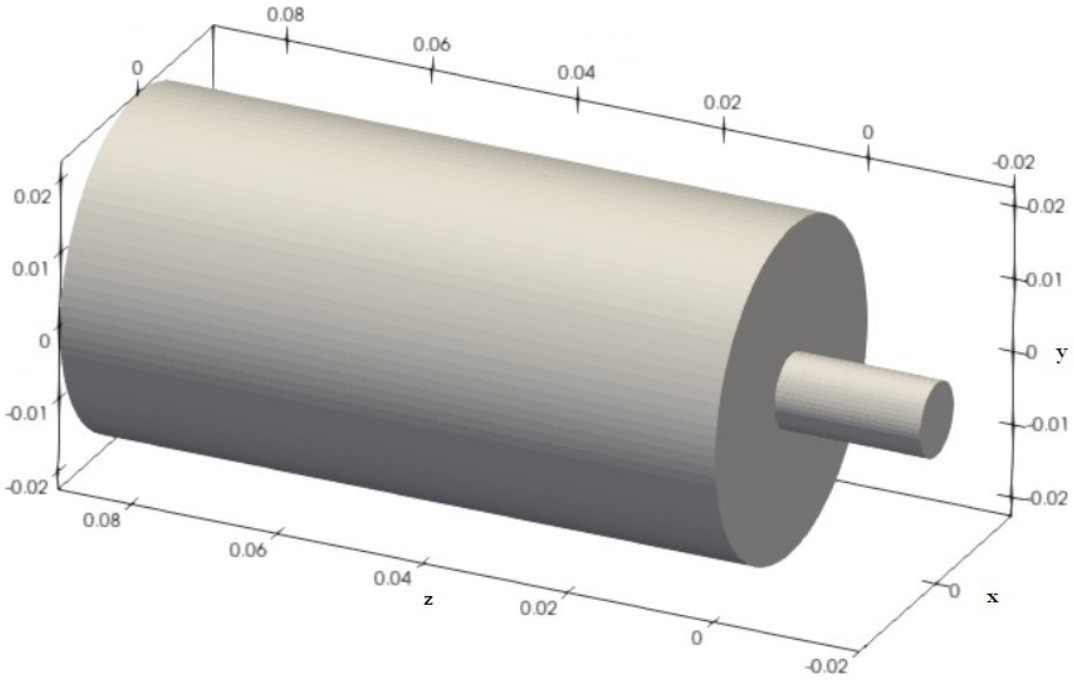

Figure 5.32: 3D axisymmetric contraction geometry

For the inlet boundary condition at $z = L_1$ a parabolic velocity profile is enforced as follows:

$$\mathbf{u} = -u_m \left(1 - \frac{x^2 + y^2}{R_1^2}\right) \mathbf{e}_z, \tag{5.12}$$

where $\mathbf{e}_z = (0, 0, 1)^\intercal$ and u_m is the maximum velocity occurred at the center of the inlet. For the outlet at $z = -L_2$, the "do-nothing" boundary condition [60], and for the walls, the no-slip boundary condition is imposed. As shown in Fig. 5.33, the domain is discretized by 132,096 hexahedral elements.

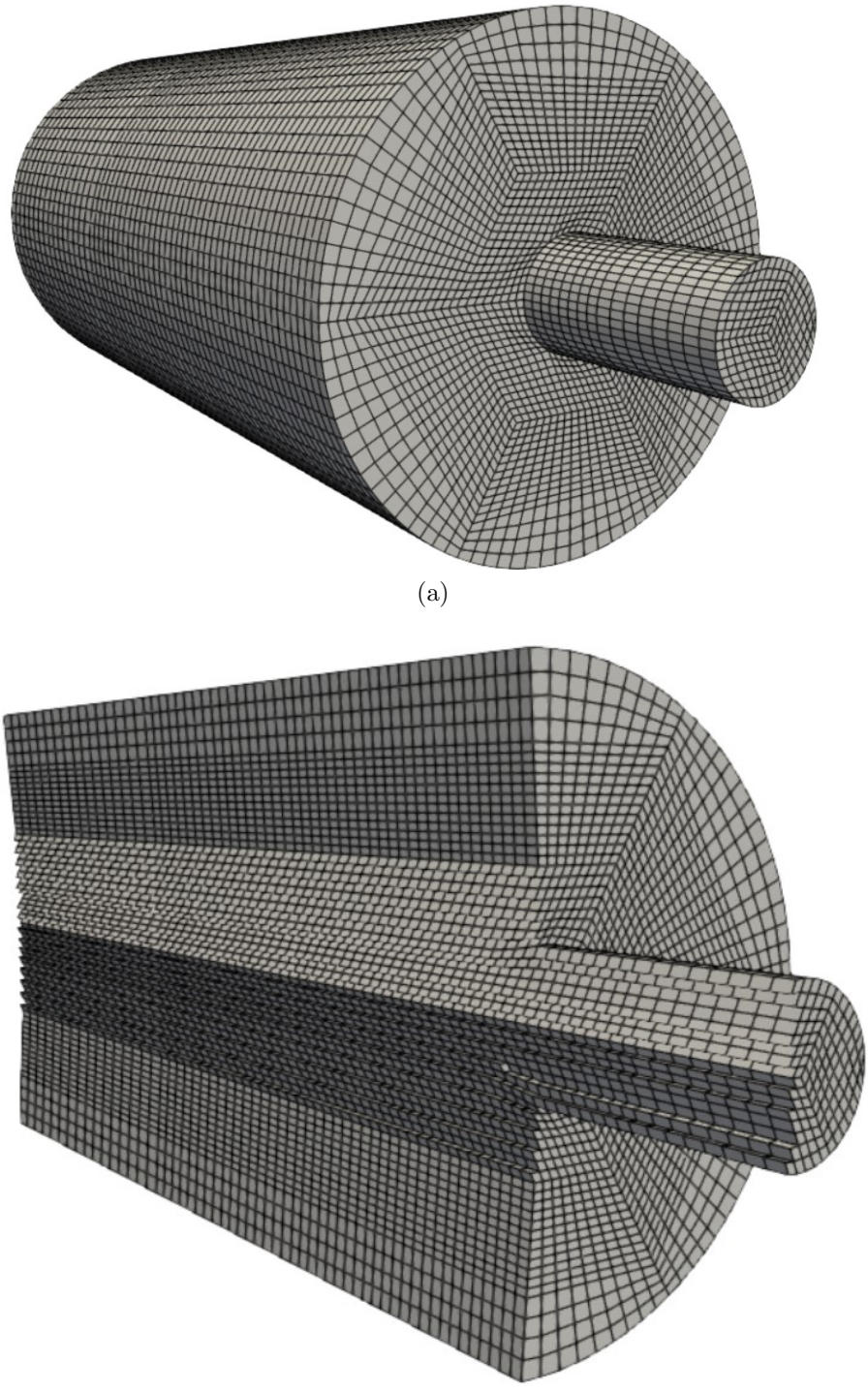

(a)

(b)

Figure 5.33: (a) The 3D axisymmetric contraction geometry discretized by 132,096 hexahedral elements. (b) A detailed view of the interior elements.

Although no definition of the Reynolds number is given in the studies mentioned above, no significant difference in experiments is observed for $0.036 \leq Re \leq 0.005$. In our studies, we assume the diameter of the longer pipe as the characteristic length and define the Reynolds number as

$$Re = \frac{u_{avg} D_1}{\nu} = 0.005,$$

where $u_{avg} = \frac{v_m}{2}$ and $\nu = \frac{\mu}{\rho} = 0.1$.

As the first test case, we simulate a Newtonian flow (without fibers) using the above parameters. The simulation continues until the changes in the calculated solution become sufficiently small (eyeball norm). The line integral convolution technique proposed by Cabral and Leedom [90] is used for producing a high-density streamline plot from the velocity vector field.

The dimensionless vortex length $X^* = \frac{L_v}{D_1}$ is of interest, where L_v is the distance of the vortex detachment point to xy-plane at $z = 0$. It should be noted that the comparison to the experimental and numerical data is based on a qualitative observation of the detachment point.

The distribution of the velocity magnitude in a 2D slice at $X = 0$ is shown in Fig. 5.34. Considering $L_v \approx 0.007$ as the detachment point, our decoupled solver calculates the dimensionless vortex length $X^* \approx 0.16$ (see Fig. 5.35). It shows a very good agreement with the experimental and numerical results of $X^* = 0.16$ presented in [10, 12, 15].

In order to perform a two-way coupled simulation, we inject fibers with $r = 276$ to the domain uniformly through the inlet at a specific time interval. The number of fibers and the interval at which the fibers are injected are chosen such that it guarantees the existence of an average of 2,000 fibers around each computational node. The initial orientation of fibers at the inlet is random, which corresponds to the isotropic orientation distribution.

The volume fraction of the suspension in the experimental study is given as $\phi = 0.045\%$. The corresponding particle number, $N_p = 6$, is assumed to be constant throughout the domain.

As discussed in the previous section, with the above parameters, we can safely employ the simplified stress formula (3.31) (Chapter 3). Due to the complexity of the geometry and the fact that the simplified formula suffices, the implicit approach is used to incorporate the fiber-induced stresses into the Navier-Stokes equations.

We use a random walk approach discussed previously to include the effect of fiber interactions. Using the empirical equation (2.32) (Chapter 2), the interaction

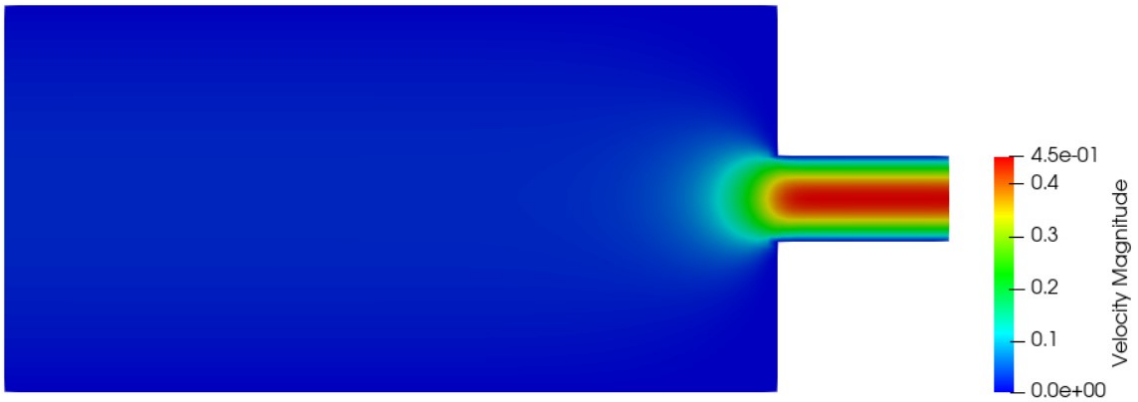

Figure 5.34: The distribution of the velocity magnitude computed with the decoupled solver.

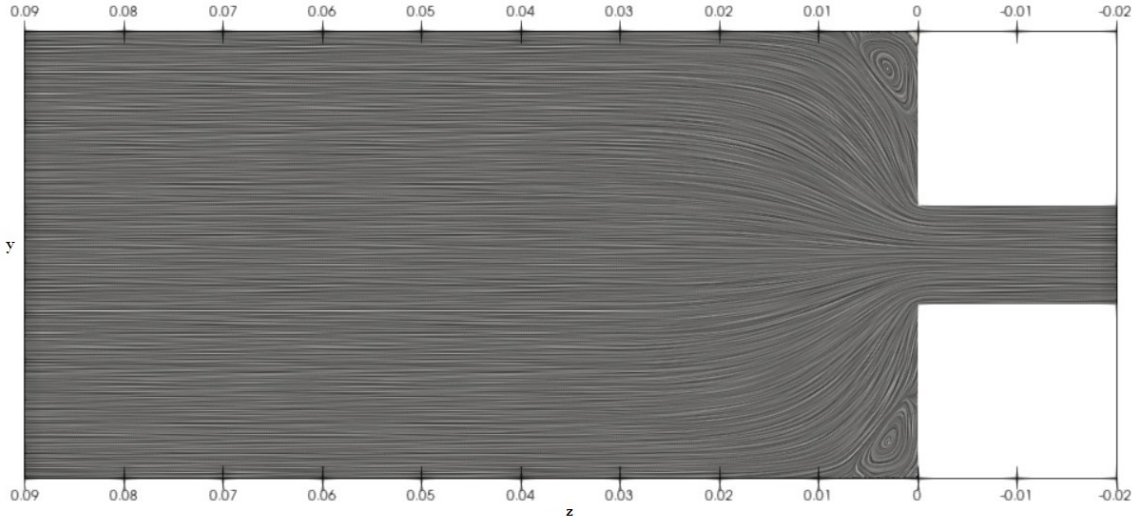

Figure 5.35: The streamlines produced from the velocity vector fields computed with the decoupled solver.

coefficient is approximated $C_I = 0.0008$. VerWeyst and Tucker [12] and Lohmann [15] performed their numerical studies using $C_I = 0.001$ and $C_I = 0.01$, respectively. We use very small time steps for our two-way coupled simulations, and therefore, all presented random walks produce fairly similar results. Consequently, we exploit the fastest approach, i.e., the Cartesian approach in $\mathbb{R}^3$ followed by a projection onto $\mathbb{S}^2$.

The distribution of the velocity magnitude and the streamlines in a 2D slice at $x = 0$ are shown in Figures 5.36 and 5.37, in which a significant increase in the corner vortex size is observed. Considering $L_v \approx 0.025$ as the vortex detachment point, we have the dimensionless vortex length of $X^* \approx 0.55$. It has a good qualitative agreement with the experimental result of Lipscomb et al., whose graph shows $X^* \approx 0.52$ (Figure 10 in [10]). VerWeyst and Tucker [12] calculated $X^* \approx 0.53$ using $C_I = 0.001$, and Lohmann [15] calculated $X^* \approx 0.52$ using $C_I = 0.01$.

We perform a further study by ignoring the influence of fiber interactions, i.e., $C_I = 0$, whose results are shown in Figures 5.38 and 5.39. The streamlines in a 2D slice at $x = 0$ demonstrate a slight decrease in the vortex size by showing $X^* \approx 0.51$.

In this regard, it is worth comparing the results of VerWeyst and Tucker [12] and the numerical study performed by Lipscomb et al. [10]. In the latter, the orientation tensors were computed under the assumption that the fibers are locally aligned with the velocity, i.e., $\mathbf{A} = \mathbf{pp}$, which led to a calculated vortex size of $X^* \approx 0.46$. If $r \gg 1$, the vorticity and straining terms in the Jeffery equations are balanced when a fiber reaches its steady state, i.e., the fiber is aligned towards the flow direction. Although the fully-alignment assumption might be reasonable for dilute fiber suspensions without steep velocity changes, the higher velocity gradient in the vortex area prevents fibers from having time to reach their steady state and to be fully aligned with the flow. Correspondingly, including the rotary diffusion is expected to be an additional source of perturbation, which can explain the smaller vortex size measured by our simulation after deactivating the fiber interactions, i.e., $C_I = 0$.

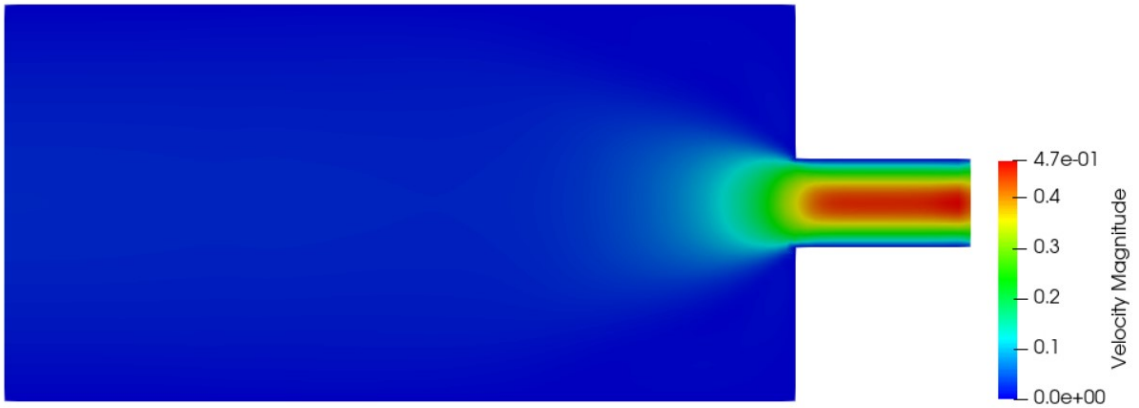

Figure 5.36: The distribution of the velocity magnitude computed with the two-way coupled solver, $N_P = 6$, $C_I = 0.0008$.

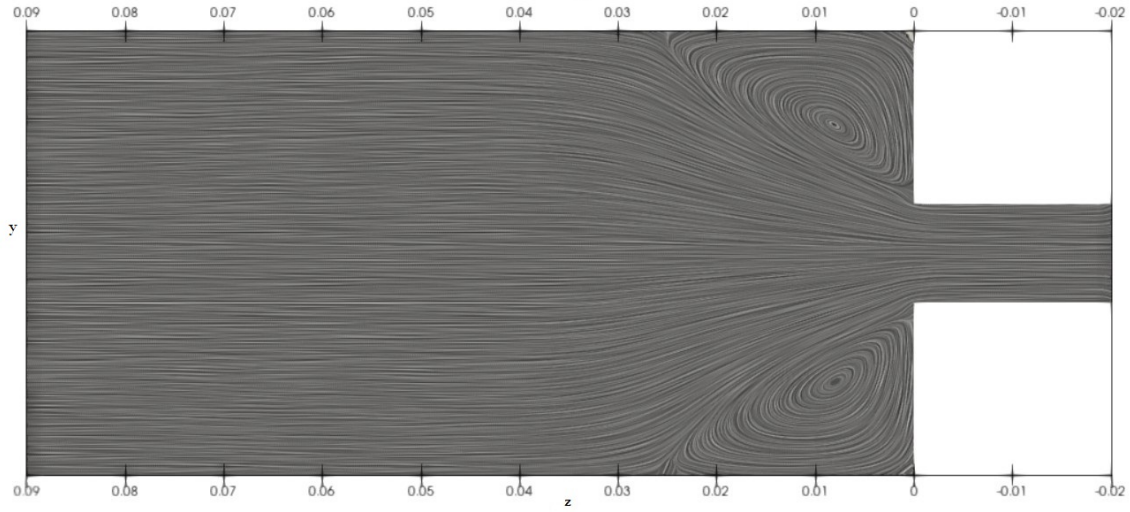

Figure 5.37: The streamlines produced from the velocity vector fields computed with the two-way coupled solver, $N_P = 6$, $C_I = 0.0008$.

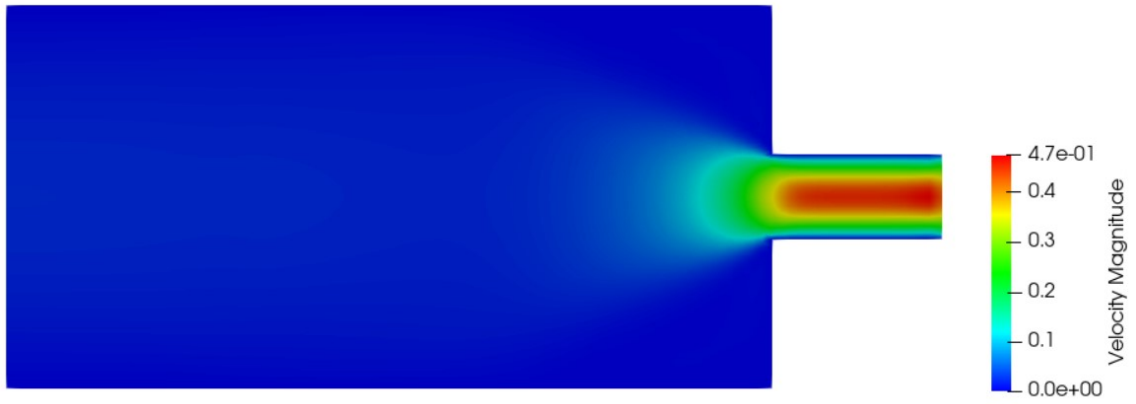

Figure 5.38: The distribution of the velocity magnitude computed with the two-way coupled solver, $N_P = 6$, $C_I = 0$.

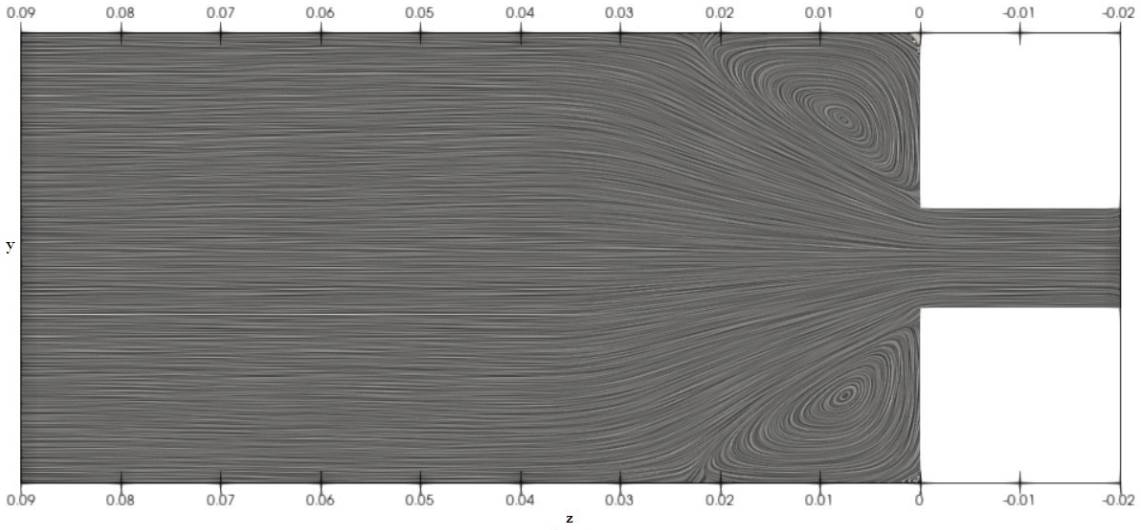

Figure 5.39: The streamlines produced from the velocity vector fields computed with the two-way coupled solver, $N_P = 6$, $C_I = 0$.

Chapter 6

Conclusions

The main objective of the work presented in this thesis was the development of a two-way coupled framework for the numerical simulation of fiber suspension flows that incorporates the fiber-induced stresses in the finite element formulation of the Navier-Stokes equations. Moreover, we expanded random walk methodologies to incorporate fiber-fiber interactions within the Lagrangian framework based on the theory of rotational Brownian motion. This chapter summarizes the presented approaches, highlights key findings, and provides an outlook for future research.

This work began by introducing the fundamental concepts and equations governing the behavior of the fluid and solid phases in fiber suspensions. After reviewing the Lagrangian and Eulerian approaches to treat the disperse phase, we studied the orientation behavior of fibers using these methods in two- and three-dimensional homogeneous flows through one-way coupled simulations of fiber suspension flows. As demonstrated in Section 5.1.1, in the absence of fiber interaction effects, the Lagrangian technique consistently exhibits high accuracy and a general superiority over the majority of Eulerian approximations in both 2D and 3D flows. Additionally, we have shown that the Lagrangian approach is considerably less sensitive to changes in initial conditions than the Eulerian models. Although a few closures produced exact or highly accurate results, no particular one could be found to be suitable for all initial conditions and flows. In contrast, it is worth recalling that the cost of the Lagrangian approach is higher, as it requires translation and rotation of a large number of fibers.

In this work, we developed and applied the random walk methodology to incorporate the additional rotary diffusion term proposed by Hinch and Leal [24] for modeling fiber-fiber interactions. After introducing deterministic and stochastic modeling of

Brownian diffusion, we provided a theoretical framework for generating Brownian motions and random walks through stochastic PDE analysis. Then, we investigated practical algorithms to evaluate random perturbations on the unit sphere. Some of the presented methods were based on the evaluation of Cartesian random walks followed by a projection onto $\mathbb{S}^2$. Chen and Yu [43] computed random walks on the unit sphere by using the second fiber-aligned coordinate system and cumulative probability obtained from an approximate solution to the spherical heat equation. As discussed in Section 4.3.4, this method only yielded accurate results for small time steps. To address the issue of larger ones, we proposed an approach based on a tabulated approximation of the cumulative distribution function obtained from the exact solution of the spherical heat equation. As shown in Section 5.1.2, the exact approach outperformed other methods as the time step increased. However, when it comes to small time steps, all methods under consideration produced similar results. Finally, we employed the methods mentioned earlier to study the effect of fiber-fiber interactions in a 3D homogeneous flow. The results of the Lagrangian simulation using random walks exhibited a very good agreement with the reference solution and demonstrated superior accuracy compared to the numerical results obtained from the Eulerian models.

To develop the two-way coupled numerical simulation tool, we first explored the rheology of fiber suspensions by introducing several constitutive models. Under the assumption of an isotropic orientation state, the constitutive equation (2.36) prompted the formulation of a benchmark that we used to validate our two-way coupled solver later in Section 5.2.1. After explaining the temporal and spatial discretization techniques we employed in this work, we discussed an operator-splitting strategy for solving the Navier-Stokes equations. Then, we presented various aspects of fiber dynamics solver. Building on this foundation, we proposed the two-way coupled solver in a segregated manner for fiber suspension flows. As demonstrated in Section 5.2.1, the simplified version of the constitutive equation yielded sufficiently accurate results for the relatively low volume fraction and high aspect ratio values, which are characteristics of non-dilute regimes. This is particularly relevant when it is essential to employ the implicit approach described in Section 3.2.4, especially when the use of small time steps is constrained by computational limitations. Let us also recall that while the explicit approach offers the benefit of being readily applicable to any constitutive equation for the non-Newtonian stress tensor, the implicit approach may require further consideration.

In the end, the tools and methodologies discussed previously were applied to the three-dimensional axisymmetric contraction problem. For the decoupled case, a small vortex was observed in the corner of the longer pipe. Then, we performed the two-

way coupled simulation incorporating the effect of fiber-induced stresses and fiber-fiber interactions into a dilute suspension. The vortex detachment point was shifted upstream and the vortex size was increased, which were in good qualitative agreement with both the experimental data and the results obtained using the Eulerian models. However, due to the absence of quantitative data, our ability to perform more precise comparisons was limited.

Despite the superior results obtained from the Lagrangian approach compared to the Eulerian one, the cost of the former remains a challenge, especially for complex geometries and higher volume fractions. This is primarily because achieving acceptable accuracy necessitates the presence of a sufficiently large number of fibers throughout the entire domain, which, in turn, results in costly simulations. This challenge is even more pronounced for turbulent flows. Therefore, there is an emphasis on developing a more efficient parallel framework with strong scalability while employing cutting-edge computational resources. Furthermore, it is imperative to incorporate advanced anisotropic rotary diffusion models and conduct further research into the nature of fiber-fiber interactions. It is worth mentioning that non-isothermal processes and more complex phenomena, such as changes in fiber length and fiber breakages, which occur during processes like injection molding, extrusion, and screw-based operations, warrant detailed analysis. Benefiting from the unique attributes of the Lagrangian framework, which features tracking each fiber individually, the approach can readily facilitate the integration of the models that may result from the phenomena mentioned earlier.

Bibliography

[1] H. H. Hu, Direct simulation of flows of solid-liquid mixtures, International Journal of Multiphase Flow 22 (2) (1996) 335–352.

[2] B. Maury, Direct simulations of 2D fluid-particle flows in biperiodic domains, Journal of computational physics 156 (2) (1999) 325–351.

[3] R. Glowinski, T.-W. Pan, T. I. Hesla, D. D. Joseph, A distributed Lagrange multiplier/fictitious domain method for particulate flows, International Journal of Multiphase Flow 25 (5) (1999) 755–794.

[4] D. Wan, S. Turek, Direct numerical simulation of particulate flow via multigrid FEM techniques and the fictitious boundary method, International Journal for Numerical Methods in Fluids 51 (5) (2006) 531–566.

[5] C. S. Peskin, The immersed boundary method, Acta numerica 11 (2002) 479–517.

[6] D. A. Drew, S. L. Passman, Theory of multicomponent fluids, Vol. 135, Springer Science & Business Media, 2006.

[7] G. B. Jeffery, The motion of ellipsoidal particles immersed in a viscous fluid, Proceedings of the Royal Society of London A: Mathematical, Physical and Engineering Sciences 102 (715) (1922) 161–179. doi:10.1098/rspa.1922.0078.

[8] P. Krochak, J. Olson, D. Martinez, Near-wall estimates of the concentration and orientation distribution of a semi-dilute rigid fibre suspension in Poiseuille flow, Journal of fluid mechanics 653 (2010) 431–462.

[9] A. D. Fokker, Die mittlere Energie rotierender elektrischer Dipole im Strahlungsfeld, Annalen der Physik 348 (1914) 810–820. doi:10.1002/andp.19143480507.

[10] G. L. II, M. Denn, D. Hur, D. Bocger, The flow of fiber suspensions in complex geometries, Journal of Non-Newtonian Fluid Mechanics 26 (3) (1988) 297 – 325. doi:http://dx.doi.org/10.1016/0377-0257(88)80023-5.
URL http://www.sciencedirect.com/science/article/pii/0377025788800235

[11] S. G. Advani, C. L. Tucker, The use of tensors to describe and predict fiber orientation in short fiber composites, Journal of Rheology 31 (8) (1987) 751–784. doi:http://dx.doi.org/10.1122/1.549945.
URL http://scitation.aip.org/content/sor/journal/jor2/31/8/10.1122/1.549945

[12] B. E. Verweyst, C. L. Tucker, Fiber suspensions in complex geometries: Flow/orientation coupling, The Canadian Journal of Chemical Engineering 80 (6) (2002) 1093–1106. doi:10.1002/cjce.5450800611.
URL http://dx.doi.org/10.1002/cjce.5450800611

[13] B. Reddy, G. Mitchell, Finite element analysis of fibre suspension flows, Computer Methods in Applied Mechanics and Engineering 190 (18–19) (2001) 2349 – 2367. doi:http://dx.doi.org/10.1016/S0045-7825(00)00238-3.
URL http://www.sciencedirect.com/science/article/pii/S0045782500002383

[14] D. Kuzmin, Planar and orthotropic closures for orientation tensors in fiber suspension flow models, SIAM Journal on Applied Mathematics 78 (6) (2018) 3040–3059.

[15] C. Lohmann, Physics-compatible finite element methods for scalar and tensorial advection problems, Springer, 2019.

[16] S. Montgomery-Smith, W. He, D. A. Jack, D. E. Smith, Exact tensor closures for the three-dimensional Jeffery's equation, Journal of Fluid Mechanics 680 (2011) 321–335.

[17] S. Montgomery-Smith, D. Jack, D. E. Smith, The fast exact closure for Jeffery's equation with diffusion, J. Non-Newtonian Fluid Mech. 166 (2011) 343–353.

[18] D. H. Chung, T. H. Kwon, Improved model of orthotropic closure approximation for flow induced fiber orientation, Polymer composites 22 (5) (2001) 636–649.

[19] V. Verleye, et al., Modelling the flow of fiber suspensions in narrow gaps, in: Rheology series, Vol. 8, Elsevier, 1999, pp. 1347–1398.

[20] E. Prulière, A. Ammar, F. Chinesta, Empirical natural closure relation for short fiber suspension models, International Journal of Forming Processes 10 (2007) 361–385.

[21] M. Sepehr, G. Ausias, P. J. Carreau, Rheological properties of short fiber filled polypropylene in transient shear flow, Journal of Non-Newtonian Fluid Mechanics 123 (1) (2004) 19–32.

[22] J. Wang, J. F. O'Gara, C. L. Tucker III, An objective model for slow orientation kinetics in concentrated fiber suspensions: Theory and rheological evidence, Journal of Rheology 52 (5) (2008) 1179–1200.

[23] H.-C. Tseng, R.-Y. Chang, C.-H. Hsu, Phenomenological improvements to predictive models of fiber orientation in concentrated suspensions, Journal of Rheology 57 (6) (2013) 1597–1631.

[24] E. J. Hinch, L. G. Leal, The effect of Brownian motion on the rheological properties of a suspension of non-spherical particles, Journal of Fluid Mechanics 52 (4) (1972) 683–712. doi:10.1017/S002211207200271X.

[25] E. J. Hinch, L. G. Leal, Constitutive equations in suspension mechanics. part 2. approximate forms for a suspension of rigid particles affected by Brownian rotations, Journal of Fluid Mechanics 76 (1) (1976) 187–208. doi:10.1017/S0022112076003200.

[26] D. L. Koch, A model for orientational diffusion in fiber suspensions, Physics of Fluids 7 (8) (1995) 2086–2088.

[27] N. Phan-Thien, X.-J. Fan, R. Tanner, R. Zheng, Folgar–tucker constant for a fibre suspension in a Newtonian fluid, Journal of Non-Newtonian Fluid Mechanics 103 (2-3) (2002) 251–260.

[28] J. H. Phelps, C. L. Tucker III, An anisotropic rotary diffusion model for fiber orientation in short-and long-fiber thermoplastics, Journal of Non-Newtonian Fluid Mechanics 156 (3) (2009) 165–176.

[29] H.-C. Tseng, R.-Y. Chang, C.-H. Hsu, An objective tensor to predict anisotropic fiber orientation in concentrated suspensions, Journal of Rheology 60 (2) (2016) 215–224.

[30] H.-C. Tseng, R.-Y. Chang, C.-H. Hsu, The use of shear-rate-dependent parameters to improve fiber orientation predictions for injection molded fiber composites, Composites Part A: Applied Science and Manufacturing 104 (2018) 81–88.

[31] J. Paschkewitz, Turbulent drag reduction using microfibers, Ph.D. thesis, Ph. D. Dissertation, Stanford University (2004).

[32] J. Paschkewitz, C. D. Dimitropoulos, Y. Hou, V. Somandepalli, M. Mungal, E. S. Shaqfeh, P. Moin, An experimental and numerical investigation of drag reduction in a turbulent boundary layer using a rigid rodlike polymer, Physics of Fluids 17 (8) (2005) 085101.

[33] J. Gillissen, B. Boersma, P. Mortensen, H. Andersson, Fibre-induced drag reduction, Journal of Fluid Mechanics 602 (2008) 209–218.

[34] R. Benzi, E. S. Ching, E. De Angelis, I. Procaccia, Comparison of theory and direct numerical simulations of drag reduction by rodlike polymers in turbulent channel flows, Physical Review E 77 (4) (2008) 046309.

[35] B. E. VerWeyst, Numerical predictions of flow-induced fiber orientation in three-dimensional geometries, University of Illinois at Urbana-Champaign, 1998.

[36] K. A. Ericsson, S. Toll, J.-A. E. Månson, The two-way interaction between anisotropic flow and fiber orientation in squeeze flow, Journal of Rheology 41 (3) (1997) 491–511. doi:http://dx.doi.org/10.1122/1.550833.
URL http://scitation.aip.org/content/sor/journal/jor2/41/3/10.1122/1.550833

[37] K. Chiba, K. Nakamura, Numerical solution of fiber suspension flow through a complex channel, Journal of Non-Newtonian Fluid Mechanics 78 (2–3) (1998) 167 – 185. doi:http://dx.doi.org/10.1016/S0377-0257(98)00067-6.
URL http://www.sciencedirect.com/science/article/pii/S0377025798000676

[38] K. Chiba, K. Yasuda, K. Nakamura, Numerical solution of fiber suspension flow through a parallel plate channel by coupling flow field with fiber orientation distribution, Journal of Non-Newtonian Fluid Mechanics 99 (2–3) (2001) 145 – 157. doi:http://dx.doi.org/10.1016/S0377-0257(01)00118-5.
URL http://www.sciencedirect.com/science/article/pii/S0377025701001185

[39] K. Chiba, F. Chinesta, Numerical simulation of flow kinematics and fiber orientation for multi-disperse suspension, Rheologica Acta 45 (1) (2005) 1–13. doi:10.1007/s00397-004-0431-2.
URL http://dx.doi.org/10.1007/s00397-004-0431-2

[40] K. Chiba, Eco-strategy of numerical simulation for fiber assembly orientation in an abrupt planar contraction flow, International Journal of Material Forming 3 (2) (2010) 1303–1312. doi:10.1007/s12289-009-0414-z.
URL http://dx.doi.org/10.1007/s12289-009-0414-z

[41] C. Eberhardt, A. Clarke, Fibre-orientation measurements in short-glass-fibre composites. part i: automated, high-angular-resolution measurement by confocal microscopy, Composites Science and Technology 61 (10) (2001) 1389 – 1400. doi:http://dx.doi.org/10.1016/S0266-3538(01)00038-0.
URL http://www.sciencedirect.com/science/article/pii/S0266353801000380

[42] J. J. J. Gillissen, B. J. Boersma, P. H. Mortensen, H. I. Andersson, The stress generated by non-Brownian fibers in turbulent channel flow simulations, Physics of Fluids 19 (11) (2007). doi:http://dx.doi.org/10.1063/1.2800041.
URL http://scitation.aip.org/content/aip/journal/pof2/19/11/10.1063/1.2800041

[43] Y. K. Chen, C. P. Yu, Monte Carlo simulation of fiber orientation in a shear flow with Brownian rotation, Aerosol Science and Technology 16 (4) (1992) 255–264. arXiv:http://dx.doi.org/10.1080/02786829208959554, doi:10.1080/02786829208959554.
URL http://dx.doi.org/10.1080/02786829208959554

[44] M. Manhart, Rheology of suspensions of rigid-rod like particles in turbulent channel flow, Journal of Non-Newtonian Fluid Mechanics 112 (2-3) (2003) 269–293.

[45] A. Moosaie, et al., Direct numerical simulation of turbulent drag reduction by rigid fiber additives, Fachgebiet Hydromechanik, 2011.

[46] A. Novikov, D. Kuzmin, O. Ahmadi, Random walk methods for Monte Carlo simulations of Brownian diffusion on a sphere, Applied Mathematics and Computation 364 (2020) 124670.

[47] F. Folgar, C. L. Tucker, Orientation behavior of fibers in concentrated suspensions, Journal of Reinforced Plastics and Composites 3 (2) (1984) 98–119. arXiv:http://jrp.sagepub.com/content/3/2/98.full.pdf+html, doi:10.1177/073168448400300201.
URL http://jrp.sagepub.com/content/3/2/98.abstract

[48] J. S. Cintra Jr, C. L. Tucker III, Orthotropic closure approximations for flow-induced fiber orientation, Journal of Rheology 39 (6) (1995) 1095–1122.

[49] D. A. Jack, D. E. Smith, Assessing the use of tensor closure methods with orientation distribution reconstruction functions, Journal of Composite Materials 38 (21) (2004) 1851–1871. arXiv:https://doi.org/10.1177/0021998304048413, doi:10.1177/0021998304048413.
URL https://doi.org/10.1177/0021998304048413

[50] O. Ahmadi, D. Kuzmin, Random walk implementation of rotary diffusion in Lagrangian models of fiber orientation, Technische Universität Dortmund, Fakultät für Mathematik, 2017.

[51] C. Lohmann, Physikkonforme Galerkin Verfahren zur Simulation der Orientierungszustände in Fasersuspensionen, Master's thesis, TU Dortmund, https://link.springer.com/book/10.1007/978-3-658-13311-5 (2015).

[52] S. Montgomery-Smith, D. A. Jack, D. E. Smith, A systematic approach to obtaining numerical solutions of Jeffery's type equations using spherical harmonics, Composites Part A: Applied Science and Manufacturing 41 (7) (2010) 827 – 835. doi:https://doi.org/10.1016/j.compositesa.2010.02.010.
URL http://www.sciencedirect.com/science/article/pii/S1359835X10000679

[53] R. S. Bay, Fiber orientation in injection-molded composites: a comparison of theory and experiment, Ph.D. thesis, University of Illinois at Urbana-Champaign (1991).

[54] C. L. Tucker, Flow regimes for fiber suspensions in narrow gaps, Journal of Non-Newtonian Fluid Mechanics 39 (3) (1991) 239 – 268. doi:https://doi.org/10.1016/0377-0257(91)80017-E.
URL http://www.sciencedirect.com/science/article/pii/037702579180017E

[55] H. Brenner, Rheology of a dilute suspension of axisymmetric Brownian particles, International Journal of Multiphase Flow 1 (2) (1974) 195 – 341. doi:https://doi.org/10.1016/0301-9322(74)90018-4.
URL http://www.sciencedirect.com/science/article/pii/0301932274900184

[56] S. M. Dinh, R. C. Armstrong, A rheological equation of state for semiconcentrated fiber suspensions, Journal of Rheology 28 (3) (1984) 207–227. arXiv:https://doi.org/10.1122/1.549748, doi:10.1122/1.549748.
URL https://doi.org/10.1122/1.549748

[57] R. Jongschaap, Microhydrodynamics: Principles and selected applications: S. kim and sj karrila, butterworth-henemann, boston, 1991, 507 pp. price:£ 45.00 (1992).

[58] B. E. VerWeyst, Numerical predictions of flow-induced fiber orientation in three-dimensional geometries. (1999).

[59] J. Evans, The effect of non-Newtonian properties of a suspension of rod-like particles on flow fields, in: Theoretical Rheology, Halstead Press New York, 1975, pp. 224–232.

[60] J. G. Heywood, R. Rannacher, S. Turek, Artificial boundaries and flux and pressure conditions for the incompressible Navier-Stokes equations, International Journal for Numerical Methods in Fluids 22 (5) (1996) 325–352.

[61] V. Girault, P.-A. Raviart, Finite element methods for Navier-Stokes equations: theory and algorithms, Vol. 5, Springer Science & Business Media, 2012.

[62] A. Quarteroni, A. Valli, Numerical approximation of partial differential equations, Vol. 23, Springer Science & Business Media, 2008.

[63] D. Arnold, D. Boffi, R. Falk, Approximation by quadrilateral finite elements, Mathematics of Computation 71 (239) (2002) 909–922.

[64] J. Hron, S. Turek, A monolithic FEM/multigrid solver for an ale formulation of fluid-structure interaction with applications in biomechanics, in: Fluid-structure interaction, Springer, 2006, pp. 146–170.

[65] J. Hron, A. Ouazzi, S. Turek, A computational comparison of two FEM solvers for nonlinear incompressible flow, in: Challenges in Scientific Computing-CISC

2002: Proceedings of the Conference Challenges in Scientific Computing Berlin, October 2–5, 2002, Springer, 2003, pp. 87–109.

[66] S. Turek, On discrete projection methods for the incompressible Navier-Stokes equations: An algorithmical approach, Computer Methods in Applied Mechanics and Engineering 143 (3-4) (1997) 271–288.

[67] S. Turek, Efficient Solvers for Incompressible Flow Problems: An Algorithmic and Computational Approache, Vol. 6, Springer Science & Business Media, 1999.

[68] D. Kuzmin, J. Hämäläinen, Finite element methods for computational fluid dynamics: a practical guide, SIAM Rev 57 (4) (2015) 642.

[69] P. Wesseling, C. W. Oosterlee, Geometric multigrid with applications to computational fluid dynamics, Journal of Computational and Applied Mathematics 128 (1-2) (2001) 311–334.

[70] S.-R. Hysing, Numerical simulation of immiscible fluids with FEM level set techniques, Ph.D. thesis, Dortmund, Techn. Univ., Diss., 2007 (2007).

[71] F.-J. Sayas, A gentle introduction to the finite element method, Lecture notes, University of Delaware (2008).

[72] G. Nikishkov, Introduction to the finite element method, University of Aizu (2004) 1–70.

[73] A. Sokolichin, G. Eigenberger, A. Lapin, A. Lübert, Dynamic numerical simulation of gas-liquid two-phase flows Euler/Euler versus Euler/Lagrange, Chemical Engineering Science 52 (4) (1997) 611 – 626. doi:http://dx.doi.org/10.1016/S0009-2509(96)00425-3.
URL http://www.sciencedirect.com/science/article/pii/S0009250996004253

[74] A. Moosaie, M. Manhart, Direct Monte Carlo simulation of turbulent drag reduction by rigid fibers in a channel flow, Acta Mechanica 224 (10) (2013) 2385–2413.

[75] A. Einstein, On the theory of the Brownian movement, Ann. Phys 19 (4) (1906) 371–381.

[76] N. Wiener, Differential-space, Journal of Mathematics and Physics 2 (1-4) (1923) 131–174.

[77] R. L. Schilling, L. Partzsch, Brownian motion: an introduction to stochastic processes, Walter de Gruyter GmbH & Co KG, 2014.

[78] R. P. Dobrow, Introduction to stochastic processes with R, John Wiley & Sons, 2016.

[79] P. Mörters, Y. Peres, Brownian motion, Vol. 30, Cambridge University Press, 2010.

[80] N. Privault, Notes on stochastic finance, Retrieved from (2013).

[81] B. Oksendal, Stochastic differential equations: an introduction with applications, Springer Science & Business Media, 2013.

[82] D. R. Brillinger, A particle migrating randomly on a sphere, in: Selected Works of David Brillinger, Springer, 2012, pp. 73–87.

[83] A. Mijatović, V. Mramor, G. U. Bravo, et al., Projections of spherical Brownian motion, Electronic Communications in Probability 23 (2018).

[84] E. P. Hsu, A brief introduction to Brownian motion on a Riemannian manifold, lecture notes (2008).

[85] V. Tulovsky, L. Papiez, Formula for the fundamental solution of the heat equation on the sphere, Applied mathematics letters 14 (7) (2001) 881–884.

[86] J. K. Blitzstein, J. Hwang, Introduction to probability, Crc Press, 2019.

[87] L. Devroye, General principles in random variate generation, in: Non-uniform random variate generation, Springer, 1986, pp. 27–82.

[88] C. P. Robert, G. Casella, G. Casella, Introducing Monte Carlo methods with R, Vol. 18, Springer, 2010.

[89] D. F. Rogers, Laminar flow analysis, Cambridge University Press, 1992.

[90] B. Cabral, L. C. Leedom, Imaging vector fields using line integral convolution, in: Proceedings of the 20th annual conference on Computer graphics and interactive techniques, 1993, pp. 263–270.